Studies of an Ultracold Bose-Bose Mixture with Tunable Interspecies Interactions

可調異核相互作用强度的超冷玻色玻色混合氣體的研究

WANG, Fudong

汪福東

A Thesis Submitted in Partial Fulfilment

of the Requirements for the Degree of

Doctor of Philosophy

in

Physics

The Chinese University of Hong Kong

July 2016

Thesis Assessment Committee

Professor LAW Chikwong (Chair)

Professor WANG Dajun (Thesis Supervisor)

Professor ZHOU Qi (Committee Member)

Professor DU Shengwang (External Examiner)

Abstract of thesis entitled:

Studies of an Ultracold Bose-Bose Mixture with Tunable Interspecies Interactions

Submitted by WANG, Fudong

for the degree of Doctor of Philosophy

at The Chinese University of Hong Kong in July 2016

This thesis presents a series of investigations on an ultracold heteronuclear mixture of ^{23}Na and ^{87}Rb. These investigations are carried out in two different apparatuses of double species Bose-Einstein condensate constructed in the course of this thesis work. Firstly, the interspecies Feshbach resonances are measured and analyzed. An s-wave Feshbach resonance is used to control the interspecies interactions and the miscible-immiscible transition of the double species Bose-Einstein condensate is observed. Secondly, the ultracold bosonic Feshbach molecules of NaRb are formed by magneto-association. Binding energies of the Feshbach molecules are measured and analyzed with a two-channel square well model. Thirdly, we study several few-body processes with this mixture. With the same s-wave Feshbach resonance, we measure the scattering length dependent dimer-dimer and atom-dimer loss rates and find two resonances which are closely related to the three-body Efimov effect. These results will shed new light on our understanding of several important elementary few-body processes and also establish the Na-Rb mixture as a nice system for such investigations.

摘要

這篇論文介紹了一些對超冷鈉23–銣87混合氣體的研究。這些研究利用了兩套不同的雙組份玻色愛因斯坦凝聚的裝置。第一，我們測量并分析了鈉-銣異核原子間的費甚巴赫共振。我們用一個 s波費甚巴赫共振操控異核原子間的相互作用强度，觀察到了可混合態和不可混合態之間的轉變。第二，我們用磁耦合的方法製備了超冷的玻色鈉銣費甚巴赫分子，測量並且用雙方勢阱模型分析了費甚巴赫分子的束縛能。第三，我們研究幾個異核玻色混合氣體中的少體過程。利用同一個費甚巴赫共振，我們測量了與散射長度有關的二聚體–二聚體和原子–二聚體的損失速率，發現了兩個與葉菲莫夫效應有關的共振。這些結果證明鈉銣混合氣體是一個不錯的研究少體問題的體系，並且可以幫助我們理解一些重要的少體過程。

Acknowledgements

I could not finish the works presented in this dissertation without the help from many people. First, I have to thank my advisor, Dajun Wang who give me a chance to work in this group and all his help over the last five years. I really appreciate the insightful advices he has given on all aspects of my work, from elementary technical skills to diagnosing technical problems, designing experiments, presenting experimental results, and so on. I am so grateful to be one of his students.

I learn a lot from Dr. Dezhi Xiong, Dr. Xiaodong He and Dr. Bo Lu, who are postdocs I worked with in this five years. They are patient with all my questions and teach me everything from how to read the resistor color codes to how to run experiments. I would also like to thank them for sharing their experiences in academics and in life with me. I thank Ting-Fai Lam, a graduate student when I enter this group, for giving me advices to make things work. I thank Dr. Jie Ma and Ting-Fai for the first-phase preparations of our apparatus I. With their work, we cannot realize the Rb BEC so quickly.

I would like to thank Dr. Xiaoke Li, my lab partner whom I worked with from the beginning of my PhD study in CUHK. His patience and persistence ensure that the system works well. I am glad to share with him the works, discussions, as well as the joyful moments.

I would like to thank Bing Zhu, Jun Chen, Mingyang Guo, Xin Ye and

Lintao Li for their help with the experiments. They helped to attack the problems we meet in experiments and always bring new ideals to the experiments. They are all hardworking and enthusiastic. Without them the apparatuses could not produce so many results.

Besides the few people that worked in our group, there are many more peoples that help me a lot in the past years. I would like to thank Prof. Qi Zhou for the useful discussions. I thank Prof. Eberhard Tiemann for the collaborations on the work of Na-Rb Feshbach resonances and kindly answering my questions about Feshbach resonance. I thank Prof. Doerte Blume for the collaborations on the work of few-body physics. I thank Yueyang Zou, Xinyu Luo and other peoples with whom I discuss about physics and experimental techniques. I would like to thank the staff members in the department of physics and mechanical workshop.

I thank Prof. Mingchung Chu for his kind help.

Last, but not the least, I would like to thank my families for their support through the years.

Dedicated to my family.

Contents

List of Figures

List of Tables

Chapter 1

Introduction

70 years after the theoretical prediction of Bose-Einstein condensation(BEC) [7, 8], people successfully realized the BEC in dilute atomic gases[9, 10, 11] in 1995. Later, the degenerate Fermi gas has also been realized in a spin mixture of ^{40}K [12]. These pioneering works have produced a wholly new exciting field that continues to thrive. Landmark results include the creation of vortices in superfluid quantum gases [13], tuning interaction strength with a Feshbach resonance[14, 15], simulating condensed matter physics with optical lattices [16, 17], studies of few-body physics [18], creation of ultracold polar molecules [19], studies of spinor gases in ultracold atoms [20] and realization of the BCS-BEC crossover [21, 22].

In this thesis, we build two ^{23}Na-^{87}Rb mixture apparatuses to create ultracold NaRb polar molecules and to explore the few-body physics in a herteronuclear boson-boson mixture. (In this thesis Rb represents the ^{87}Rb unless specified.) The works and progresses will be discussed in section 1.1 and 1.2.

1.1 Ultracold NaRb polar molecules

In contrast to conventional atomic gases, of which the interactions are isotropic short range van der Waals interactions, dipolar systems have the dipole-dipole interactions (DDI) between particles. The DDI make it is possible to study different physics in the dipolar systems compared to the usual neutral atoms [23].

The DDI between two dipole moments (magnetic dipole moments or electric dipole moments) reads

$$V_{dd}(r,\theta) = \frac{C_{dd}}{4\pi}\frac{1-3cos^2\theta}{r^3} \tag{1.1}$$

The C_{dd} is $\mu_0\mu_m^2$ for magnetic dipole moments and d^2/ϵ_0 for electric dipole moments, respectively. μ_m is the magnetic dipole moment and d is the electric dipole moment. μ_0 is the magnetic constant and ϵ_0 is the vacuum permittivity. m is the mass of a single dipole moment. $r = |\mathbf{r}|$ is the separation between the two dipoles and θ is the angle between $\mathbf{r}$ and the direction of the external field. The interaction between two head to tail aligned dipoles is attractive while it is repulsive if the two dipoles are aligned shoulder to shoulder. The critical value of θ is 54.7°. Therefore we can tuning the DDI to be attractive or repulsive by changing the angle θ.

In order to characterize the strength of this anisotropic long range tunable interaction, it is useful to define an effective scattering length, the so called dipole length [24] as

$$a_{dd} = \frac{C_{dd}m}{4\pi\hbar^2}. \tag{1.2}$$

The ratio between a_{dd} and the s-wave scattering length a is widely used to measure the strength of the DDI relative to the contact interaction.

The DDI dramatically changes the scattering properties at ultralow tem-

perature regime [25]. With the DDI, the dipolar BEC can only be stablized by carefully tunning the parameters of the system, such as θ and the dimensionality of the external trap [23]. The excitation spectrum of a stable dipolar condensate has a roton-maxon structure similar to the that in the superfluid helium [24]. For Fermions, the DDI deforms the Fermi surface [26]. At ultralow temperature, the DDI opens the possibility for BCS pairing in a single component dipolar Fermi gas [24]. After loaded into optical lattice, the anisotropic and long range character of DDI helps to realized exotic quantum phases. One example is the supersolid phase which can be realized in a 2-D optical lattice with a dipolar Bose gas [27].

In order to realize an ultracold dipolar system, one can use Rydberg atoms or magnetic atoms. Alternative realizations are ultracold diatomic heteronuclear molecules such as KRb [19]. For a quantitative understanding of the DDI strength of different systems, a summary of the dipole lengths for different systems are shown in Fig 1.1. The heteronuclear molecules composed of two alkali atoms have much larger dipole lengths than the magnetic atoms and much longer lifetime than the Rydberg atoms. Thus they are suitable for the studies of strongly interacting dipolar gases.

Since 2008, the dipolar ground state KRb molecules have been carefully studied and many important results are obtained. However, this molecule is unstable [19, 28] since both the exchange reaction $2XY \rightarrow X_2 + Y_2$ and the trimer formation reaction $2XY \rightarrow X_2Y + Y$ are exothermic [29]. Here X and Y denote two kinds of atoms. The instability limits the applications of KRb molecules. Therefore, people start to work on other bi-alkali atoms combinations, among which there are five stable combinations (NaK, NaRb, NaCs, KCs and RbCs[29]) in terms of these two kinds of chemical reactions. We can see that the NaRb molecules have the second largest permanent

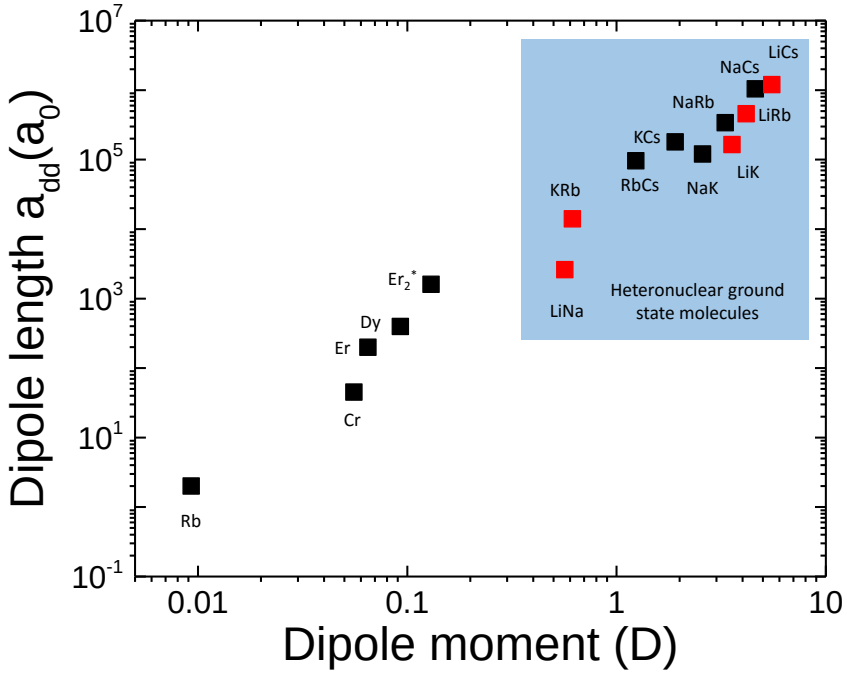

Figure 1.1: Comparsion of dipole lengths of neutral alkali atoms, magnetic atoms, Feshbach molecules of magnetic atoms and heteronuclear molecules of bi-alkali atoms in their ground states[1, 2]. The Rydberg atoms are not shown in this figure since they have much larger dipole lengths. The red squares denote the chemical unstable bi-alkali molecules.

electric dipole moment among the stable combinations. Thus we use Na-Rb mixture to create dipolar molecules, which would accompany the experiments of KRb [19], RbCs [30, 31], NaK [32] and would constitute a great step towards the study of strongly interacting bosonic dipolar gases.

Due to the complexity of the molecular energy levels and the lack of cycling transitions, it is difficult to apply the well established laser cooling technique to the molecules. Despite the recent progress in creation of a magneto optical trap of a diatomic molecule [33, 34, 35], the lowest achieved temperature is 400 μK [35]. The temperature is still too high to realize the dipolar

quantum gas which can only be achieved by associating atomic quantum gases nowadays. This associating method has been successfully used in the experiments of homonuclear molecules [36, 37] and heteronuclear molecules [19]. There are three steps in this method: creating ultracold mixture, associating Feshbach molecules and transferring the molecules to the ground state. We try to follow this method. For our Na-Rb mixture, thanks to the preferable scattering properties, both the two kinds of atoms can be cooled to degenerate without the need to tune the magnetic field. Although there is no experiments about the Na-Rb interspecies Feshbach resonances, the Feshbach spectroscopy of Na[38], Rb[39] as well as the potentials of Na-Rb [40] are studied. All these informations help to identify and analyze the Feshbach resonances of Na-Rb[3]. The creation of NaRb Feshbach molecules[6] follows the magneto-association method [15, 41], which can be understand with the Laudau-Zener formula. These two steps have been finished and will be described in details in this thesis.

The last step of creating the ground state molecules is to transfer the Feshbach molecules to the ground state. One powerful method is the stimulated Raman adiabatic passage (STIRAP) [19, 37, 42, 43], in which process the Feshbach molecules are state selectively transferred to the ground state with high efficiency and the binding energy is taken away by the laser fields. In STIRAP, two coherent laser beams couple the Feshbach molecular state the ground state via an intermediate state. This process can be understood with the Λ-type three energy level system. When two photon detuning of the Raman lasers is zero, the dark state, which is a superposition of the Feshbach molecular state and the ground state, depends on the power of the two laser beams. By adiabatically changing the laser beams' power, the dark state changes from the Feshbach molecular state to the ground state and no

molecules will be populated in the intermediate state.

In order to realize the STIRAP, one or more suitable intermediate states have to be identified. The intermediate state should have a strong coupling to both the Feshbach molecular state and the ground state. For transferring Feshbach molecules to the rovibrational ground state of the singlet or triplet potential, the intermediate state should have singlet and triplet character. The Franck-Condon factor, which are the squares of the overlap integrals between vibrational wavefunctions, should also be as large as possible. For our NaRb molecules, possible choices can be found in the $1^1\Pi$-$2^3\Sigma^+$ [44] or the $2^1\Sigma^+$-$1^3\Pi$[45, 46] coupled electronic states. Molecules have hyperfine structures. For the ground state, it is required that only one hyperfine state will be populated. If it is not the lowest hyperfine state, spin-changing collisions may cause loss problem. Therefore, it is preferable that the excited state can couple the lowest hyperfine states in order to avoid additional transfer steps[47]. What is more, the splitting of different hyperfine states of the intermediate state should be large enough to avoid the problem associated with the "multiple intermediate states problem"[48]. Recently, we identify a suitable intermediate state and successfully create the ground state NaRb molecules[49] with a transferring efficiency about 80 %. It is a great step towards the degenerate NaRb polar molecules. The work of STIRAP will not be indroduced here, for more information please read other publications of our group.

1.2 Ultracold Na-Rb mixture

The ultracold mixtures of atomic gases exhibit rich physics unreachable to single species quantum gas experiments. One example is the miscible-immiscible transition. When the repulsive interspecies interaction are larger

than the intraspecies ones, two BEC will seperate in real space. After creating the double species BEC of Na and Rb, we use an interspecies Feshbach resonance to tune the interspecies interaction strength. The miscible-immiscible transition has been observed observed and analyzed.

Another example is the study of few-body physics in a heteronuclear mixture. According to V. Efimov's predictions [50, 51], there would be an infinite number of three-body bound states as well as a geometrical scaling universality when three identical quantum particles subjected to resonant pair-wise interactions. Thanks to the accessibility of the interaction strength, the experiments of cold atoms are suitable for the study of Efimov physics. In 2006, Kraemer *et al.* [18] observed an Efimov resonance in ultracold Cs gas. Since then extensive studies are performed in other atomic species. And the studies in three-distinguishable-particle and four-identical-boson cases are also performed. In our heteronuclear bosonic Na-Rb system, we measured the scattering length dependent atom-dimer and dimer-dimer recombination rates by tuning the magnetic field close to an interspecies Feshbach resonance. The two observed recombination resonances are closely related to the trimer and tetramer states. This observation would be supplemental to other experiments and help to understand the few-body physics in a heteronuclear bosonic mixture.

1.3 Thesis outline

All the works in this thesis are motivated by the long-term goal of our group: creating a BEC of dipolar NaRb molecules. The five-year PhD studies can be divided into two stages. In the first three years, the experiments follows the three steps of creating the ground state NaRb molecules. A single chamber apparatus of Na and Rb mixture is constructed. The ultracold mixture of

Na and Rb is created by laser cooling and evaporative cooling. Interspecies Feshbach resonances are measured and analyzed. One s-wave resonance located near 347 G is used to control the miscibility of double species BEC of Na and Rb. We also successfully associate NaRb Feshbach molecules by magneto-association with the same resonance.

After the work of Feshbach molecules, we realize that there are several limitations in the single cell system: The number of Na and Rb is too small and the lifetime is too short because that the contradictory requirements of vacuum pressure of laser cooling and evaporative cooling are hard to be fulfilled; The optical access is poor and it is difficult to add other optical components such as the optical lattice beams; The large size the glass cell makes is it hard to add strong electric field which is crucial to induce strong DDI. Therefore, from the third year of my PhD study, we began to design a two-cell system in which one cell is used to collect MOTs and the other one is used to do following experiments. A mechanic translation stage is used to transfer atoms between these two cells. Then I focus on the construction of the new system. After one and a half years of work, the NaRb Feshbach molecules can also be created in this new system. In order to increase the number of Feshbach molecules, we study the collision properties of the Feshbach molecules and free Na and Rb atoms near the resonant magnetic field, which correspond to the studies of few-body problems. These results help to understand three-body and four-body physics in a heteronuclear boson-boson mixture and give informations about how to mitigate loss during association of Feshbach molecules.

Basically, this thesis belongs to the preparing work of the dipolar ground state NaRb molecules and it is organized as follows:

Chap 2: Brief introductions of the scattering at ultralow temperature,

Feshbach resonance as well as the properties of a BEC with interactions. This chapter is not intended to give the complete information about these topics. More details can be found in the references therein.

Chap 3: Descriptions of our first Na-Rb machine, the single-cell apparatus. Details cannot be found in research publications due to the limitation of page number, this chapter discusses relevant experimental techniques. However, since the laser cooling and trapping are well established techniques, I will not give details about how we optimize the MOT, molasses and optical pumping in this chapter. People can find more details in other publications of our group.

Chap 4: Details of our second Na-Rb machine: a two-cell apparatus. Since many established techniques in the first apparatus are used, I only discuss the hardware which is different from that of the previous one.

Chap 5: I will describe how we create the dBEC of Na and Rb. We use a hybrid trap of which the trap minimum is shifted away from the zero magnetic field point of the QT by a red detuned ODT. I will describe how we align the hybrid trap and the problems we have met when dealing with the hybrid trap. This chapter closely follows [52, 53].

Chap 6: In the first part, the interspecies Feshbach resonances are measured and analyzed. In the second part, we use an s-wave Feshbach resonance to control the interspecies interaction. By carefully tuning the experimental parameters, we realize the miscible-immiscible transition in our Na-Rb system. The results are compared with numerical simulations. This chapter closely related to our publications of [3, 53].

Chap 7: In this chapter, I will report the creation of NaRb Feshbach molecules via magneto-association. The lifetime of the Feshbach molecules are measured to be about 20 ms, which is long enough for the next step

towards ground state molecules. We also measure the binding energies of the Feshbach molecules. The results are fitted with the two-channel square well model. This chapter follows [6].

Chap 8: A brief introduction of the Efimov physics is presented at the beginning of this chapter. Then I give the details how we measure and analyze the atom-dimer and dimer-dimer recombination rates. This experiment has not been finished when writing this thesis. For more experimental details and theoretical understandings of this experiment, please read an upcoming publication.

Chap 9: Conclusions are drawn in this chapter and an outlook is given for future experiments in the Na-Rb mixture.

□ End of Chapter.

Chapter 2

Theoretical background

Understanding two-body collisions yields insight into interactions in experiments of quantum gases. In this chapter, a brief introduction of the scattering theory at ultra-low temperature will be presented. Then the Feshbach resonance(FR) is described with the two-channel square well model. Further, the relation between the s-wave scattering length a and the interaction strength is understood with two simple pictures. In the last part, Gross-Pitaevskii (GP) equation is introduced and the properties of a BEC with interaction are discussed.

2.1 Scattering at ultra-low temperature

In order to describe the elastic collision of two spinless atoms with an isotropic interaction, it is convenient to use the coordinates of the center of mass. The wave function after scattering can be expressed as

$$\psi = e^{i\mathbf{k}\cdot\mathbf{r}} + f(\theta)\frac{e^{ikr}}{r}. \tag{2.1}$$

This wave function is composed of two parts: an incoming plane wave $e^{i\mathbf{k}\cdot\mathbf{r}}$, and a scattered wave depends on the scattering amplitude $f(\theta)$. The wave function ψ can be expanded into partial waves

$$\psi = \sum_{l=0}^{\infty} A_l P_l(\cos\theta) R_l(r) \tag{2.2}$$

where l is a quantum number denotes the orbital angular momentum and $P_l(\cos\theta)$ are Legendre polynomials. $R_l(r)$ is the radial part of the wave function. The scattering amplitude can also be expanded as

$$f(\theta) = \frac{1}{2ik} \sum_{l=0}^{\infty} (2l+1) \left(e^{i2\delta_l} - 1\right) P_l(\cos\theta) \tag{2.3}$$

Here δ_l is the phase shift for the partial wave l. The total scattering cross section reads

$$\sigma = 2\pi \int_{-1}^{1} d(\cos\theta) |f(\theta)|^2 = \frac{4\pi}{k^2} \sum_{l=0}^{\infty} (2l+1) \sin^2\delta_l \tag{2.4}$$

For two atoms interact with the van der Waals interaction $V_{vdW}(r) = -C_6/r^6$, $R_l(r)$ obey an equation of

$$R_l'' + \frac{2}{r} R_l' + \left[E - \frac{2\mu}{\hbar^2} \left(V_{vdW}(r) + V_{rot}(r)\right) r^2\right] R_l = 0 \tag{2.5}$$

where $V_{rot}(r) = l(l+1)\hbar^2/(2\mu r^2)$ is the rotational energy barrier and μ is the reduced mass. For typical experiments, $T \sim 1\mu K$. Thus V_{rot} is much larger than the kinetic energy of atoms when $l \geq 1$. As a result of which, only the s-wave scattering is important and higher partial waves can be neglected.

Consequently, the total scattering cross section becomes

$$\sigma = \frac{4\pi \sin^2 \delta_0}{k^2} = \frac{4\pi a^2}{1 + k^2 a^2} \tag{2.6}$$

Where the s-wave scattering length is defined as

$$a \equiv -\lim_{k \to 0} \frac{\tan \delta_0 (k)}{k} \tag{2.7}$$

In the limit of low temperature, $ka \ll 1$, $\sigma = 4\pi a^2$ is independent of temperature. For large scattering lengths $ka \gg 1$, the scattering cross section reaches to the unitary limit $\sigma = 4\pi/k^2$ and is independent of a.

2.2 Feshbach resonance

For two alkali atoms scattering, the interaction depends on the the electronic spins $\mathbf{s}_1$ and $\mathbf{s}_2$

$$V(r) = V_{vdW}(r) + J(r)\, \mathbf{s}_1 \cdot \mathbf{s}_2 \tag{2.8}$$

When r is small, the exchange interaction $J(r)$ is large and $V(r)$ are different for the singlet ($S = 0$) and triplet ($S = 1$) potentials. (Where S is the total electronic spin.) When r is large, $J(r)$ is small and the singlet and triplet potentials coincide. At ultra-low temperature, short range details of these two potentials can not be resolved by the scattering wave function. In this condition, scattering processes are dominated by $V_{vdW}(r)$. Let us consider a simple picture: a bound state of the closed channel V_c and a scattering state of the open channel V_o are coupled together by hyperfine interaction

and spin-spin interaction. The Schrödinger equation can be writen as

$$\begin{pmatrix} -K + V_o + \mu_o B & \Omega \\ \Omega & -K + V_c + \mu_c B \end{pmatrix} \begin{pmatrix} \phi_o \\ \phi_c \end{pmatrix} = E \begin{pmatrix} \phi_o \\ \phi_c \end{pmatrix} \tag{2.9}$$

Where K is the kinetic energy and Ω is the coupling. The two potentials can be tuned by magnetic field B since the magnetic dipole moments of these two potentials μ_c and μ_o are different. Since the short range details can not be resolved in ultra-low energy scattering process, V_c and V_o can be replaced by two square well potentials and the trial solution is

$$\chi = \begin{cases} A_+ \sin q_+ r \cdot \chi_+ + A_- \sin q_- r \cdot \chi_-, (r < r_0) \\ B_+ \sin\left(kr + \eta\right) \cdot \chi_o, (r \geq r_0) \end{cases} \tag{2.10}$$

where $q_\pm$ are wave vectors associated with eigenstates $\chi_\pm$ in the range $r < r_0$. This problem can be solved by substituting this trial solution into the Schrödinger equation and using the continuous and differentiable requirements of a wave function. If the scattering state is near degenerate with the bound state, the scattering properties will be dramatically modified and there is a resonance. According to [15, 54], we have a simple formula for a near a resonant magnetic field B_0

$$a = a_{bg}\left(1 - \frac{\Delta}{B - B_0}\right) \tag{2.11}$$

Where the background scattering length a_{bg} depends on the details of the two potentials. The resonance's width Δ is determined by the coupling strength Ω. The tunablity of a is proved that: at $B \to B_0^<$,$a \to +\infty$ while at $B \to B_0^>$,$a \to -\infty$.

2.3 Tunable interactions with Feshbach resonance

The interaction strength of a dilute gas in many body system level is proportional to a [54]

$$g\delta(r) = \frac{2\pi\hbar^2}{\mu} a\delta(r) \tag{2.12}$$

One intuitive physical picture to understand this result is that when a particle passes through an atomic cloud, the scattered wave function is

$$e^{ikr} + f_0 \frac{e^{ikr}}{r} \tag{2.13}$$

where f_0 is s-wave scattering amplitude and $k = \sqrt{2\mu E/\hbar^2}$ is wave vector corresponding to kinetic energy E. Thus the complex refractive index reads[55]

$$n = 1 + \frac{2\pi\rho}{k^2} f_0 \approx 1 - \frac{2\pi\rho a}{k^2} \tag{2.14}$$

Here ρ is the density of the atomic cloud. Substituting $f_0 \approx -a$, the total phase shift of the scattering wave function is

$$\varphi = \int (n-1)\, k dl \approx -\frac{2\pi\rho a}{k} \int dl \tag{2.15}$$

Since the phase shift when a particle passes through a potential is

$$\varphi = \int \left[\sqrt{\frac{2\mu}{\hbar^2}(U-E)} - \sqrt{\frac{2\mu}{\hbar^2}E} \right] dl \approx -\frac{\mu}{\hbar^2 k} U \int dl \tag{2.16}$$

we can get the interaction is proprotional to a as

$$U = \frac{2\pi\hbar^2\rho a}{\mu} \tag{2.17}$$

For another physics picture, let us considering putting N atoms in to a spherical box with radius R. The asymptote wave functions are $R(r) \approx \sin(kr)/r$ or $R'(r) \approx \sin(kr - ka)/r$ when the interactions are absent or present. Since the wave functions vanish at $r = R$, we have $k = \pi/R$ and $k = \pi/(R-a)$ for the two cases. Therefore the energy difference is

$$\frac{\hbar^2}{2\mu}\left(\frac{\pi}{R-a}\right)^2 - \frac{\hbar^2}{2\mu}\left(\frac{\pi}{R}\right)^2 \approx \frac{\hbar^2\pi^2 a}{\mu R^3} \propto \frac{2\pi\hbar^2\rho a}{\mu} \tag{2.18}$$

where $R(r) = \frac{1}{\sqrt{2\pi R}r}\sin\left(\frac{\pi r}{R}\right)$ and $\rho = |R(0)|^2 = \frac{\pi}{2R^3}$ is the density.

It is clear that the effective interaction is repulsive for a positive a and attractive for a negative a. Therefore, by tuning the magnetic field close to a Feshbach resonance, the interaction can be anonymous large, both attractively and repulsively.

2.4 Gross-Pitaevskii equation and BEC with interaction

BEC occurs in a gas of bosonic atoms when the thermal de Broglie wavelength $\lambda_T = \sqrt{2\pi\hbar^2/mk_BT}$ is comparable with atom spacing [56]. In a BEC state, there is a macroscopic occupation of the ground state of the trap potential.

For an ideal gas trapped in a 3-D harmonic potential

$$V_{ext}(x,y,z) = -\frac{1}{2}m\left(\omega_x^2x^2 + \omega_y^2y^2 + \omega_z^2z^2\right) \tag{2.19}$$

the transition temperature is

$$T_c = \frac{1}{k_B}\frac{\hbar\bar{\omega}N^{1/3}}{\zeta(3)^{1/3}} \approx 0.94\hbar\bar{\omega}N^{1/3} \tag{2.20}$$

where $\omega_i\,(i=x,y,z)$ are trap frequencies and $\bar{\omega}=\left(\omega_x\omega_y\omega_z\right)^{1/3}$ is the average trap frequency. N is the atom number and $\zeta\,(3)$ is the Riemann-Zeta function.

In reality, interactions between atoms always present and the properties of BEC are different from that of ideal gas. In order to quantitatively describe a BEC with interaction, we need to use the time dependent and time independent Gross-Pitaevskii (GP) equation [56]

$$i\hbar\frac{\partial}{\partial t}\Phi\left(\mathbf{r},t\right) = \left[-\frac{\hbar^2}{2m}\nabla^2+V_{ext}+g|\Phi\left(\mathbf{r},t\right)|^2\right]\Phi\left(\mathbf{r},t\right) \tag{2.21}$$

$$\mu\phi\left(\mathbf{r}\right) = \left[-\frac{\hbar^2}{2m}\nabla^2+V_{ext}\left(\mathbf{r}\right)+g\phi^2\left(\mathbf{r}\right)\right]\phi\left(\mathbf{r}\right) \tag{2.22}$$

The condensate wave function $\Phi\left(\mathbf{r},t\right)=\phi\left(\mathbf{r}\right)\exp\left[-i\mu t/\hbar\right]$ is normalized with $\int d\mathbf{r}|\Phi\left(\mathbf{r},t\right)|^2=\int d\mathbf{r}\phi\left(\mathbf{r}\right)^2=N$. V_{ext} is the external trap potential, $g=4\pi\hbar^2a/m$ is the interaction strength introduced before.

For the repulsive interactions, stable condensates can be produced and the size of which increase compared with ideal gases. However, for attractive interactions, the atomic gas tends to increase its density. If g is small, attractive interaction can be balanced by the zero-point kinetic energy. But if $N|a|/a_{ho}\geq 0.575$ $\left(a_{ho}^2=\hbar/\left(m\bar{\omega}^2\right)\right)$ [57] , the BEC collapses.

For large BEC, the interaction energy if much larger than the kinetic energy since

$$\frac{E_{int}}{E_{kin}}=\frac{N|a|}{a_{ho}} \tag{2.23}$$

In this case, we can use the Thomas-Fermi(TF) approximation by neglecting the kinetic energy term and the density distribution of the BEC can be obtained as

$$n\left(\mathbf{r}\right)=\mathrm{Max}\left(0,\frac{\mu-V_{ext}\left(\mathbf{r}\right)}{g}\right)=\frac{15}{8\pi}\frac{N}{\prod_i R_i}\mathrm{Max}\left(1-\sum\frac{x_i^2}{R_i^2},0\right) \tag{2.24}$$

The condensate density is zero outside the TF radius

$$R_i = \sqrt{\frac{2\mu}{m\omega_i^2}}, (i = x, y, z) \tag{2.25}$$

Other parameters, including atom number N, chemical potential μ, energy per atom E/N can also be calculated [56].

□ End of Chapter.

Chapter 3

Experimental apparatus I

A brief description of our single chamber system is presented in this chapter. For more details, please read Xiaoke Li's and Jun Chen's theses [58, 59].

3.1 Vacuum system

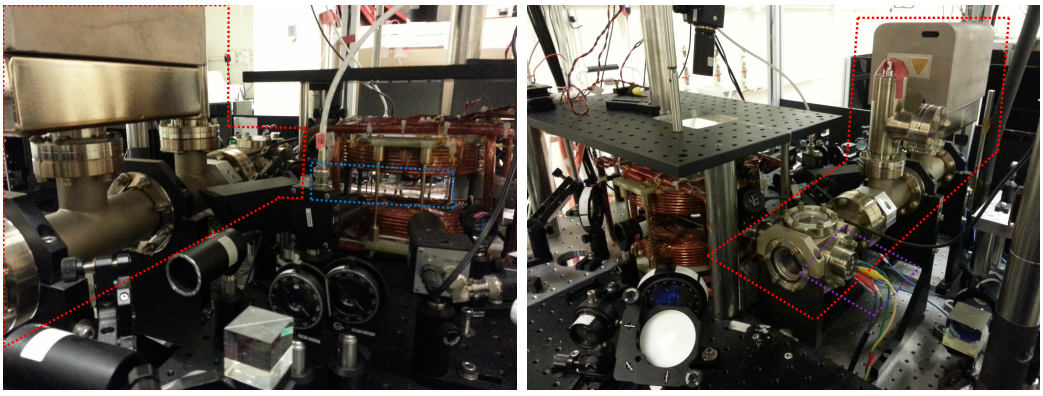

Figure 3.1: Photographs of the single chamber system. The vacuum component, glass cell and dispenser feedthrough are denoted with red, blue and violet dashed boxes, respectively.

The whole setup is constructed with standard stainless vacuum components as shown in Fig. 3.1. We have an uncoated rectangular Pyrex cell

installed in the system, which has the dimensions of 100 mm × 40 mm × 40 mm. An ion pump (45 L/s, Gamma Vacuum) and a titanium sublimation pump (TSP) (Varian Vacuum) maintain the vacuum pressure. The system is prepared with standard UHV procedures. By the readings of the ion pump controller, the vacuum pressure is 1.8×10^{-11} Torr at the position of the ion pump. But it is estimated that the vacuum at the cell is about 5 times worse due to the limit of conductance. This estimation is consistent with 20 s lifetime in QT.

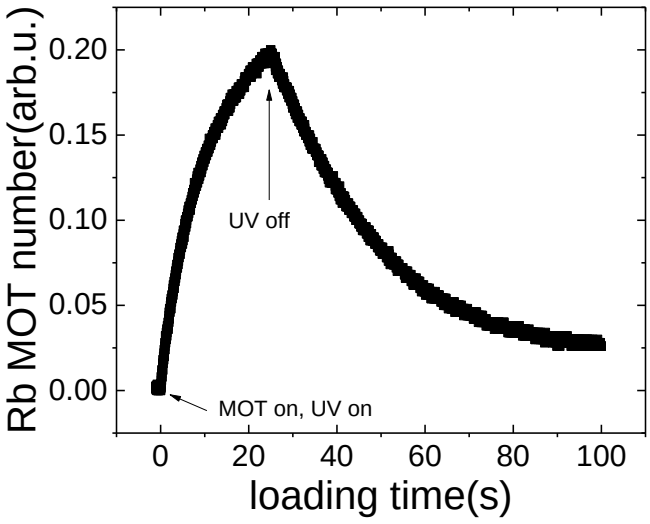

Figure 3.2: MOT loading with LIAD. The MOT number is measured with the fluorescence. After tuning off the UV LED, but keep the MOT beams on, Rb number quickly decrease.

There are two Rb dispensers and two Na dispensers installed in the system. They are directly fixed on a feedthrough with a spot welder. These dispensers are install as close as possible to the cell center. With trial and error, we found that the best choice is to keep one Rb dispenser current at a constant about 1.7 A during experiments while only fire Na disperser once in several months.

In laser cooling, Na(Rb) partial pressure should be high enough for loading a large MOT, while in evaporative cooling, vacuum must be good enough for a long lifetime. In our single cell system, we use the LIAD techniques [60, 61] to manipulate the vacuum pressure. If shined by ultra violet (UV) light (Thorlabs M365L2), atoms are ejected from the surface of the Pyrex cell and enter the cell. Then the Na(Rb) partial pressure increases. After turning off the UV LED, atoms are quickly absorbed on the surface of the Pyrex cell. In this way we can control the vacuum in one second. The effect of LIAD is shown in Fig 3.2. After turning on the MOT beams and the UV LED, the Rb number quickly increase. However, if turning off the UV while keeping the MOT beams on, the Rb number starts to decrease. Fitting the loading curve when the UV LED is on with an exponential function $y = y_0 + Ae^{-t/\tau}$ gives a saturated number about 0.2119. Fitting the data after the UV LED is turned off gives a saturated number 0.01697. Therefore, the number of Rb MOT with LIAD is about 12.5 times of that without LIAD in this measurement.

3.2 Laser cooling and trapping

3.2.1 Na and Rb laser

Since both ^{23}Na and ^{87}Rb have a nuclear spin of 3/2, their energy levels are similar (Fig. 3.3). There are several lasers necessary for cooling and trapping atoms:

Trap laser: A laser near resonant with the cycling transition of $F = 2 \leftrightarrow F' = 3$ provides radiation force to cool atoms;

Repump laser: Since the cooling transition is not an ideal cycling transition, atoms will be populated to $F = 1$ states after scattering about 1000

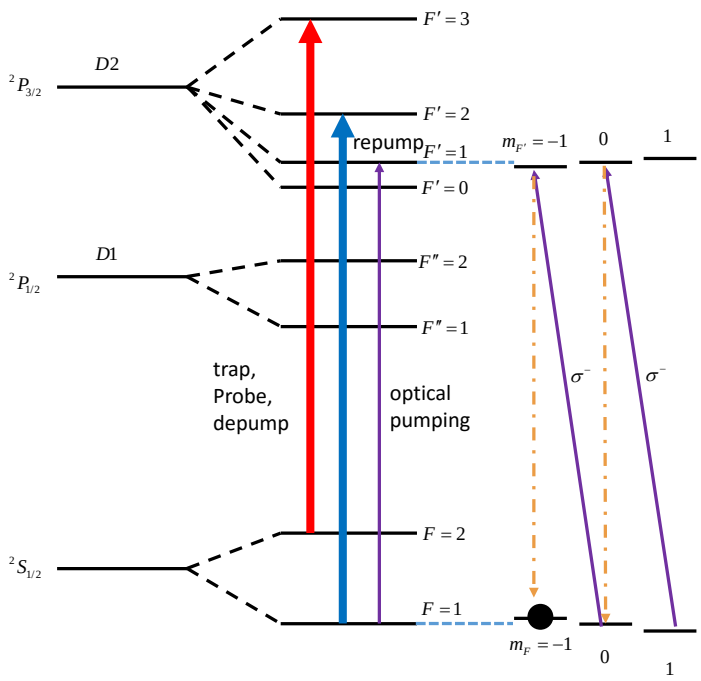

Figure 3.3: Energy levels of ^{23}Na and ^{87}Rb. The ground state $^2S_{1/2}$ splits to F=1 and F=2 states. The D2 line ($^2P_{3/2}$) has four hyperfine states: $F' = 0, 1, 2, 3$. Trap laser, probe laser and depumping lasers are chosen to be near resonant with the $F = 2 \leftrightarrow F' = 3$ transition (red arrow). Repump laser is near resonant with the $F = 1 \leftrightarrow F' = 2$ transition (blue arrow). OP laser is near resonant with the $F = 1 \leftrightarrow F' = 1$ transition (purple arrow). Physical picture of optical pumping is shown on the right panel. Continuously excited by a σ^- laser, atoms transfer magnetization to laser field and eventually populate in $m_F = -1$ states.

photons. These atoms can not see the trapping laser and can not be cooled further. A repump laser, which is near resonant with the transition of $F = 1 \leftrightarrow F' = 2$, is helpful to bring $F = 1$ atoms back to the cycling transition;

Optical Pumping(OP) laser: After MOT and sub-Doppler cooling, atoms are populated in $F = 1$ magnetic sub-states in our present experimental scheme. For loading as many as atoms into magnetic trap, an OP laser is necessary for populating atoms into the $|F, m_F\rangle = |1, -1\rangle$ state, which is

the only trappable state with $F = 1$. This laser is near resonant with the $F = 1 \leftrightarrow F' = 1$ transition and has a σ^- polarization;

Depumping laser: It should be noticed that in order to depopulate atoms in $F = 2$ states in OP process as fast as possible, another laser called depumping laser is turned on. With this beam, $F = 2$ atoms can be firstly excited and then decay to $F = 1$ states. In our experiments, depumping laser is chosen to be the trap laser;

Probe laser: The probing laser is also chosen to be resonant with the $F = 2 \leftrightarrow F' = 3$ transition. Before detection, atoms must be firstly populated into $F = 2$ states with a repump laser or a MW pulse.

Rb laser

There are three laser diodes for Rb lasers. *Repump diode*: One external cavity diode laser(ECDL) is locked to the $F = 1 \leftrightarrow F' = 2$ transition. This diode provides the repump and OP laser beams. *Trap diode*: An ECDL locked to the $F = 2 \leftrightarrow F' = 3$ transition provides the probe laser and the seeding laser for trap beams. *Slave diode*: A diode (Thorlabs LD785-SH300) amplifies the seeding laser to 300 mW. This laser also serves as the depumping laser during optical pumping.

Our lasers are constructed in the Littrow configuration [62]. For locking the lasers, we use saturated absorption spectroscopy generated by directly modulating the diode current with a 50 kHz signal. Feedback is divided into two stages, the faster one for the diode current and the slower one for a PZT. After optimizing the feedback parameters, the lasers have a linewidth narrow than 1 MHz. The locking electronic circuits are based on a modification of JILA's peak lock and side lock circuits.

Na laser

In the first 4 years, the Na laser is generated by a ring dye laser (DYE-SF-077, TekhnoScan). This laser is pumped by a 6 W, 532 nm diode-pumped solid-state(DPSS) laser (Sprout, Lighthouse Photonics). The dye is R6G and we replace it about every three months due to degradation. The typical output power of the dye laser is 600 mW. For stabilizing the dye laser, the ring cavity is locked to an external cavity which is locked to then Na atomic transition with saturated absorption spectroscopy.

Then we buy a Raman Amplifier (MPB Communications Inc) which is seeded with a 1178 nm diode laser (Sacher Lasertechnik). This seeding laser is amplified by the Raman fiber amplifier, which is pumped by an Ytterbium fiber laser. Then the frequency is doubled with a second harmonic generator (SHG). The maximum power of 589 nm laser is about 1.5 W, which is high enough for two apparatuses. The previous dye laser is saved for other spectroscopy experiments. This MPB laser is stabilized by locking the frequency doubled laser to the atomic transition with saturated absorption spectroscopy.

Our optical layouts for Na and Rb lasers are shown in Appendix. For more information, please read Xiaoke Li's and Jun Chen's theses [58, 59].

3.2.2 MOT, CMOT, molasses and optical pumping

MOT beams configuration

We combine the Na and Rb lasers before they are sent into the cell with 2 inch polarizing beams splitters (PBS) as shown in Fig 3.4. One of these large PBS can also help to split one trap laser beam into two laser beams. With this method we can make a "six-beam" configuration. In the usual "three-

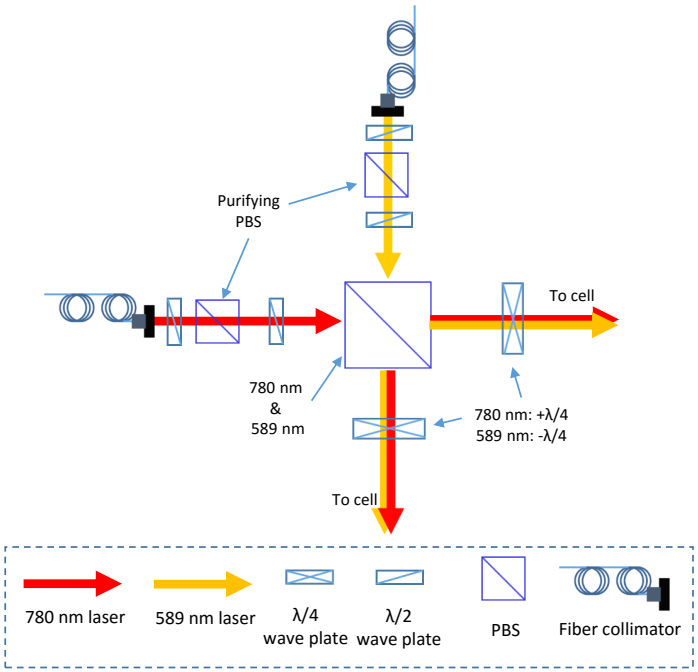

Figure 3.4: Combination of Na and Rb MOT beams. With a PBS we can combine one Na one Rb beam and split both of the beams. There are other PBS to purify the polarization which is important to keep the power balance of the split beams. The lens used for expanding the laser beams are not shown in this figure.

beam" configuration, a MOT beam is sent into the cell and then reflected back. If the atom density is high, there is a shadow in the center of the reflected beam due to the absorption of atoms. As a result of which, atoms may leak from this shadow region. In our "six-beam" configuration, there is no such problem, but the required laser power is doubled.

There is also a slow polarization drift when laser beams pass through the fibers which causes a problem in the power balance of the split beams. Therefore, we add "purifying PBS" to purify the polarizations before the splitting. Consequently the power balance problem becomes a power intensity problem. In our system, the MOT parameters are more sensitive about

the power balance. Therefore, with these purifying PBS, we can achieve a better stability of the MOT.

Rb 3-D MOT

The MOT of ^{87}Rb is a standard technique which has been well established in many groups worldwide and it is relatively insensitive to parameters of the system. We follow their methods to optimize the Rb MOT.

The trap laser is detuned about -19 MHz away from the $F = 2 \leftrightarrow F' = 3$ cycling transition. The MOT beams have a $1/e^2$ beam diameter of 25 mm. The total laser power is 70 mW. The repump laser beams are combined with trap laser beams and have a power of 10 mW. The repump laser is on resonance with the $F = 1 \leftrightarrow F' = 2$ transition. The magnetic field gradient is optimized to be 10 G/cm. The total MOT loading time is about 30 s. We turn on the LIAD UV LED at the begining of the MOT loading and turn it off 1 s before the end of the MOT loading.

Na 3-D MOT

Compared with ^{87}Rb, the Na MOT has some peculiarities. Due to the relatively small hyperfine splittings in the excited state manifold, a full understanding of Na MOT requires a model in which all the excited states are taken into consideration [63]. This makes the optimization process more complex since the intensities and frequencies of trap laser and repump laser are strongly dependent with each other. An example is shown in Fig 3.5. If the repump beam power is high(the red dots), some detailed structures are missing.

In this apparatus, after optimization, the repump beams have a total power of 15 mW and are on resonant with the $F = 1 \leftrightarrow F' = 2$ transition.

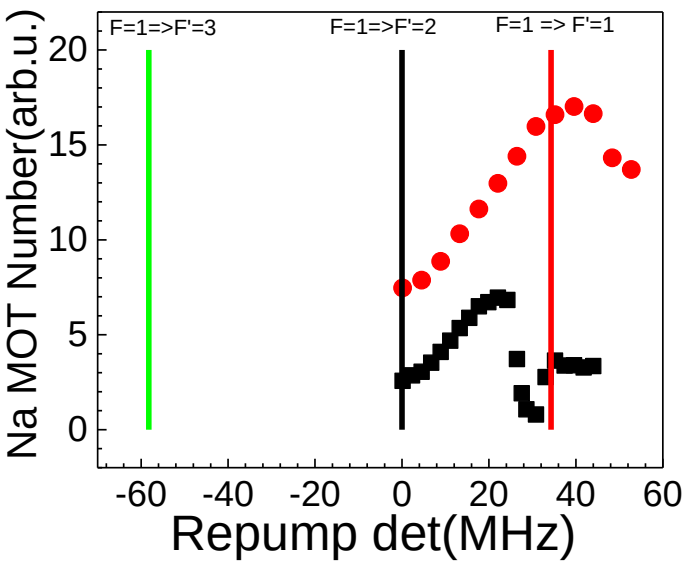

Figure 3.5: Repump laser detuning dependent Na MOT number. The three vertical lines indicates the resonant transition frequencies of Na. The black squares are experimental results when the repump laser has a power of 0.4(arb.u.) while the red dots are experimental results when the repump laser has a power of 0.7(arb.u.).

The trap beams have a total power of 80 mW and are red detuned 15 MHz from the $F = 2 \leftrightarrow F' = 3$ transition. The $1/e^2$ beam diameters are 20 mm.

Combining the two MOTs

One complication of working with double species MOTs is the light induced inelastic collisions, which can limit the number of atoms [64]. Consequently, it is difficulty to load Na MOT since Na is the minor species in our system.

In order to solve this problem, we use a Rb probe laser to push Rb MOT away from Na MOT. With this push beam, the density overlap between Na MOT and Rb MOT decreases and the mentioned loss processes are prohibited. This push beam is turned off 1 s before the compressed MOT (CMOT) so that the two clouds can spatially overlap for optimized QT loading.

CMOT and molasses

After MOTs loading, trap laser detunings are increased and repump laser intensities are decreased to increase the radiation force and decrease photon scattering rate. As a result of which, the heating is suppressed and atom density increases.

Then the molasses is performed by turning off magnetic gradient field, reducing repump laser intensity further and increasing trap laser detuning further.

After optimization, we have 3×10^8 Rb with a temperature about 20μK and 5×10^6 Na with a temperature about 40 μK.

Optical pumping

After 6 ms molasses, a quantization field about 1 G is applied and an OP laser beam is turned on. This laser has a σ^- polarization and is near resonant with the $F = 1 \leftrightarrow F' = 1$ transition. The depumping laser is also turned on at beginning of Molasses. By optimizing experimental parameters, atoms are majorly populated into the $|F, m_F >= |1, -1 >$ states and we have the QT loading efficiency about 70 % for both species.

3.3 Optical dipole trap

Atoms in an inhomogeneous light field experience a force that derives from the gradient of their light shifts. This dipole force is essential to create an ODT which can trap all hyperfine states. For a far detuned light field, the

trap potential and photon scattering rate are [65]

$$\begin{cases} V_{dip}(\mathbf{r}) = -\dfrac{3\pi c^2}{2\omega_0^3}\left(\dfrac{\Gamma}{\omega_0-\omega}+\dfrac{\Gamma}{\omega_0+\omega}\right) I(\mathbf{r}) \\ \Gamma_{sc}(\mathbf{r}) = \dfrac{3\pi c^2}{2\hbar\omega_0^3}\left(\dfrac{\omega}{\omega_0}\right)^3\left(\dfrac{\Gamma}{\omega_0-\omega}+\dfrac{\Gamma}{\omega_0+\omega}\right) I(\mathbf{r}) \end{cases} \tag{3.1}$$

where ω_0 is the atomic transition and ω is the light frequency. Γ is the spontaneous decay rate. $I(\mathbf{r})$ is light intensity.

The potential is attractive for a red detuning while it is repulsive for a blue detuning. The amplitude of potential scales as I/Δ while the photon scattering rate scales as I/Δ^2. Therefore, in order to create a trap with large trap depth but small photon scattering rate, we should increase the beam intensity and increase the detuning.

For multilevel atoms all energy levels have to be taken into consideration

$$\begin{cases} V_{dip}(\mathbf{r}) = \dfrac{1}{2\epsilon_0 c}\sum\limits_e \left[\dfrac{|\langle e|\mathbf{d}\cdot\hat{\epsilon}|g\rangle|^2}{\hbar(\omega_L-\omega_{eg})} - \dfrac{|\langle e|\mathbf{d}\cdot\hat{\epsilon}|g\rangle|^2}{\hbar(\omega_L+\omega_{eg})}\right] I(\mathbf{r}) \\ \Gamma_{sc}(\mathbf{r}) = \sum\limits_e \left[\dfrac{\Gamma_e|\langle e|\mathbf{d}\cdot\hat{\epsilon}|g\rangle|^2}{\Delta_{eg}^2}\right] I(\mathbf{r}) \end{cases} \tag{3.2}$$

ω_{eg} is the resonant transition frequency between excited state $|e\rangle$ and ground state $|g\rangle$. $\hat{\epsilon}$ is the polarization vector. ω_L is the laser frequency. $\mathbf{d}$ is the dipole operator and Γ_e is the spontaneous decay rate for excited state $|e\rangle$.

In the limit that all optical detunings are larger than the hyperfine splittings of excited states, the above expressions can be simplified to

$$\begin{cases} V_{dip}(\mathbf{r}) = \dfrac{\pi c^2\Gamma_{eff}}{2\omega_{0,eff}^3}\left(\dfrac{2+\mathcal{P}g_F m_F}{\Delta_{2,F}}+\dfrac{1-\mathcal{P}g_F m_F}{\Delta_{1,F}}\right) I(\mathbf{r}) \\ \Gamma_{sc}(\mathbf{r}) = \dfrac{\pi c^2\Gamma_{eff}^2}{2\hbar\omega_{0,eff}^3}\left(\dfrac{2+\mathcal{P}g_F m_F}{\Delta_{2,F}^2}+\dfrac{1-\mathcal{P}g_F m_F}{\Delta_{1,F}^2}\right) I(\mathbf{r}) \end{cases} \tag{3.3}$$

Here $\mathcal{P}$ characterizes the laser polarization. ($\mathcal{P} = 0, \pm 1$ for π and $\sigma^{\pm}$ polarization, respectively.) g_F is the landé factor and $\Delta_{2,F}$, $\Delta_{1,F}$ denote energy differences between the particular ground state F and the center of $^2P_{3/2}$ and $^2P_{1/2}$ states, respectively. $\omega_{0,eff} = \omega_1/3 + 2\omega_2/3$ and $\Gamma_{eff} = \Gamma_1/3 + 2\Gamma_2/3$ are the effective transition resonant frequency and the effective spontaneous decay rate. $\omega_i\left(\Gamma_i\right), (i = 1, 2)$ are the frequencies(spontaneous decay rates) of D_i line.

Our ODT is composed of two crossed beams. The two beams intersect with an angle of 62° in horizontal direction. The ODT beams are provided by a 1070 nm multimode fiber laser(IPG photonics) and controlled by two acousto-optic modulators(AOMs) (Gooch&Housego 3110-197). After passing through the AOMs, ODT beams are directly sent into the cell without fibers to clean the spatial profile. The beam waists are 50 μm($1/e^2$) with a quality factor M^2 about 1.2 for both beams. In order to minimize the heating results from interference effect, frequencies of the two beams are shifted to different orders of by the AOMs and two beams are linearly polarized into two orthogonal directions.

The polarization alignment is important especially in the heteronuclear spinor experiments [66]. With a small fraction of circular polarization, the effective magnetic field is large enough to induce an energy shift comparable with the spin dependent interactions. Therefore, we use PBS to purify the polarization before the beams enter the Pyrex cell.

For a Gaussian beam propagating along the z direction, the intensity distribution is

$$I\left(r, z\right) = \frac{2P}{\pi\omega\left(z\right)^2}\exp\left(-\frac{2r^2}{\omega\left(z\right)^2}\right) \tag{3.4}$$

Where $\omega\left(z\right) = \omega_0\sqrt{1 + \left(z/z_R\right)^2}$ is the z-dependent beam waist, ω_0 is the beam waist at focus position(z = 0), $z_R = \pi\omega_0^2/\lambda$ is the Rayleigh range and

P is the total power of this beam.

Expanding this expression within a range $z \ll z_R$ and $r \ll \omega_0$, we get

$$I(r,z) = \frac{2P}{\pi\omega_0^2}\left[1 - 2\left(\frac{r}{\omega_0}\right)^2 - \left(\frac{z}{z_R}\right)^2\right] \tag{3.5}$$

Consequently, we have a harmonic trap

$$V_{dip}(r,z) = V_0\left[1 - \frac{1}{2}m\omega_r^2 r^2 - \frac{1}{2}m\omega_z^2 z^2\right] \tag{3.6}$$

with characteristic parameters: trap depth $V_0 \equiv V_{dip}(r=0, z=0)$, radial trap frequency $\omega_r = \sqrt{4V_0/(m\omega_0^2)}$ and longitudinal trap frequency $\omega_z = \sqrt{2V_0/(mz_R^2)}$. With a 1070 nm ODT, the ratios of the trap depths and trap frequencies of Na and Rb are $V_{Na}/V_{Rb} = 0.35$, $\omega_{Na}/\omega_{Rb} = 1.14$, respectively.

Since the trap depth of Na is much smaller than that of Rb, it is more difficult to load Na atoms into ODT after evaporation in the hybrid trap [67], especially when Rb is present. In order to increase the Na ODT loading efficiency, a 660 nm(Cobolt Flamenco$^{\text{TM}}$) ODT is installed, which provides a repulsive potential for Rb while an attractive potential for Na. With a maximum power of 500 mW, we can make Na and Rb have the same trap depths by carefully tuning experimental parameters. It does help to create a larger double BEC [59].

Another problem of 1070 nm ODT comes from the differential gravity sag. Combing the gravity effect with the harmonic trap potential, the total trap potential becomes $V(z) = m\omega_z^2 z^2/2 + mgz$. The trap center changes to

$$z_{sag} = -\frac{g}{\omega_z^2} \tag{3.7}$$

For a trap with $\omega_{Na} = 2\pi \times 100$ Hz, the calculated differential gravity sag

is $\delta_z = |z_{sag,Na} - z_{sag,Rb}| = 10\mu$m. It is comparable with the size of atomic clouds. Thus δ_z should be minimized for creating a mixture with large density overlap. Since δ_z vanishes for a 946.46 nm ODT [59, 68], we set up a Tapered Amplifier(TA)(m2k-laser GmbH) for this "magic-wavelength" ODT. With a fiber cleaning spatial profile, we can send 500 mW near ideal Gaussian laser beams into the cell. This new ODT will be tested very soon.

In order to calibrate an ODT, it is important to measure the trap frequencies accurately. For a trap frequency smaller than 100 Hz, it is useful to excite a dipole oscillation and then measure the movement of the atomic cloud. The trap frequency can be extracted by fitting the data with a sine wave function. For a larger trap frequency of ω, people usually use the parametric heating method: Temperature of the atomic cloud increases when the ODT power is modulated with a frequency of 2ω. However, this "clean" temperature spectrum is only valid for ideally alignment and a single beam ODT. The non ideal alignments in a crossed ODT make the spectrum more complex [69].

When modulating the ODT power with a frequency of ω_m, there are two effects which can be mathematically expressed as

$$\begin{cases} V_1 = [1 + \epsilon \sin\omega_m t]\, m\omega^2 x^2/2 \\ V_2 = m\omega^2 \left[x - \epsilon_x \sin\omega_m t\right]^2/2 \end{cases} \tag{3.8}$$

V_1 corresponds to the trap depth modulation and V_2 corresponds to the trap center modulation. ϵ and ϵ_x are the relative modulation amplitudes of V_1 and V_2, respectively.

The effect of V_1 can be understood by treating $H_1' = m\epsilon \sin\omega_m t \omega^2 x^2/2$ as

a perturbation. The probability for a transition from $|m\rangle$ to $|n\rangle$ is

$$R_{m\to n} \equiv |\langle m|H_1'|n\rangle|^2 \propto \left|\langle m|x^2|n\rangle\right|^2 \propto \left|\langle m|\left(a^+ + a\right)^2|n\rangle\right|^2 \tag{3.9}$$

Here $|m\rangle, |n\rangle$ are eigenstates of the harmonic trap and $a^+(a)$ is the creation (annihilation) operator of the harmonic oscillator. Therefore, the transition from $|n\rangle$ to $|n+1\rangle$ is prohibited. Only $|n\rangle \leftrightarrow |n+2\rangle$ is significant. Thus the measured resonant peak corresponds to double of the trap frequency. What is more, the heating rate is proportion to ω_m^2 [69]. Therefore the higher the trap frequency, the stronger the heating effect.

For the trap center modulation, $H_2' = -m\omega^2\epsilon_x \sin\omega_m t x$ is the leading term of the perturbation. The transition probabilities are

$$R_{m\to n} \propto |\langle m|x|n\rangle|^2 \propto \left|\langle m|\left(a^+ + a\right)|n\rangle\right|^2 \tag{3.10}$$

Therefore, only transitions of $|n\rangle \leftrightarrow |n+1\rangle$ are significant. In this condition, temperature increases when the modulation frequency equals the trap frequency.

Fig. 3.6 shows a typical parametric heating spectrum in our system. The two higher trap frequencies of the ODT are close to each other and are about 6 times of the lowest trap frequency. The lowest trap frequency is out of range of this measurement. After modulating with different frequencies, the measured spectrum of the atomic size has two peaks. The left peak locates at ω_1 and the right peak locates at ω_2. Since the amplitude of the left peak is larger than that of the right one, the left peak corresponds to the center modulation while the right peak results from the depth modulation. The fitting shows that $\omega_2 = 2\omega_1$, which is consistent with this interpretation.

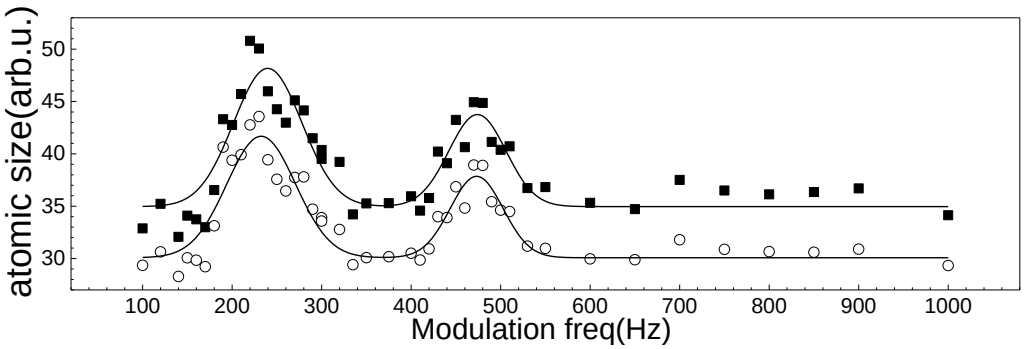

Figure 3.6: Parametric heating spectrum. Solid squares and open circles correspond to measured atomic clouds' size of two different directions after modulating with different frequencies. Solid curves are fitting results of a sum of two Gaussian peaks.

3.4 Magnetic field

Different magnetic fields are used in the experiments. A description of how we create and control the magnetic fields is given in this section.

3.4.1 Coils

In our system, there are two pairs of large coils: one Helmholtz pair for generating a homogeneous magnetic field and one anti-Helmholtz pair for generating a quadrupole magnetic field. Each Helmholtz coil has 7×10 turns(7 layers), and each anti-Helmholtz coil has 7×4 turns(7 layers). These coils are constructed with bared 4 mm out diameter(OD) copper tubes with standard α winding pattern. For isolation, the copper tube is manually winded with 2 layers of 0.05 mm thick Kapton tape. The coils are fixed on a G-10 glass epoxy holder with epoxy 353ND. The dimensions and generated magnetic fields are summarized in Table. 3.1. The homogeneity of the Helmholtz coils is shown in Fig. 3.7.

There are also 3 pairs of square coils mounted near the Pyrex cell. All

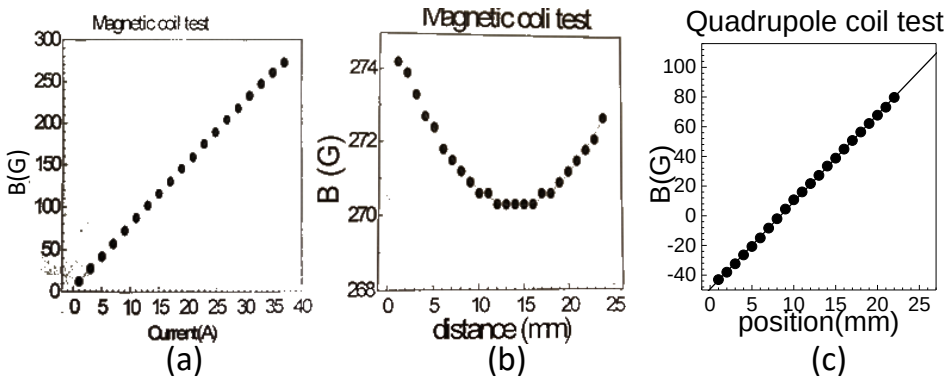

Figure 3.7: Single chamber system coil test.(a) Helmholtz pair generated magnetic field v.s. current. (b) Homogeneity of homogenous magnetic field with 37 A current(axial direction). (c) Anti-Helmholtz pair generated magnetic field v.s. axial position with 50 A current.

Table 3.1: Parameters of coil pairs of single chamber system.

coil	Radius		Separation		magnetic field
	Inner	Outer	Inner	Outer	
Helmholtz	52 mm	88 mm	52 mm	113 mm	7.30(2) G/A
Anti-Helmholtz	34 mm	46 mm	52 mm	114 mm	1.18(1)G $cm^{-1}A^{-1}$

of which are winded with 1 mm OD isolated copper wire. These 3 coil pairs can generate several Gauss magnetic fields along x, y, z directions to shield stray magnetic fields and to provide quantization fields.

3.4.2 Magnetic field control

As shown in Fig. 3.8, these two coil pairs are connected to a 30V-200A power supply(SM30-200, Delta Elecktronika) in parallel configuration. The power supply is set to the constant voltage(CV) mode and controlled by a PC analog signal. Two Hall transducers(LEM IT200S) are used to measure the current through the two coil pairs and the output signals of which are sent to two

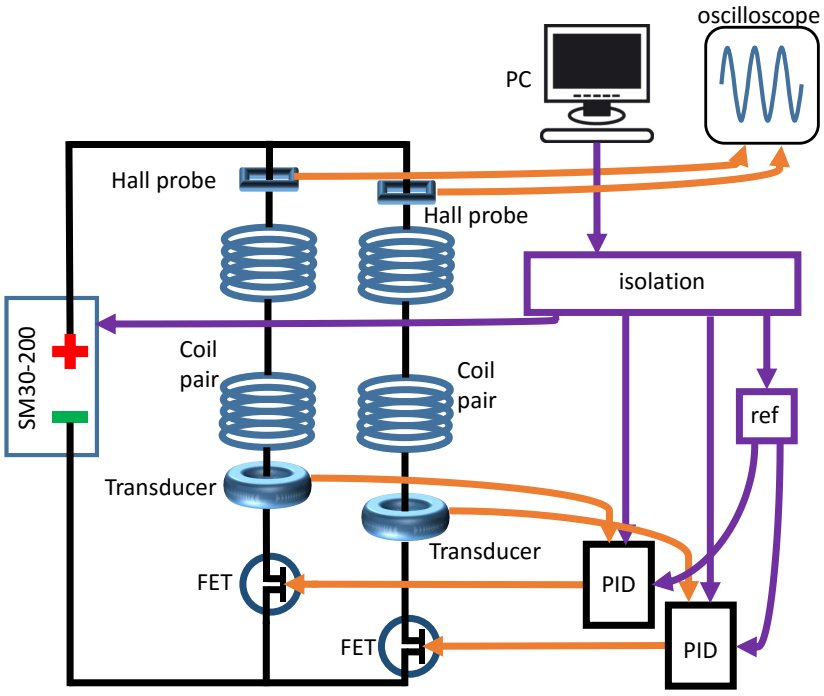

Figure 3.8: Connection scheme of the Helmholtz coils and quadrupole coils.

PID circuits to stabilize the magnetic field via power MOSFETs. Another two Hall transducers(CSNS 300F-RS, Honeywell) are used to monitor the currents in the two coil pairs. There are two kinds of references for the PID circuits. If we try to dynamically control the magnetic fields with a range larger than 80 G, the reference signal is PC's analog signal(isolated PCI 6733 signal). While for a high resolution control, the reference is a "constant voltage + PC signal". A 10 V signal is created with an ultra precision voltage reference REF102C. With voltage dividers, we can create several interesting reference signals out of this 10 V voltage. These references and PC signal are assigned to different channels of a multiplexer, and can be chosen with digital signals. If we want to tune magnetic field in a small range within these interesting magnetic fields, a PC signal is summed with current summing circuit. A higher resolution is achieved with a much larger

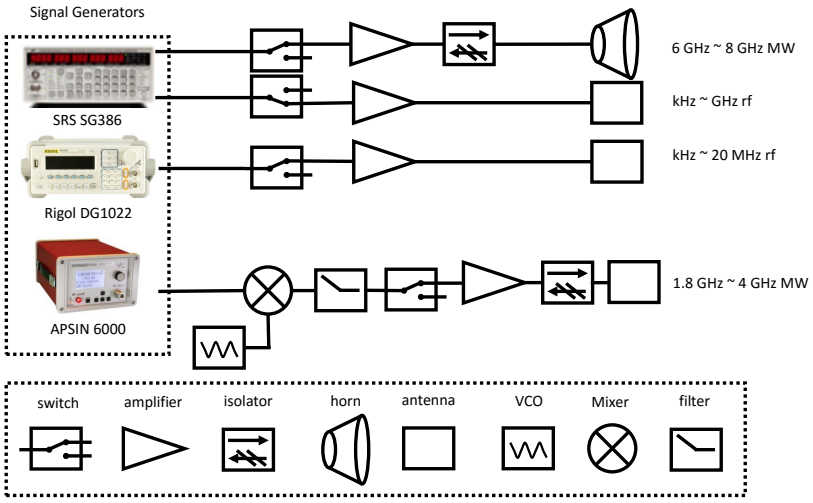

Figure 3.9: Rf and MW system. The three signal generators create different signals: SG 386 generates rf and MW pulse and phase continuous sweep signals, which are used for evaporative cooling, adiabatic rapid passage and MW pulse for Rb $|F = 1, m_F\rangle \leftrightarrow |F = 2, m'_F\rangle$ transitions; Rigol DG 1022 is used for creating rf pulses for Rb(Na)$|F = 1, m_F\rangle \leftrightarrow |F = 1, m'_F\rangle$ transitions at low magnetic fields; APSIN 6000 is used to create pulses and sweeping signals (by mixing a MW pulse with a VCO generated rf signals) for Na $|F = 1, m_F\rangle \leftrightarrow |F = 2, m'_F\rangle$ transitions. The MW horn is used for 6 GHz $\sim$ 8 GHz signals and the "Q-section" antennas are used for 1.8 GHz $\sim$ 4 GHz signals. Other rf signals are transmitted with loop antennas. For the 6 GHz $\sim$ 8 GHz signals, we use amplifier ZVE-3W-183+ (mini-circuits) and L0608-40 (microsemi). For the 1.8 GHz $\sim$ 4 GHz signals, we use amplifier ZHL-16W-43-S+ (mini-circuits). For rf signals, we use amplifier ZHL-1-2W-S (mini-circuits) and ZHL-32A-S+ (mini-circuits).

resistor connected with PC signal in the current summing circuit. In order to separate high current part with the computer, we isolate all digital and analog signals with ICs. After optimizing the PID parameters, we could only achieve a stability about 30 ppm. One reason is that the inductance of a single coil is larger than 0.5 mH which limits the feedback bandwidth smaller than 500 Hz.

3.4.3 Cooling

The maximum Ohmic heating of the coils can be as high as 2 kW. It will burn the coils within a few seconds. Therefore, it is important to cool the coils. In our system, the copper tube is connected with water pipes through Swagelok connecters. The water is cooled with a laserpure 20 chiller(Coherent), which is then cooled by an air-cooled chiller(DLSB 5/30). The change of temperature is less than 15 °C in our experiments.

3.5 Rf and MW system

In our system, electromagnetic radiation fields are used to manipulate atoms. These signals are generated with different signal generators and then sent to atoms with loop antennas for radio frequency(rf), microwave(MW) horn for Rb $|F = 1 > \leftrightarrow |F = 2 >$ transitions and "Q-section" antennas[70] for Na $|F = 1 > \leftrightarrow |F = 2 >$ transitions. For different signals, different amplifiers, switches and other components are used. Details of our rf and MW system can be find in Fig. 3.9.

3.6 Imaging

We use the absorption imaging[71] to detect the properties of an atomic cloud. When a laser beam passes through an atomic cloud, photons of which will be scattered. By recording the intensity profiles of this beam with a CCD (Apogee), information of the atomic cloud can be extracted.

The laser intensity decreases when the laser beam passes through an

atomic cloud according to the Beer's Law

$$\frac{dI\left(x,y,z\right)}{dz}=-\hbar\omega R_{sc}\left(\delta,I\right)n\left(x,y,z\right)=-\sigma_{0}\frac{I}{1+I/I_{sat}+4\delta^{2}/\Gamma^{2}}n\left(x,y,z\right) \tag{3.11}$$

where the photon scattering rate is

$$R_{sc}\left(\delta,I\right)=\frac{\Gamma}{2}\frac{I/I_{sat}}{1+I/I_{sat}+4\delta^{2}/\Gamma^{2}} \tag{3.12}$$

It depends on the detuning δ and the intensity I. $\sigma_0 = \hbar\omega\Gamma/\left(2I_{sat}\right)$ is the resonant scattering cross section and I_{sat} is the saturation intensity.

At low intensity limit $I \ll I_{sat}$, this function can be easily solved as

$$\int n\left(x,y,z\right)dz=-\frac{\ln\left(I\left(x,y\right)/I_{0}\left(x,y\right)\right)}{\sigma_{eg}} \tag{3.13}$$

where $\sigma_{eg} = \sigma_0/\left(1+4\delta^2/\Gamma^2\right)$. The column density $\int n\left(x,y,z\right)dz$ can be calculated thereafter. In usual experiments, three pictures are recorded. $I_1\left(x,y\right)$: laser profiles without atoms; $I_2\left(x,y\right)$: laser profiles after scattered by atoms; $I_0\left(x,y\right)$: all unwanted signals without laser and atoms. Then the column density can be calculated as

$$\tilde{n}\left(x,y\right)\equiv\int n\left(x,y,z\right)dz=-\frac{1}{\sigma_{eg}}\ln\frac{I_{2}\left(x,y\right)-I_{0}\left(x,y\right)}{I_{1}\left(x,y\right)-I_{0}\left(x,y\right)} \tag{3.14}$$

If the intensity of the probe beam is high, careful calibration must be preformed [72].

If $\tilde{n}\left(x,y\right)$ is known, the total number can be directly calculated by integrating the column density. If the trap frequencies are well known, the temperature can also be extracted by fitting the column density distribution. If the trap frequencies are not known, one can use the time of flight(TOF) method to get the temperature. After switching off the trap, atomic cloud

starts to expand according to

$$\sigma^2(t) = \sigma_0^2 + \frac{k_B T}{m} t^2 \tag{3.15}$$

where $\sigma(t)$ is the size of the atomic cloud with an expanding time of t. Temperature can be fitted with measured σ for different t.

In order to simultaneously detect different hyperfine states, one can use the Stern-Gerlach method. By applying a magnetic gradient field, different hyperfine states will be separated if these states have different magnetic dipole moments. Then all of these states ccan be detected in one experimental cycle.

3.7 Computer control system

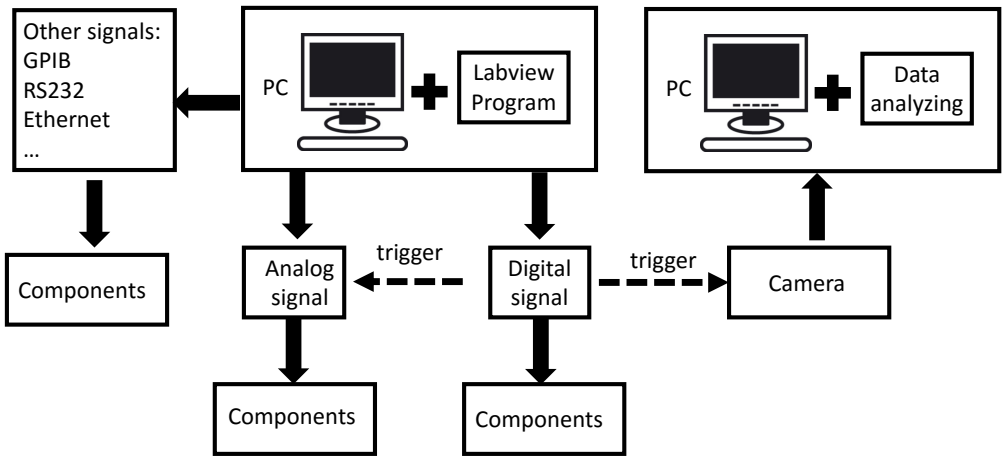

Figure 3.10: Schematic of computer control system.

The control system, as shown in figure 3.10, can be divided into three parts:(1) Digital signal, (2) Analog signal, (3) GPIB, RS232 and Ethernet control. We use a DIO-64(Viewpoint system, PCI interface) to generate 64

output TTL signals. The Logic gate optocouplers 6N137 and buffer amplifiers BUF634 are used to isolate the signals and to boost the output current, respectively. The arbitrary analog signals are generated by three DAC boards(two PCI-6713 and one PCI-6733, National Instruments). All the three boards generate eight 14-bit(PCI-6713) or 16-bit(PCI-6733) signals with 1 MS/s update rates. One PCI-6713 and one PCI-6733 update their outputs when receiving trigger signals from the DIO-64, otherwise previous values are held. With this method, one can avoid writing too much data into the buffers. For a fast ramping process, we write a waveform into the buffer of another PCI-6713. When receiving a trigger, this board continuously generates the whole waveform. For analog signals, differential amplifiers are used to partially isolate the DAC boards with controlled components. The GPIB(RS232, Ethernet) signals are used to control signal generators for evaporative cooling and spin manipulation.

□ End of Chapter.

Chapter 4

Experimental apparatus II

The single cell system has some limitations: (1) It is difficult to increase the numbers of Na and Rb due to the contradictory requirements of vacuum. (2) The optical access is poor and there is no space for more laser beams, optical lattice beams, for instance. (3) Due to the limitation of dimensions of the cell, it is hard to add strong electric fields. So we set up another system for Na-Rb mixture. Since many existing techniques developed in the previous setup are used here, only the modified components will be introduced with details.

4.1 Vacuum system

Details of the vacuum system can be find in Fig. 4.1. It is a two-cell system. The MOT cell has dimensions of 100 mm $\times$ 40 mm $\times$ 40 mm, and is used to collect Na and Rb atoms with LIAD. The science cell (100 mm $\times$ 20 mm $\times$ 20 mm) is used to perform the following experiments such as evaporative cooling. In between there is a differential tube which helps to maintain the vacuum difference between those two cells. Its inner diameter is 8.1 mm and

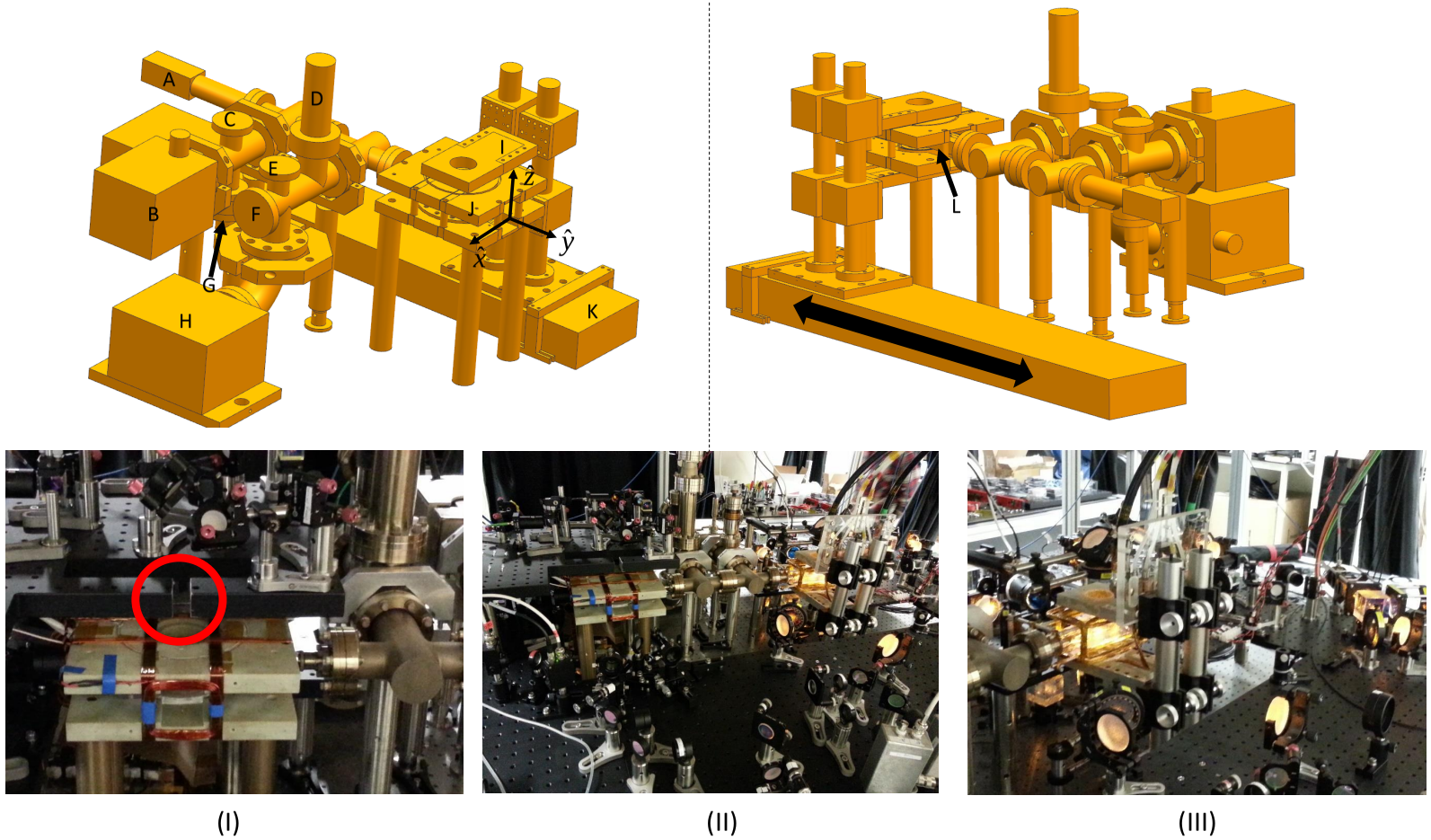

Figure 4.1: 3-D model and photographs of experimental apparatus II. The upper panel are 3D models where some holders are not shown and some components are only shown with schematic figures. A: MOT cell; B: 25 s/L ion pump; C and E: two all metal angle valve(not shown here); D: TSP; F: ion gauge; G: feedthrough; H: 45 s/L ion pump; I: transfer coil; J: Bias coil; K: translation stage; L: Science cell. The translation stage can move from the MOT cell to the science cell (denoted as a double-headed arrow) and it transfers atoms between these two cells. $\hat{x}, \hat{y}, \hat{z}$ are defined directions of this system. Photographs of this apparatus are shown in lower panel: (I) details of the science cell; (II) whole system; (III) details of the MOT cell. The red circle denotes the slit which is important to mitigate the eddy current effect.

Table 4.1: Parameters of the coils in the two-cell system. Column "N" denotes the "number of turns × number of layers". Column "B" is the generated magnetic fields with a unit of "G/A" and column "Gradient" denotes the generated gradient field with a unit of "G/cm·A^{-1}". The unit of length is mm. The note "m" indicates a measured value while "cal" indicates a calculated value.

coil	N	Diameter		Separation		B	Gradient
		Inner	Outer	Inner	Outer		
Bias	4×4	74.2	103.6	30	59.5	3.23(1)(m)	0.77(m)
Transfer	6×4	50.0	94.2	84	113.5		0.66(1)(m)
SG1	20×36	49.4	62	32	50		86(cal)
SH1	3×3	62.2	70.6	30	36.3	2.4(cal)	
SH2	3×4	123.2	131.6	59.5	70	1.42(m)	

length is 12.5 inch.

There are two ion pumps (25 L/s and 45 L/s, Gamma Vacuum) and one TSP to maintain the vacuum. An Ion gauge (Duniway) measures the vacuum pressure near the science cell. As shown in Fig. 4.2, two Rb dispensers and two Na dispensers (Alvatec) are installed in the system. The four dispensers are mounted on a homemade ceramic holder which is fixed on the differential tube. Dispensers are connected with a feedthrough via bare copper wire (Accu-Glass). Ceramic beads are used to isolate the copper wire with other vacuum components. In order to avoid wasting Na and Rb atoms, the dispensers are placed in the MOT cell which makes released atoms have a large possibility to be absorbed by the MOT cell. All dispensers are placed a little upwards to prevent atoms flow out due to gravity. Due to the limitation of dimensions, we have to adjust the dispensers' position many times when assembling the vacuum. Maybe due to the fatigue of metal, one Na dispenser touches the cell (denoted by a red circle in Fig. 4.2) after vacuum

preparation. Fortunately this problem did not happen during the baking process and we find this problem early enough. Otherwise the cell would explode since the temperature of dispenser is as high as 400 °C when firing it. After making sure that it is okay when firing other dispensers, we bear this problem and plan to fix it when upgrading the system.

We prepare the ultra high vacuum with the routing methods. But the vacuum can only reach 10^{-10} Torr. (Judging from the ion pump readings. We did not install the ion gauge at that time). After checking leaks with methanol, the reading lowers down to several 10^{-11} Torr. Several months later, we surprisingly find that the vacuum reading increased to 10^{-10} Torr again. After struggling with this problem for several weeks, we find that it results from a "partially" leak in a customized vacuum component. By applying some methanol, the ion pump reading decreases again although it can only keep there for several minutes. It is believed that this leak can be blocked due to contraction of metal when the methanol evaporates.

We have to prepare the vacuum for a second time after the leak is sealed by vacseal (Vaceal Inc.). Then we have a vacuum which can provide a lifetime of atoms more than 200 s.

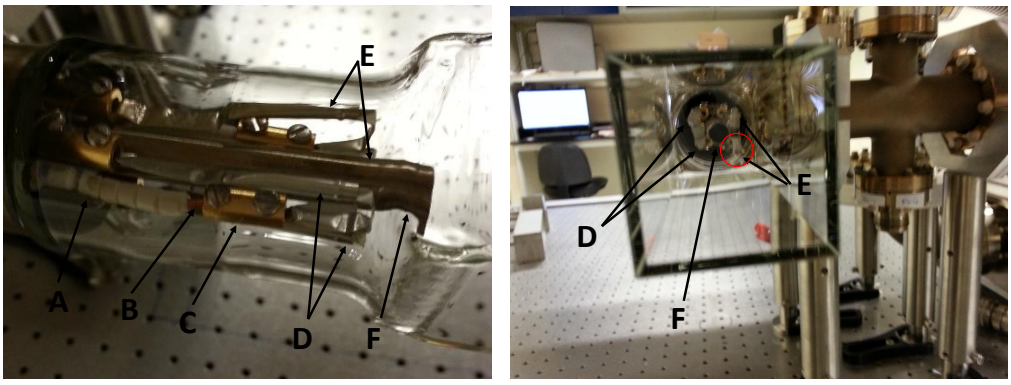

Figure 4.2: Connection of dispensers. A: ceramic beads; B: bare copper wire; C: connector; D(E): Rb(Na) dispensers; F: differential tube. Red circle denotes where a Na dispenser touches the glass cell.

4.2 Magnetic field

There are two major coil pairs in this setup, a transfer coil and a bias coil. The transfer coil is in an anti-Helmholtz configuration and is mounted on a mechanical translation stage (Parker). The bias coil can be changed between a Helmholtz configuration and an anti-Helmholtz configuration with an H-bridge composed of 4 high voltage relays (LEV200, Tyco Electronics). The transfer coil provides a QT potential for collecting atoms in MOT loading as well as transferring atoms between the two cells. The bias coil provides a QT potential during evaporative cooling and a homogeneous magnetic field in other experiments.

The transfer coil and bias coil are winded with daglass isolated square hollow copper tubes which have an outer dimension of 0.125 inch and an inner diameter of 0.0625 inch (S&W Wire Co.). The coils are winded with a back-winding method. This winding method is helpful to reduce the stray fields as well as to simplify the designing of coil holders.

Besides these two coils, there are several other coils for different proposes: Six shim coils at both MOT and science cell for shielding stray magnetic fields; A small gradient coils(SG1) is used to generate a gradient magnetic field for Stern-Gerlach separation and free atoms removing during Feshbach molecules creation; A Helmholtz coil(SH1) for a small homogenous magnetic field with fast controlling speed. The z-direction shim coil of science cell (SH2) is designed to be in an Helmholtz configuration, which can also generate a homogenous magnetic field with several Gauss.

All the dimensions and parameters of these coils are listed in Table. 4.1. And details of coils construction can be find in appendix C.

The two major coils are connected in parallel to a 16.5 V - 400 A power supply (Delta Elektronika). The maximum achievable magnetic field gradient

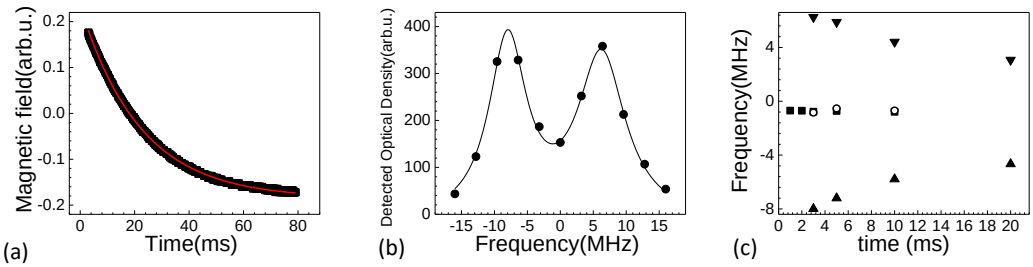

Figure 4.3: Eddy current effect. After tuning off a 340 G magnetic field at $t = 0$, there is a magnetic field generated by eddy current. (a) is the measured magnetic field near the science cell. The red curve is the fitted results of an exponential decay function which gives a time constant of 22.0(1) ms. (b) is the measured Rb probe line shape at $t = 3$ ms. The black curve is a fitting of a sum of two Gaussian functions. (c) is a summary of the eddy current effect. Triangles are fitted peaks for different t for original setup. Black squares are resonant peaks when all components are taken away. (No double-peak structure at this time). Open circles are resonant peaks after cutting the Al breadboard. (There is also no double-peak structure.)

is about 250 G/cm and the highest homogenous magnetic field is 1200 G, which is larger than all interesting magnetic fields in our Na-Rb system. With a PID control circuit, the magnetic field has a stability about 20 ppm.

In our setup, we can shut down the current of the bias coil in 200 μs. However, by measuring the resonant probe frequency after turning off the magnetic field, we find that the total magnetic field caused by the eddy current decays with a time constant about 22 ms, as shown in Fig. 4.3(a). The eddy current effect makes it is impossible to change the magnetic field at high speed. By taking away all components near the science cell piece by piece, we find that all the metal components contribute the stray magnetic field especially the Aluminum breadboard on top of the cell, where there is a hole for optical access. This problem is partially solved by cut a slit in this breadboard as shown in Fig. 4.1. As shown in Fig. 4.3(a), before cutting this slit, there is a double-peak structure in the probe line shape after turning off

the high magnetic field. After cutting the slit, we do not observe the double-peak structure and the resonant frequency is the same as the case when all components are taken away.

Other coils except the SG1 are powered by the diode current driver modules (LD3000R, Thorlabs), which have a stability about 10 ppm and a modulation bandwidth about 1.1 kHz. Solid state relays (D1D40, crydom) are used to switch on and off the currents in 10 μs.

The SG1 coil is connected with a 60V - 10 A power supply. There are two kinds of switches for this coil: A solid state relay which is used to quickly turn on and off the current; Two mechanical relays can isolate SG1 and the power supply. The mechanical relays are switched on(off) about 5 ms before(after) turning on(off) the solid relay.

4.3 Atom transportation

The transfer coil is mounted on a holder which is fixed on the computer controlled mechanical translation stage. This track is driven by a servo motor. Parameters including travel distance, maximum velocity, acceleration and deceleration are firstly loaded into the controller. Then the track is controlled by TTL signals. By moving the transfer coil from the MOT cell to the science cell or vice versa, we can transfer atoms between these two cells.

There are several possible heating and loss mechanisms during transferring process: (1), It is possible that atom can not pass through the differential tube due to misalignment. (2), The magnetic gradient of the transfer coil is too small, as a result of which the size of the atomic cloud is so large that atoms collide with the differential tube. (3), Acceleration or deceleration is so large that atoms can not follow the QT. (4), Acceleration is too small that atoms spend long time in the MOT cell where the lifetime is short.

The alignment of the track is optimized by recording the atom number when the QT goes a round trip to different position and by measuring the atom position in the science cell. Then we optimize the track parameters, QT gradient value as well as dispensers current for the largest but coldest atomic sample in the science cell.

The repeatability of the track is about 5 μm. In order to get a better stability of our system, atoms will be firstly loaded into the science QT after atom transportation. The science QT is created by setting the bias coil to an anti-Helmholtz configuration. After optimization, we get an finish the transportation and loading in 5 s. The total efficiency is 70 % and no obvious heating is observed.

The electric noise of the track is large even if it does not move. Therefore, we turn off the track when it returns to the MOT cell. With this method, no obvious electric noise pollution is observed in following experiments.

4.4 Other components

Many established techniques in the single chamber system are used in this system.

The Rb laser are similar with that of the single chamber system except that the two ECDL diodes are replaced by two DFB diodes (Eagleyard Photonics). For the Na lasers, these two apparatus share the the Raman fiber amplifier.

For the ODT, we use a Nufern fiber amplifier now. The output is about 15 W. This amplifier is seeded with a single frequency seeding laser(Laserglow Technologies).

The rf and MW system is also similar with previous one. But since the dimensions of the new science cell is smaller, the antennas can be placed

closer to atoms and consequently the Rabi frequencies are larger than before.

We use absorption image in the system. Both Na and Rb probe beams are along the $+\hat{y}$ direction and pass through the differential tube. After scattered by atoms, Na and Rb probe beams are separated by a PBS and then detected with two CCDs(Point Grey).

□ End of Chapter.

Chapter 5

Creation of BEC in the hybrid trap

We use a hybrid trap for evaporative cooling. The hybrid trap is firstly realized by Lin *et al.* [67] and then used in Rb-Cs mixture experiments [73]. Compared with the traditional Ioffe-Pritchard magnetic trap, it is easy to design and construct. What is more, compared with plug trap, no additional blue detuned ODT laser is needed. The details of cooling Rb and Na to degeneracy is introduced in this chapter.

5.1 Hybrid trap

Rf(MW) evaporation are widely used to cool atoms down to sub-μK regime. The basic idea is that a rf(MW) field can transfer atoms from a low field seeking state (trappable states) to a high field seeking state (untrappable states), and those atoms are then repelled out of the trap. By tuning the rf(MW) frequency, one can selectively remove the hottest atoms. Followed by thermalization between remaining atoms, the temperature of system is

lowered.

The Rf(MW) evaporation can be easily realized in a QT. However, BEC can not be created in a QT due to the "Majorana loss" problem [74]. If the rate of change of magnetic field direction ω_B is larger than the Lamor frequency ω_L, atoms can undergo a nonadiabatic transition to an untrappable state. For an atom with mass m and velocity v placed at position r of a QT with gradient B', the Lamor freuqency is $\omega_L = \mu_B g_F m_F B(r)/\hbar = \mu_B g_F m_F B' r/\hbar$. The ω_B can be calculated as $\frac{dB(r)}{dt}/B(r) = v/r$. Therefore the radius of loss region is

$$r_M = \left(\frac{v\hbar}{\mu_B g_F m_F B'}\right)^{1/2}. \tag{5.1}$$

A more careful analysis [74, 67] reveals that the Majorana loss rate is scaled as

$$\Gamma_M \propto \frac{\hbar}{m}\left(\frac{\mu_B g_F m_F B'}{k_B T}\right)^2 \tag{5.2}$$

At low temperature, the Γ_M is so large that the BEC cannot be created. In order to solve the Majorana loss problem, other kinds of traps are designed. In a time averaged orbiting potential(TOP) trap[74], atoms can not follow the rotation of the QT center and an effective trap with no zero magnetic point is created. For the Ioffe-Pritchard(IP) trap[75] and the quadrupole-Ioffe-configuration(QUIC) trap[76], there is no zero magnetic field point thanks to careful designing of the coils. In a combination of QT and ODT potentials, atoms can be pushed(plug trap)[10] or pulled(hybrid trap) away from the zero magnetic field point.

The hybrid trap is composed of a QT and a displaced single beam ODT.

The total trap potential is

$$U(x,y,z) = \mu B' \sqrt{\frac{x^2+y^2}{4} + z^2} + mgz - U_0 \exp\left\{ -\frac{2\left[x^2 + (z-z_0)^2\right]}{w_0^2\left(1 + \left(y\lambda/\pi\omega_0^2\right)^2\right)} \right\} + E_0 \tag{5.3}$$

The QT is aligned along the z-direction and has a gradient about B'. The single beam ODT with wavelength λ propagates along y-direction. U_0, ω_0 are the trap depth and beam waist of the ODT. The offset between the ODT focus and the QT zero point is in the z-direction and has a value of z_0. The gravity is along z-direction and has an acceleration of g. E_0 is determined by choosing $U(0,0,0) = 0$. Fig. 5.1 shows an example of the hybrid trap potential. The effective trap depth of the whole trap potential is defined as the difference between trap minimum and the QT zero point if the gradient magnetic field can compensate the gravity. The black arrow indicates the trap depth for a 160 G/cm hybrid trap. As the gradient decreases, the trap depth increases and reaches its maximum value when the gradient magnetic field balance the gravity force (30.4 G/cm for ^{87}Rb $|1,-1\rangle$ and 8.0 G/cm for ^{23}Na $|1,-1\rangle$). Thus it is helpful to mitigate Majorana loss rate by lowering B'.

When lowering the gradient field, the trap is as tight as before. It benefits for a faster evaporative cooling.

The single beam ODT alignment is divided into four steps:(1) Compensating the background magnetic field. The earth magnetic field and stray magnetic fields contribute a total field about 0.5 G. With a QT about 160 G/cm, the zero point shift is about 30 μm. It is comparable with the beam size of ODT. Thus it is necessary to carefully tune the magnetic fields generated by shielding coils. Firstly, we set a current for a shim coil and measure the atoms position r for different magnetic gradients B'. With a fitting func-

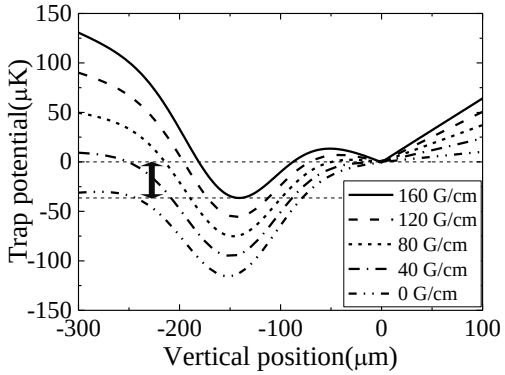

Figure 5.1: Rb hybrid trap potential in $x, y = 0$ plane with different magnetic gradient fields. The trap depth of ODT is $U_0 = 100\mu$K, beam size is $\omega_0 = 90\mu m$, and the offset is $z_0 = 150\mu m$. Where E_0 is choose to make $U(0, 0, 0) = 0$.

tion $r = r_0 + B_o/B'$, we can get the desired position r_0 of atoms when the background magnetic field in this direction B_o is zero. Then we change the value of this shim coil to place atoms at r_0, which is the desired value for this shim coil. For a better alignment, we load atoms into XODT and use a rf(MW) pulse to measure the Zeeman energy difference between two hyperfine levels. With this method, we can compensate the background field with an accuracy about 1 mG. (2) Aligning ODT position in the horizontal direction. By placing the ODT slightly lower than the QT center, and then scanning the ODT focus horizontally, we can find two peaks and a dip in the number spectrum Fig. 5.2. The peak corresponds to a position where the ODT suppresses the Majorana loss. If the ODT is right under the QT center, the Majorana loss is enhanced. It is this position corresponds to the dip in number spectrum and peak in the temperature spectrum. (3) The ODT is directly placed at the QT center in vertical direction since we can image the atoms' vertical position. (4) Fine tuning the offset z_0 by optimizing the atom number and temperature.

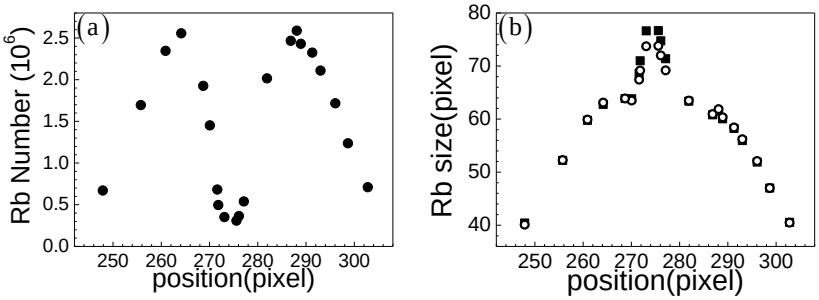

Figure 5.2: Hybrid trap alignment in horizontal direction. By scanning the single beam ODT position, there shows a dip in the number spectrum(a) and a peak in temperature spectrum(b). The open circles and black squares in (b) are measured atomic cloud's size after TOF in two directions.

5.2 Rb BEC

We create the Rb BEC in this setup by firstly evaporative cooling in the hybrid trap and then continue the evporative cooling in the XODT by lowering the laser power.

After laser cooling and optical pumping, we can load more than 10^8 Rb$|1,-1\rangle$ into QT with an axial gradient of 160 G/cm. The temperature is about 90 μK and the estimated PSD is about 2.1×10^{-6}. After QT loading, a single beam ODT with a $1/e^2$ beam waist of 60 μm is ramped up to 5 W in 200 ms to form a hybrid trap. Then we perform the MW evaporation by sweeping the MW frequency. This sweep is divided into several sections with different sweeping speed and MW power. These parameters are chosen by optimizing the evaporation efficiency section by section. After evaporation to 6822 MHz, we typically have 2.5 $\times 10^7$ atoms with a temperature of 29 μK.

In order to load Rb atoms into the XODT. B' is ramped down to a value about 30.5 G/cm, just enough for compensate the gravity. At the same time another ODT beam is ramped up to about 5 W to form the XODT. The

loading has an efficiency about 15%. After the loading, we have an atomic cloud with a temperature about 14.6 μK and a PSD about 3 $\times 10^{-3}$.

Evaporation continues in the XODT by lowering the laser power. We control the trap power following a scaling law $P(t) = P_0 (1 + t/\tau)^{-\beta}$ [77]. The parameters τ and β are experimentally optimized. After 3.5 s evaporation in XODT, we observe the onset of the phase transition. At the transition point, the temperature is 240 nK and number is 2.7 $\times 10^5$. We can obtain a quasi-pure BEC with 10^5 atoms by lowering the XODT further. Fig. 5.3(a) shows the density distributions and absorption images with 30 ms TOF near the phase transition. The whole evaporation trajectory is shown in Fig. 5.3(b). We can get an evaporation efficiency $\alpha = -\log(PSD/PSD_0)/(\log(N/N_0))$ about 2.2 in the hybrid trap and 2.7 in the XODT.

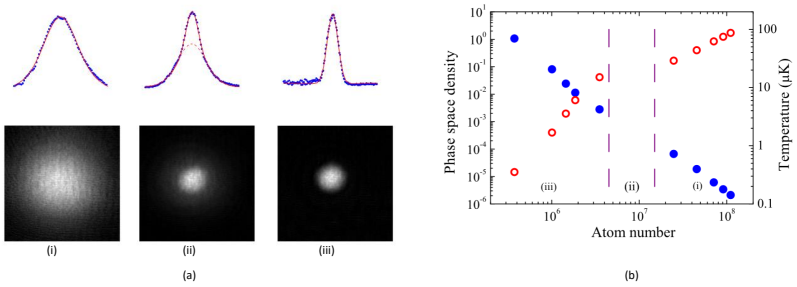

Figure 5.3: (a)Absorption images with 30 ms TOF. (i) thermal cloud just before phase transition,(ii) bimodal distribution and (iii) quasi-pure condensate. Field of view: 900μm $\times$ 900μm. Upper panel is the integrated OD of data(blue dots) and fitting results of Gaussian or/and parabola functions(red solid line). (b) is the evaporation trajectory and section (ii) corresponds to the XODT loading.

By ramping down the single beam ODT power and the magnetic gradient field at the last stages of the MW evaporation, we can also produce a quasi-pure Rb BEC of 10^5 atoms in the hybrid trap without a loading into the XODT.

5.3 Double species BECs

In our system, the Na number is much smaller than that of Rb. Therefore, we choose sympathetic cooling of Na in the Hybrid trap.

The interspecies collision rate $\gamma = \bar{v}n\sigma$ depends on the elastic collision cross section $\sigma = 4\pi a_{\mathrm{NaRb}}^2$, density overlap n and mean thermal relative velocity $\bar{v} = \sqrt{8k_B\left(T_1/m_1 + T_2/m_2\right)/\pi}$. a_{NaRb} is the interspecies s-wave scattering length. Considering every two-body collision, the energy transfer is

$$\Delta E = \frac{4m_1m_2}{\left(m_1+m_2\right)^2}k_B\left(T_1 - T_2\right) \tag{5.4}$$

which is reduced by a factor of $\xi = 4m_1m_2/\left(m_1+m_2\right)^2$ with respect to the collisions with two equal mass particles [78]. It is known that 2.7 collisions are necessary for the thermalization of equal mass particles [79]. In our Na-Rb system, $\xi = 0.66$ and 4.1 collisions are necessary for thermalization. Consequently, the temperature difference ΔT between Na and Rb obeys an equation of

$$\frac{d\left(\Delta T\right)}{dt} = -\frac{\gamma\xi}{2.7}\Delta T. \tag{5.5}$$

The thermalization process is measured as Fig. 5.4. We perform a quick evaporation of Rb in the hybrid trap and then measure the temperature evolution of Na. Since Rb number is much larger than Na number, there is no temperature change of Rb in this measurement. Fitting the data gives an interspecies scattering length $a_{\mathrm{NaRb}} = 115(20)a_0$, which is about 57% larger than the more accurate value of 73 a_0 [3]. The discrepancy is probably because γ is not a constant during the measurement and the number 2.7 is not accurate in a hybrid trap.

The different trap potentials of Na and Rb in a 1064 nm XODT make the creation of dBECs difficult in three aspects: (1) The Na has a shallower

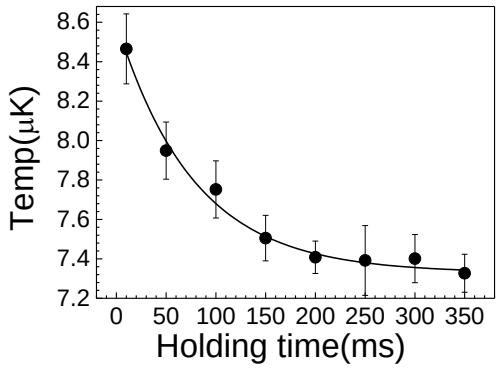

Figure 5.4: Temperature evolution of Na after quickly cooling Rb. The error bar is standard deviation of 3 measurements.

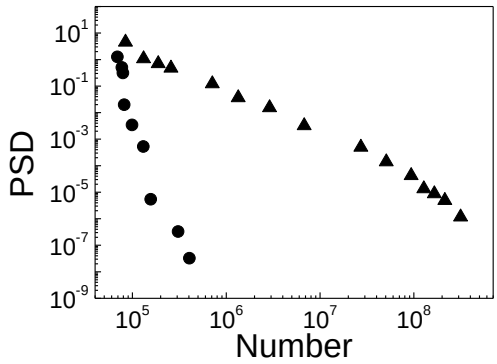

Figure 5.5: Symperthetic cooling in hybrid trap. Triangles and dots are data of Rb and Na respectively.

effective traping potential in the hybrid trap and consequently Na has a shorter lifetime compared with Rb; (2) It is difficult to load Na into XODT due to the much smaller trap depth; (3) We have to use Na sympathetically cooling Rb in the XODT. Therefore we make two modifications of the evaporation. Firstly, we displace the ODT focus in the radial direction of the QT(horizontal direction), in which the magnetic gradient field B' is a half of that of the axial direction. As shown in Fig. 5.1, the effective trap depth becomes larger with this method. We also decompress the QT during MW evaporation which helps to reduce Γ_M by increasing the effective trap depth

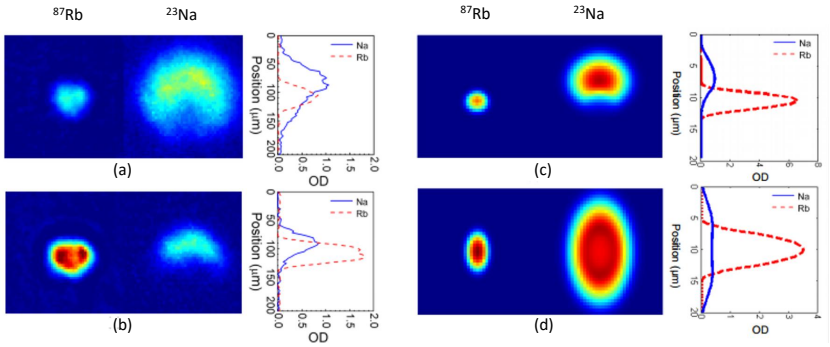

Figure 5.6: DBECs in XODT at the background scattering lengths. (a) and (b) are absorption images in horizontal direction after 10 ms TOF for 3.5 $\times$ 10^3 Rb + 3.2 $\times$ 10^4 Na and 8.5 $\times$ 10^3 Rb + 1.3 $\times$ 10^4 Na, respectively. Simulated in trap density distribution with corresponding parameters of (a) is shown as (c)(horizontal view) and (d)(vertical view). On the right side of each pseudo colour image, the figure shows corresponding cross sections for Na(Blue solid line) and Rb(Red dashed line).

and lowering the temperature of the atomic clouds. The atomic density also decreases which reduces the three-body loss rate.

As shown in Fig. 5.5, after optimizing the experimental parameters, the evaporation efficiencies of Rb and Na in hybrid trap are measured to be 1.7 and 9.5 respectively.

After MW evaporation, Na and Rb are loaded into the XODT and the evaporation continues by lowering the XODT power. By carefully tuning the number ratio of Na and Rb, dBECs can be created. In our case, Na firstly reaches the phase transition point since it has a larger number and higher trap frequencies.

The density distribution of dBECs depends on the ratio of inter- and intra-species interaction strengths. If the interspecies interaction is repulsive and larger than the intraspecies interactions, the dBECs are immiscible. It is the case for our Na-Rb dBECs with background scattering lengths. This phenomenon has been observed as well as studied by numerical simulation.

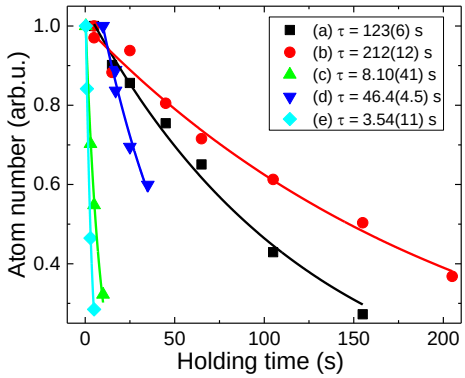

Figure 5.7: Measured lifetime of Na and Rb in different conditions: (a) and (b) are Na and Rb lifetime after loading into hybrid trap separately, (c) and (d) are Na and Rb lifetime when evaporative cooled to about 9 μK in hybrid trap. (e) is Na lifetime in pure QT with a temperature about 9 μK. Solid curves are fitting results of exponential decay. These data are measured in our apparatus II.

Fig 5.6 shows the absorption images and numerical simulation results of dBECs. The Na BEC has a crescent shape rather than a doughnut shape in (a), (b) and (c). It is because that there are gravity sag between Na and Rb, which makes the system asymmetric in vertical direction. However, the system is predicted to have a cylindrical symmetry in horizontal direction, which makes Rb surrounded by Na as shown in (d).

In order to create larger dBECs in XODT, we also add the 660 nm ODT in the system, which can tune the trap depths of Na and Rb. It has been shown that with this new ODT, we can create 7.3×10^4 Rb + 1.1×10^5 Na dBECs. The details of this upgrade can be found in Jun Chen's thesis [59].

Although the dBECs can be created in our hybrid trap, the Majorana loss of Na is still a problem especially at low temperature. As shown in Fig. 5.7, Na and Rb have a lifetime about 123 s and 212 s respectively when loaded into the hybrid trap, where they have a temperature about 150 μK. The difference lifetimes of Na and Rb results from different Γ_M. After evaporation to 6832

MHz, the temperature of mixture is about 9 μK. Rb lifetime is about 46 s while Na lifetime is only 8 s. And the lifetime of Na is 3.5 s in a pure QT. We can see that the hybrid trap can only partially suppress the Majorana loss. Therefore, it benefits for creating larger dBECs with other kinds of traps, plug trap for instance.

In conclusion, we have created dBECs with evaporative cooling and sympathetic cooling in the hybrid trap and ODT. Although there are some limitations, the hybrid trap does help to partially suppress the Majorana loss.

□ End of Chapter.

Chapter 6

Double species BEC with tunable interactions

Feshbach resonance(FR) is a powerful tool to tune the interactions in cold atoms. In this chapter I will firstly introduce our experimental details of observation of Na-Rb interspecies FRs. Then the creation of dBECs with tunable interactions is presented as an example of using these FRs. This chapter based on our publications of [3] and [53]

6.1 Interspecies Feshbach resonances

6.1.1 Observation of Feshbach resonance

Since the first observation of FRs in Na atoms [14], many methods have been used to find and characterize the FRs: loss and heating spectrum, magnetic field dependent BEC size [80], magnetic field dependent Feshbach molecule(FM) binding energies [81, 82], association and dissociation of Feshbach molecules [83, 84, 85], and so on.

The most widely used method is measuring the loss and heating spectrum.

For a homonuclear ultracold atomic sample loaded into ODT, the density evolution can be described by the following equation

$$\frac{dn\left(\mathbf{r},T\right)}{dt}=-\gamma n\left(\mathbf{r},T\right)-\beta n^{2}\left(\mathbf{r},T\right)-\alpha n^{3}\left(\mathbf{r},T\right). \tag{6.1}$$

There are three loss mechanisms:

One-body loss: γ term results from scattering with background atoms, photo scattering with ODT beams and evaporation effect. In typical experiments, all these three processes are slow and can be neglected.

Two-body loss: When two alkali atoms colliding, it is possible to exchange the valence electrons of these two atoms, which is called spin-exchange collisions. The magnetic dipole-dipole interactions V_{dd} couple the orbital angular momentum and electron spin angular momentum. The orbital angular momentum changed collisions due to V_{dd} are called dipolar relaxation. In these two processes, the channels before and after collision are different. Energy difference between these two channels are released to the kinetic energies of atoms. Consequently, atoms run away from the trap since ΔE is much larger than the trap depth.

Three-body loss: α results from the three-body recombination process in which three atoms collide to form a diatomic molecule and an atom. The energy released by the binding energy of the molecule goes into the kinetic energies of the recoiling atoms and the formed molecule. Consequently, all of these three atoms are lost. Since $\alpha \propto n^{3}a^{4}$ [86], the three-body loss rate is sensitive to the scattering length.

Usually heating is associated with two-body and three-body loss. The loss processes prefer to occur at the trap center where the atoms have the highest density and lowest energy. Consequently when the low energy atoms are lost, the remaining atoms will have a higher temperature after thermalization.

By carefully preparing the system, three-body loss dominate, especially near a FR. It is this loss and heating indicate a FR. This scenario can also be generalized to atomic mixture.

In ref. [3], we only consider the combinations of Na$|F, m_F\rangle$ + Rb$|F, m_F\rangle$ = $|1, 1\rangle + |1, 1\rangle$ and $|1, -1\rangle + |1, -1\rangle$. Later, we also study FRs in all other combinations in $F = 1$ states.[87]. Here I only discuss the results in ref. [3].

As indicated before, both Na and Rb atoms are in $|1, -1\rangle$ states when they are loaded into XODT. Since Na and Rb have a similar hyperfine structure as well as near Zeeman shifts at low magnetic field, we can transfer both atoms to $|1, 1\rangle$ states at a magnetic field of 10 G with a single rf adiabatic rapid passage(ARP). However, for preparing other spin combinations, we have to use more than one rf ARPs at a magnetic field about 100 G where the transition frequencies between different Zeeman states have separations larger than 1 MHz.

Typically we can prepare a mixture with 1.5×10^5 atoms for both species after spin rotation and evaporation. The temperature is $1.5(1.8)\mu$K for Na(Rb). With measured trap frequencies of $\omega_{\rm Na}\,(\omega_{\rm Rb}) = 2\pi\times\{320, 355, 160\}$ $(\{280, 310, 140\})$Hz, the calculated peak density is $3 \times 10^{12}{\rm cm}^{-3}\,(10^{13}{\rm cm}^{-3})$ for Na(Rb).

With the prepared mixture, we start coarse scan by switching the magnetic field to a certain value and then sweeping the magnetic field in a range of 2 G in 500 ms. If heating and loss are observed in both atoms, we use a holding method to determine accurate position of the FR: (1) ramp magnetic field to a value slightly larger than the possible resonance; (2) wait for magnetic field stabilization by holding it at this value for about 10 ms; (3) switch the magnetic field to a value and hold it there for a period of time, typically 50 ms. The time varies for different resonances to make of the maximum loss

is about 60 %; (4) detect remaining atom numbers and size of atomic clouds after TOF. By varying the holding magnetic fields, we get a loss and heating spectrum as shown in Fig. 6.1. Fitting with Gaussian curves, we can get the resonant magnetic field as well as information of the resonance width.

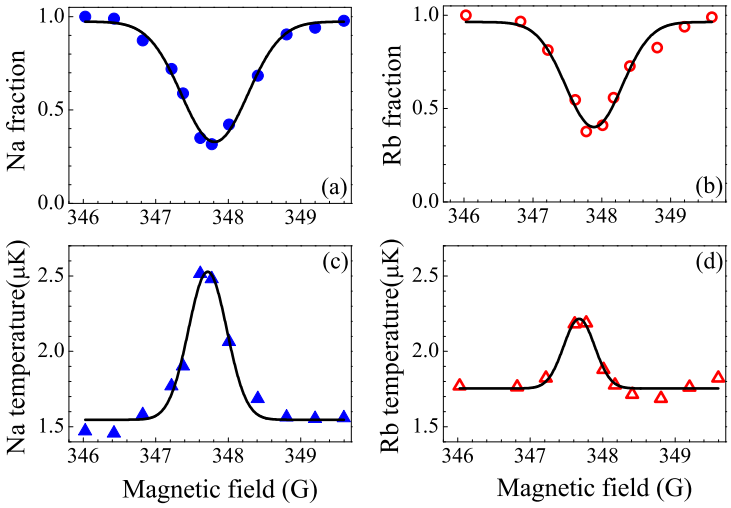

Figure 6.1: Feshbach resonance near 347.8 G. When both atoms are in $|1,1\rangle$ state, loss and heating are observed for Na(left) and Rb(right). Black solid lines are fitting results of Gaussian functions. This figure is taken from [3].

Besides several s-wave FRs, we also observe some p-wave FRs. The multiple structure can be resolved with our magnetic field resolution, as shown in Fig. 6.2.

6.1.2 Analysis and assignment

Prof. Eberhard Tiemann help to analyze these resonances with coupled-channel(cc) model. This method is successfully used in other homo- and hetero-nuclear systems [38, 88, 89, 90]. The potential curves for NaRb $X^1\Sigma^+$ and $a^3\Sigma^+$ are constructed in a power series of the internuclear separation R.

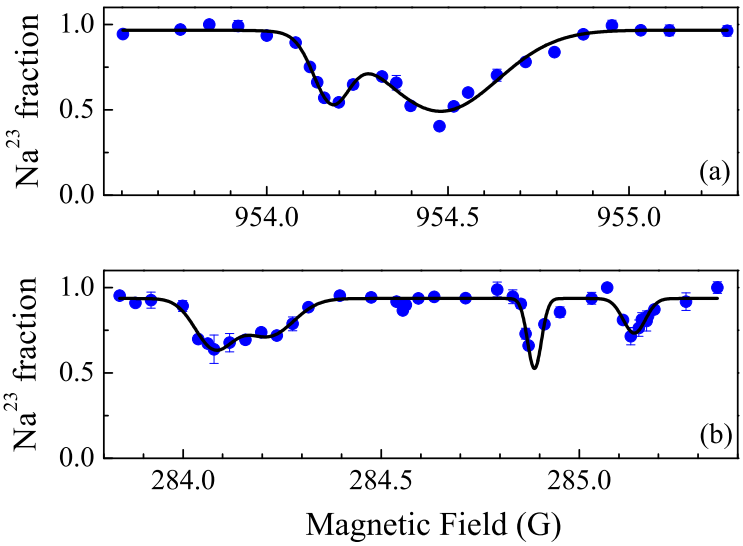

Figure 6.2: p-wave FRs for $|1,-1\rangle + |1,-1\rangle$ spin combination(upper panel) and $|1,1\rangle + |1,1\rangle$ spin combination(lower panel). This figure is taken from [3].

They are firstly parametrized based on previous spectroscopy work [40] and then fitted with found FRs as well as about 10000 rovibrational transitions from the Fourier-transform molecular spectroscopy [40]. Spin-spin interaction [38] as well as Fermi-contact interaction are included in calculations. More information of the calculations can be found in [3].

The cc calculations can explain our measurement with high accuracy and the discrepancy between the calculations and the observations are smaller than 200 mG. The analyses also reveal the scattering lengths of the uncoupled states to be 106.74 a_0 for $X^1\Sigma^+$ and 68.62 a_0 for $a^3\Sigma^+$.

All found FRs are summarized in Table. 6.1. There are two s-wave resonances located at about 347 G and 478 G with a width about 4 G. They can be used to tune the interspecies interactions without affecting the intraspecies s-wave scattering lengths $a_{\mathrm{Na,Rb}}$ since all intraspecies FRs are away from these

two FRs.

6.2 Double species BECs with tunable interaction

In this part, details of the miscible-immiscible transition in the dBECs of Na and Rb will be presented.

6.2.1 Coupled Gross-Pitaevskii(GP) equation

Recalling the GP equation of a single specie BEC and generalizing it to dBECs, we have

$$\begin{cases} \left[-\frac{\hbar^2}{2m_1}\nabla^2 + V_{ext,1} + g_{11}|\phi_1|^2 + g_{12}|\phi_2|^2\right]\phi_1 = \mu_1\phi_1 \\ \left[-\frac{\hbar^2}{2m_2}\nabla^2 + V_{ext,1} + g_{22}|\phi_2|^2 + g_{12}|\phi_1|^2\right]\phi_2 = \mu_2\phi_2 \end{cases} \tag{6.2}$$

$V_{ext,i}, (i = 1, 2)$ are the external trap potentials for atoms 1 and 2. m_i, μ_i are atomic mass and chemical potentials. Interaction strength $g_{ij} = 2\pi\hbar^2 a_{ij}/m_{ij}$, $(i, j = 1, 2)$ depends on the intra-(inter) species s-wave scattering length a_{ij} and reduces mass $m_{ij} = m_i m_j/(m_i + m_j)$. The wave functions ϕ_i are normalized by $N_i = \int d\mathbf{r} n_i = \int d\mathbf{r}|\phi_i|^2$, where N_i are atom numbers. Correspondingly, the total energy of this system is

$$E = \int d\mathbf{r}\left(\frac{\hbar^2}{2m_1}|\nabla\phi_1|^2 + \frac{\hbar^2}{2m_2}|\nabla\phi_2|^2 + V_{ext,1}n_1 + V_{ext,2}n_2 + \frac{1}{2}g_{11}n_1^2 + \frac{1}{2}g_{22}n_2^2 + g_{12}n_1n_2\right) \tag{6.3}$$

Following the analysis of [91], with the assumption of large number which require that $g_{11,22} > 0$ and uniform system, if the two condensates overlap,

Table 6.1: Summary of observed ^{23}Na + ^{87}Rb interspecies FRs with the assignments from coupled-channel calculations. We have investigated resonances below 1000 G for two different spin combinations. The resonance centers B_{exp} and FWHM widths ΔB_{exp} are determined by profile fits to Gaussian functions. The column "obs-cal" gives the difference between observation and calculation assuming a two-body collision. Resonance profiles according to $a = a_{bg}(1 + \Delta/(B - B_{res}))$ are calculated for s-wave at 1 nK. Where the unit of magnetic field is G.

Entrance channel	B_{exp}	ΔB_{exp}	$\delta_{obs-cal}$	type	Closed channel	B_{res}	Δ	$a_{bg}(a_0)$
Na$\|1,1>$	284.1(3)	0.12(4)	-0.05	p M=1 or 2 m_f=2	v=-2(2+1)			
+	284.2(3)	0.14(2)	-0.018	p M=3 m_f=2	v=-2(2+1)			
Rb$\|1,1>$	284.9(3)	0.04(1)	0.115	p M=2 m_f=1	v=-2(2+1)			
m_f=2	285.1(3)	0.06(1)	0.072	p M=1 m_f=1	v=-2(2+1)			
	347.8(3)	0.95(17)	0.012	s M=2 $f = 3$	v=-2(2+1)	347.75	-4.89	66.77
	478.8(3)	0.99(7)	-0.035	s M=2 $f = 2$	v=-2(2+1)	478.79	-3.80	66.77
Na$\|1,-1>$ +	899.8(3)	0.45(5)	0.021	s M=-2 $f = 2$	v=-1(2+1)	899.82	0.333	75.91
Rb$\|1,-1>$	954.2(3)	0.12(1)	-0.060	p M=-2 m_f=-2	v=-1(2+1)			
m_f=-2	954.5(3)	0.33(5)	-0.027	p M=-3 and -1 m_f=-2	v=-1(2+1)			

the total energy is

$$E_o = \frac{1}{2}\left[g_{11}\frac{N_1^2}{V} + g_{22}\frac{N_2^2}{V} + 2g_{12}\frac{N_1 N_2}{V}\right]. \tag{6.4}$$

V is the volume of the trap potential.

If the two condensates are immiscible and occupy different position. Neglecting the thickness of the interface between the two condensates, the total energy of the system is

$$E_s = \frac{1}{2}\left[g_{11}\frac{N_1^2}{V_1} + g_{22}\frac{N_2^2}{V_2}\right] \tag{6.5}$$

Here V_i are the occupied volume of condensate i. The conditions of a fixed system size $V = V_1 + V_2$ and equal pressure $\partial E_s/\partial V_1 = \partial E_s/\partial V_2$ lead to

$$\begin{cases} V_1 = \dfrac{V}{1 + \sqrt{g_{22}/g_{11}}\,(N_2/N_1)} \\ V_2 = \dfrac{V}{1 + \sqrt{g_{11}/g_{22}}\,(N_1/N_2)} \end{cases} \tag{6.6}$$

The energy becomes

$$E_s = \frac{1}{2}\left[g_{11}\frac{N_1^2}{V} + g_{22}\frac{N_2^2}{V} + 2\sqrt{g_{11}g_{22}}\frac{N_1 N_2}{V}\right] \tag{6.7}$$

Therefore, the energy difference between these two states is

$$\Delta = E_o - E_s = \left(g_{12} - \sqrt{g_{11}g_{22}}\right)\frac{N_1 N_2}{V}. \tag{6.8}$$

For small interspecies interactions, $g_{12} < \sqrt{g_{11}g_{22}}$, the energy of the overlap states is lower and the two condensates prefer to occupy the same position. While for large interspecies interactions, $g_{12} < \sqrt{g_{11}g_{22}}$, the two condensates can not overlap, which lead to the immiscible states. The results can also be

found with stability analysis [92].

Define the critical interspecies interaction strength as

$$g_{12}^{c} = |\sqrt{g_{11}g_{22}}| \tag{6.9}$$

For $g_{12} < -g_{12}^{c}$, the two condensates collapse since the interspecies attractive interactions is larger than the intraspecies repulsive interactions. For $g_{12} > g_{12}^{c}$, the mutual repulsive interactions of the two condensates repel each other, making the two condensates immiscible. For other values of g_{12}, the two condensates overlap.

With the known intraspecies scattering lengths of Na (54.5 a_0) [38] and Rb (100.4 a_0) [39, 93, 94], the calculated critical interspecies scattering length is 60.2 a_0 for Na$|F = 1, m_F = 1\rangle$ + Rb$|F = 1, m_F = 1\rangle$ combinations. Since the $a_{12} = 73a_0$ [3] at zero magnetic field, the dBECs should be immiscible. This immiscibility has been experimentally proved in Fig 5.6.

We can tune the interspecies interaction accordint to [95, 96]

$$a_{12} = a_{bg}\left(1 - \frac{\Delta_1}{B - B_{res,1}}\right)\left(1 - \frac{\Delta_2}{B - B_{res,2}}\right). \tag{6.10}$$

By tuning the g_{12} be smaller (larger) than g_{12}^{c} we can realize the miscible (immiscible) states. The critical magnetic field is 384.5 G. For $a_{12} = 0$, the magnetic field is 352.6 G.

6.2.2 Creation of dBECs with tunable interactions

There are two methods of creating the dBECs with different interaction strength. One is preparing dBECs at a favorable magnetic field where a_{12} is suitable for sympathetic cooling and then changing magnetic field to different values. In order to avoid exciting dBECs, the final magnetic field ramp must

be very slow. It is because that when tuning the B across the critical value B_c, the adiabatic theorem requires that $\dot{E}(B)/E_g \ll 1$. Where E_g is the energy difference between the two phases and $\dot{E}(B)$ is the energy change rate when ramping the magnetic field. However the immiscible-miscible transition is a gapless transition and the time required to avoid exciting the system is infinite long. We tried to use this method to create dBECs but dipole oscillations are observed when ramping the magnetic field.

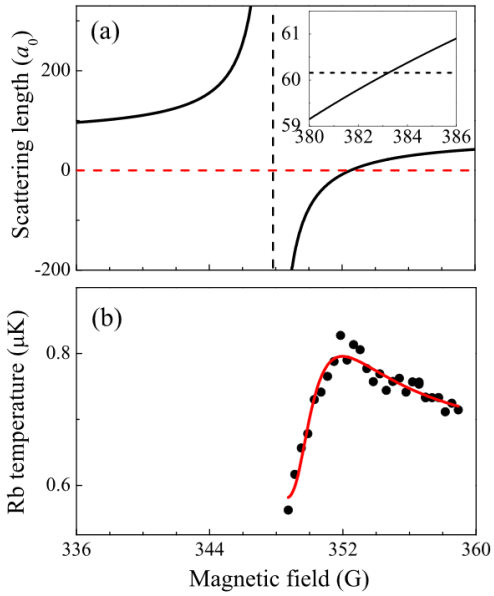

Figure 6.3: (a).Tunability of a_{12} with s-wave FR. The vertical dashed line indicates the resonant magnetic field 347.8 G and the inset shows the interspecies scattering lengths near the miscible-immiscible transition point. (b) Temperature of Rb after fast evaporation of Na in XODT for different magnetic fields.

Another method is firstly ramping the magnetic field to a desired value and then performing the evaporative and sympathetic cooling. There are also two difficulties. The first one it that some a_{12} is not suitable for sympathetic cooling and the dBEC number is small. The second one is that the dBEC formation is also a gapless phase transition and defects will be created if

evaporation is fast [97]. However, the evaporation speed requirement in our system is not as strict as the experiments of Papp *et al* [97] since we have a near spherical trap. In this trap we have the trap frequencies of $2\pi \times (124, 143, 74)$Hz and $2\pi \times (112, 129, 66)$Hz for Na and Rb, respectively. This trap is helpful to avoid the formation of patterns [98].

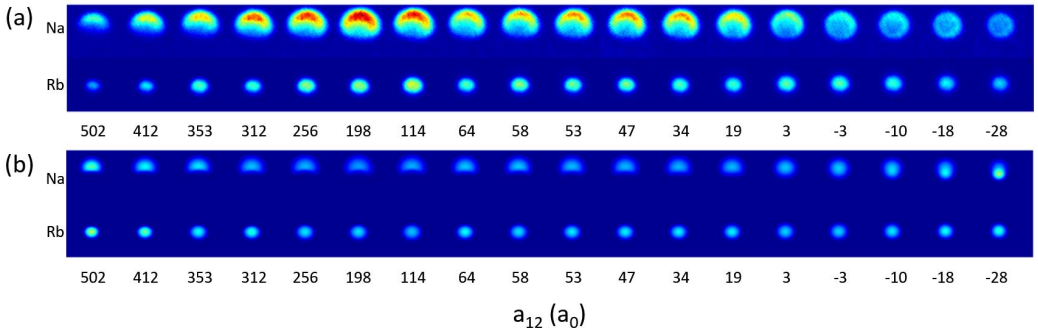

Figure 6.4: (a) Column density profiles of the double BEC near the 347.8 G resonance measured after 13 ms TOF. The interspecies scattering length a_{12} are calculated for different magnetic field values. The atom numbers are different for the a_{12}. (b) Simulated in-trap column density profiles for the dBEC. the simulation parameters for each image are the same as the corresponding experimental ones in (a).

After optimizing experimental parameters, we find that the second method is more favorable for creating larger dBECs. We also study the magnetic field dependent sympathetic cooling by measuring Rb temperature after a fast evaportion of Na in the XODT. The results are shown in Fig. 6.3. Since the thermalization speed depends on the interspecies scattering cross section $\sigma_{12} = 4\pi a_{12}^2$, we can fit the data with a function[99] of

$$T(B) = T_{eq} + \Delta T \exp\left[-\eta a_{12}^2 (B - \delta B)^2\right] \tag{6.11}$$

where the T_{eq}, ΔT, η and δB are fitting parameters. The fitted $a_{12} = 0$ point is 352.0(6) G, which is in agreement with our expectation on this FR.

We image the dBECs at low magnetic field. The magnetic field is hold at the interesting values for the first 2 ms TOF and then switched off for the following expansion. Since the atom density decrease quickly at the first 2 ms, we assume that the following TOF with the background a_{12} will not affect the density distribution too much.

We assume the density distributions after TOF are the same as the in trap ones if the scaling factors related to the trap frequencies are taken into account. Therefore we normalize all dimensions to the size of Rb BEC after TOF to quantitatively analyze the separations of the dBECs.

By changing the magnetic fields, we can create dBECs with different a_{12} ranging from -28 a_0 to 502 a_0. As shown in Fig. 6.4, at large positive scattering lengths, the crescent shaped Na BEC lies above the Rb BEC. As a_{12} decreases, the Na BEC becomes more and more round. When a_{12} is negative, the Na BEC becomes a "doughnut" shape. We need clarify that these results are different from the theoretic calculations. The deviations come from the non-ideal detection method in our experiments. Although we keep the magnetic fields for the first 2 ms TOF, the density is still high enough to contribute significant mutual repulsive interactions to perturb the density distributions of dBECs after turning off the magnetic fields.

It is hard to tell where is the miscible-immiscible transition point when comparing absorption images. However, if we plot the center of mass(COM) separations between Na and Rb BECs, we find that there is a turning point around 60 a_0, which is coincident with the calculation. It should be clarified that the numbers of the created dBECs are small, and consequently the critical scattering length could be different from the calculated results based on the TF approximation. This effect can be studied by creating large dBECs.

We also numerically calculate the in trap densities of Na and Rb BECs

with corresponding experimental parameters. The results are shown in Fig. 6.4 and Fig. 6.5. These two results can qualitatively describe the experimental observations.

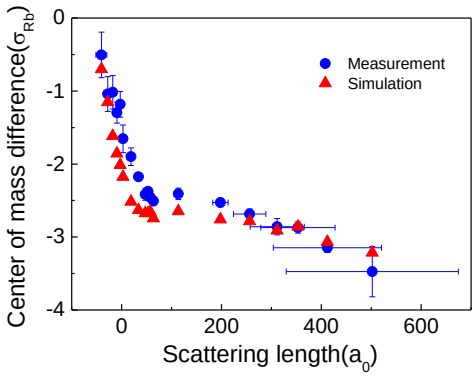

Figure 6.5: Measured and simulated a_{12} dependent vertical COM separation of the Na and Rb BECs. The data are extracted from images in Fig. 6.4. Error bars in the measured separations represent one standard deviation of statistic from typically 5 repeated experimental cycles, while those of a_{12} come from magnetic field calibration and stability.

To summarized this chapter, we have identified three s-wave and several p-wave Feshbach resonances in the heteronuclear mixture of Na and Rb. The s-wave resonance located at 347.8 G is used to control the interspecies interactions. Both the miscible and immiscible states are observed and simulated. Although it is hard to get the critical value of a_{12}, we observe a "kick point" which can be qualitatively explained by the simulations.

□ End of Chapter.

Chapter 7

Formation of NaRb Feshbach molecules

FR results from the coupling between an atomic pair and a molecular state. This coupled two channel picture indicates that the Feshbach molecules(FM) can be created with an adiabatic passage or a Rabi pulse. In this chapter, I will discuss the formation of ultracold FMs of NaRb.

7.1 Magneto-association

The formation of FMs have been extensively studied both theoretically and experimentally [15, 41]. A schematic figure of association FMs by adiabatically sweeping magnetic field across the FR is shown in Fig. 7.1. It is exactly a Laudau-Zener process, where the coupling strength is related to resonance width Δ, background scattering length a_{bg}, differential magnetic moment $\delta\mu$. Assuming a linear sweeping of magnetic field, the molecule formation efficiency for an atomic pair is $P = 1 - \exp(-2\pi\delta_{LZ})$. The Landau-Zener

factor is

$$\delta_{LZ} = \frac{2\pi\hbar}{\mu}\left|\frac{a_{bg}\Delta}{\dot{B}}\right|. \tag{7.1}$$

μ is the reduced mass. When generalizing to multiple particles situation, it is important to count the number of available atomic pairs which is proportion to density overlap $n_1(\mathbf{r})\, n_2(\mathbf{r})$. Then the association efficiency reads [100]

$$P = 1 - \exp\left(-2\pi n_1(\mathbf{r})\, n_2(\mathbf{r})\, \frac{2\pi\hbar}{\mu}\left|\frac{a_{bg}\Delta}{\dot{B}}\right|\right) \tag{7.2}$$

For a small ramp speed of B, the association efficiency is

$$P = 2\pi n_1(\mathbf{r})\, n_2(\mathbf{r})\, \frac{2\pi\hbar}{\mu}\left|\frac{a_{bg}\Delta}{\dot{B}}\right|. \tag{7.3}$$

The linear dependent of $1/\dot{B}$ is confirmed experimentally [101, 102] and the linear dependent of density overlap has also been tested [102].

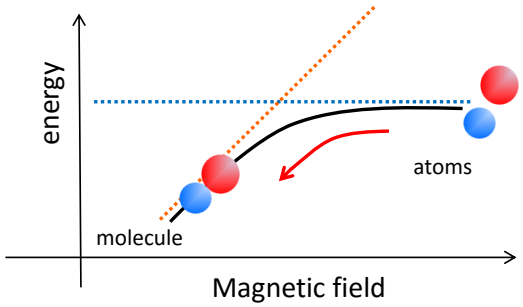

Figure 7.1: Schematic of magneto-association. The two dashed lines are uncoupled atomic pair and the molecular state. The solid line is one of the dressed states. The molecules can be created by ramping the magnetic field across the resonance.

However, the molecule association efficiency cannot reach the unity but saturates to a samller value. E. Hodby *et al.* [101] invented a stochastic phase-space sampling (SPSS) model to explain this saturation. This phenomenological model claims that a pair of atoms close in phase space can

form a FM if they satisfy the relation

$$\mu \left| v_{rel} \right| \left| p_{rel} \right| < \gamma \frac{h}{2} \tag{7.4}$$

where v_{rel} and p_{rel} are the relative velocity and momentum of the two atoms. γ is a system dependent constant number. Previous experiments find that $\gamma_{BF} = 0.38(3)$ for a Boson-Fermion mixture [102], $\gamma_B = 0.44(3)$ for a bosonic gas [101] and $\gamma_F = 0.38(4)$ for a fermionic gas [101].

The association becomes more complicated when loss mechanisms are taken into account. For a higher association efficiency, it is better to use a slower magnetic field ramp, larger density overlap as well as higher phase space density overlap. However, when the magnetic field is close to the FR, the three-body loss and dimer relaxation are largely enhanced. Therefore all these requirements for a higher association efficiency lead to severe loss during the association, especially in Bose gases where there is no Pauli blocking to prevent two particles getting close to each other. Another point is that in order to get a mixture with higher phase space density, one suffers from small atom numbers. Consequently, the best experimental parameters for the biggest molecular sample can only be found by trial and error.

In our experiments, the mixtures consist of 8×10^4 Na and 1×10^5 Rb. The temperature is about 350 nK. The average trap frequency is $\bar{\omega} = 2\pi \times 170(148)$ Hz for Na(Rb). The calculated peak density and phase space density are 4×10^{12} cm^{-3}(2.6×10^{13} cm^{-3}) and 1.0(0.84) for Na(Rb), respectively. The association is performed by sweeping the magnetic field across the resonant field with a speed of 5.2 G/cm. In Fig. 7.2, we show the remaining atom number for different magnetic fields in association and reverse sweeping process. The onset of loss and gain of remaining atoms indicate the resonant magnetic field value as well as the creation of FMs.

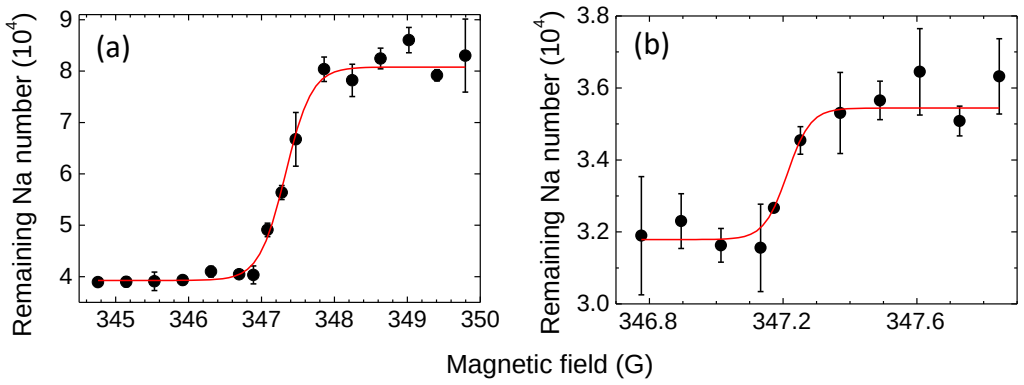

Figure 7.2: Magneto-association and dissociation. (a) Remaining atoms after magnetic field is swept down with a constant speed and stopped at different field. (b) Reverse sweeping after association. The solid curves are fitting results to hyperbolic tangent function. Error bars are from statistics of typically three shots.

After creation of FMs, it is necessary to remove the unassociated atoms as fast as possible since atom-molecule collisions limit FMs lifetime severely. The most powerful method is using a blast laser. By applying a laser resonant with a cycling transition, atoms can continuously scatter photons. The corresponding radiative force pushes the atoms out of the trap. At the magnetic field of 347 G, the cycling transition is $|m_J = 1/2, m_I = 3/2\rangle \longleftrightarrow |m_J^{'} = 3/2, m_I^{'} = 3/2\rangle$ for both Na and Rb atoms. (Since F is not good quantum number at high magnetic fields, quantum number of m_J and m_I will be used in this paragraph. $|m_J = 1/2, m_I = 3/2\rangle$ is adiabatically connected with $|F = 2, m_F = 2\rangle$, $|m_J' = 3/2, m_I' = 3/2\rangle$ is adiabatically connected with $|F' = 3, m_F' = 3\rangle$, and $|m_J = -1/2, m_I = 3/2\rangle$ is adiabatically connected with $|F = 1, m_F = 1\rangle$.) Thus a MW pulse has to be applied to populate the Na and Rb atoms into the $|m_J = 1/2, m_I = 3/2\rangle$ states before applying the laser pulse. Since this MW transition is very sensitive about the magnetic field ($\sim$ 2.2 MHz/G), stable MW pulse requires the Rabi Frequency about 50 kHz with our magnetic field stability. It is technically difficult to achieve

such large Rabi Frequency in our apparatus I. However the MW system of our apparatus II works thanks to the smaller size of the science cell. But at the time of the publication of [6], we use a gradient magnetic field to remove the Na and Rb thanks to the non-zero differential magnetic dipole moments between the free atoms and the FMs. Below a magnetic field of 345.6 G the FMs have negative magnetic dipole moments and they are trapped by the gradient field. However, $|m_J = -1/2, m_I = 3/2\rangle(F = 1, m_F = 1\rangle)$ atoms of Na and Rb have positive magnetic dipole moments which are untrappable. Thus we can use a 3 ms gradient pulse to purify the FM sample.

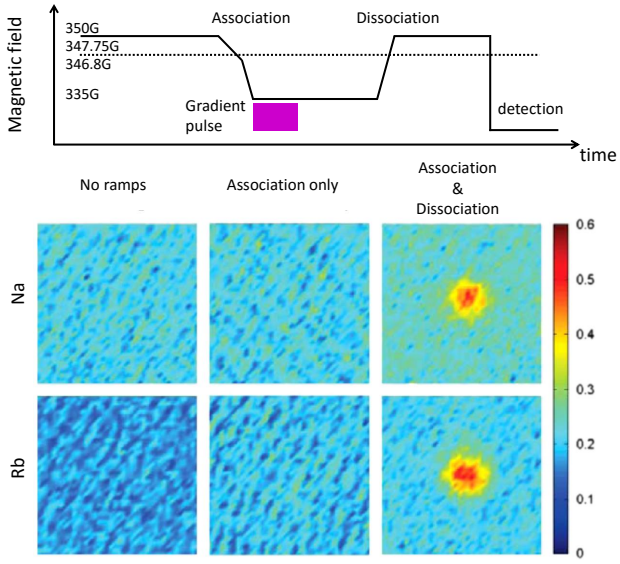

Figure 7.3: Creating pure NaRb FM molecules. (a) shows the schematic of experiments, (b) are absorption image for different experiment sequences. When there is no association or dissociation, no signal could be detected if the gradient pulse is present. After performing all the steps including association, purifying and dissociation, atoms can be detected for Na and Rb. The color bar indicates optical density.

The schematic of creating a pure FM sample is shown in Fig. 7.3. After magneto-association by ramping the magnetic field downward to 346.8 G, we switch it to $B_{final} = 335$ G in 0.1 ms. Then we add a gradient pulse to remove

the free atoms. In the apparatus I, we can only generate this gradient pulse with our QT coil which is connected with our Helmholtz coil to the same power supply in a parallel configuration as described in previous chapter. Thus there is a magnetic field "spike" in the homogeneous magnetic field when suddenly turning on/off current in the QT coil. So we have to ramp B_{final} to a value much smaller than the resonant field to avoid dissociating the FMs by non-ideal control of the magnetic field. The 335 G is an experimental optimized value for the largest FM number. After the gradient pulse, we reversely ramp the magnetic field to 350 G to dissociate the FMs. Then we can measure the properties of FMs by detecting the dissociated free atoms. As shown in the lower panel of Fig. 7.3, only when both association and dissociation are performed we can detect the atoms if the gradient pulse is always present. It is a strong evidence that we have created a pure NaRb FM sample. By optimizing the experimental parameters we can create about 2000 NaRb FMs. (In the apparatus II, we can create more than 10^4 FM now.)

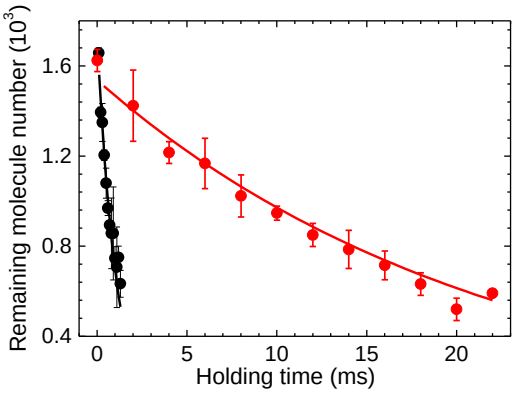

Figure 7.4: Lifetime of molecule sample with(black solid circles) or without(red open circles) free atoms. Solid curves are exponential fitting results. Error bars represent on standard deviation from typically three shots.

The overall association efficiency is about 2.5 %, which is much smaller than that of the Bose-Fermi mixture experiments: 40% for KRb [102], 15%

for NaK [103]. However, this result is comparable with the experiments of the bosonic RbCs Feshbach molecules, in which the reported association efficiences are 7 % [104] and 2.5 % [105]. In a system with Fermions, Pauli blocking prevents particles getting close, resulting a suppressed atom-molecule collision rate. That is why the Bose-Fermi Feshbach molecules have higher association efficiencies. This is consistent with the FM lifetime measurements in Fig. 7.4: 1.1(1) ms if free atoms are present while 21.8(8) ms if free atoms are removed. The 21.8 ms lifetime is long enough for further experiments.

7.2 Binding energy measurement

To further characterize the FM, we measure its binding energies at different magnetic fields. By applying a rf field, a pair of atoms can be associated into a FM if the rf frequency matches the binding energy of the FM. Due to the conservation of M_F, which is the projection of the total angular momentum on the direction of the magnetic field, the polarization of the rf field should be in parallel with the magnetic field. After the formation, the FMs will be quickly killed by colliding with free atoms. Consequently, by measuring the leftover atoms after a rf pulse, we can extract information of the binding energy. Here we measure a spectrum with a constant rf frequency but a varying magnetic field. A typical spectrum is shown in Fig. 7.5.

The shape of the rf spectrum depends on the two-body association rate which is determined by the energy-dependent wave-function overlap of the scattering atomic pair and the molecular state [106]. Close to the resonant magnetic field of a width FR, there is an analytical formula for the loss spectrum which considers the density of states of the atomic pair, temperature broadening as well as the wave-function overlap [106, 107]. However, the used FR in our experiment is not a width FR and we measure the binding

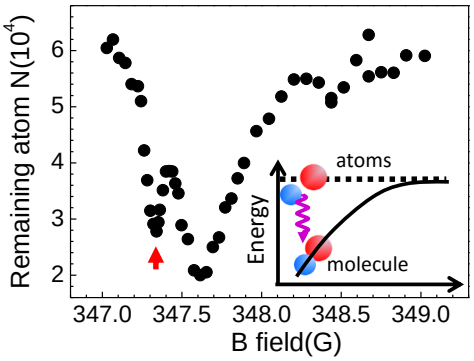

Figure 7.5: Binding energy spectrum by changing magnetic field. In addition to the enhanced loss near FR resonant field about 347.7 G, we observe another loss maximum(marked by an arrow) which corresponds to association of FMs. Here we use a 10 ms, 0.1 MHz, 0 dBm rf pulse. Inset shows the experimental scheme that an atomic pair can be associated into molecules with appropriate rf frequency.

Table 7.1: Summary of fitting results of the two s-wave resonance. Coupled channel calculation results are taken from [3].

Coupled channel		Square well		
B_0	Δ	B_0	Δ	$\delta\mu$
347.75	4.89	347.64(3)	5.20(27)	2.66(29)
478.79	3.80	478.83(3)	4.81(27)	2.52(26)

energies up to 3.5 MHz, where the corresponding magnetic field is about 3 G ($\sim 0.6\Delta$) away from the resonant point. Therefore the analytical formula is not valid in our case. We use a phenomenological function-a convolution of Boltzmann distribution and a Gaussian function-to fit the data [108]. The asymmetric behavior of the measured rf spectrum is captured by the thermal Boltzmann distribution. We use the Gaussian function instead of a Lorentz function since there are power broadening and magnetic fluctuation. We also add a linear function to account for the "background" three-body loss feature when the rf field is absent. One example of fitting is shown in Fig. 7.6.

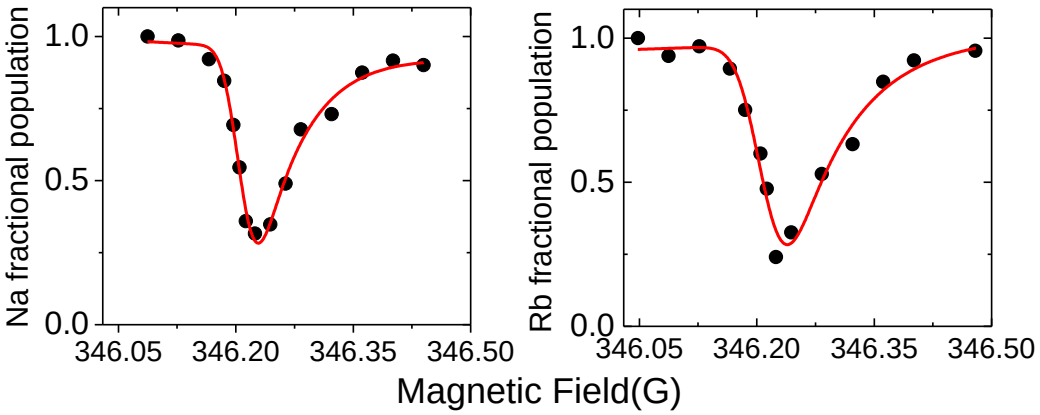

Figure 7.6: Remaining Na(a) and Rb(b) atoms after a 1 MHz pulse. The solid curves show the fitting results.

In our experiments, the pulse length is chosen to get a large but not saturated loss feature. As a result, the pulse length ranges from 10 ms to 300 ms. We also use different rf power but no power induced shift is observed within our experimental parameters. With this method, we measure the binding energies of the two $|1,1> + |1,1>$ s-wave FRs and summarize the results in Fig. 7.7. The information of these two FRs can be extracted form these measurements by fitting with a two-channel square well model developed by Lange *et al.* [96]. Near a FR, the binding energy $E_b = \hbar^2 k_m^2 / 2\mu$ depends on the differential magnetic dipole moment $\delta\mu$ between the open and the closed channel and the Feshbach coupling strength Γ according to

$$k_m(B) = \frac{1}{a_{bg} - \bar{a}} + \frac{\Gamma/2}{\bar{a}\left(E_b + \delta\mu\left(B - B_c\right)\right)} \tag{7.5}$$

Here k_m is the wave number, B_c is the magnetic field where the bare molecular state is tuned to degenerate with the open channel and $\bar{a}$ is the mean scattering length which depends on the van der Waals C_6 coefficient. The

resonance width Δ and resonant magnetic field B_0 can be calculated by

$$\begin{cases} \Delta = \dfrac{1}{\delta\mu}\dfrac{(a_{bg}-\bar{a})^2}{a_{bg}\bar{a}}\dfrac{\Gamma}{2} \\ B_0 = B_c - \dfrac{a_{bg}}{a_{bg}-\bar{a}}\Delta \end{cases} \tag{7.6}$$

With $C_6 = 1.2946 \times 10^7$ cm^{-16} and $a_{bg} = 66.77a_0$ [3], we can get information of these two FRs as Table. 7.1

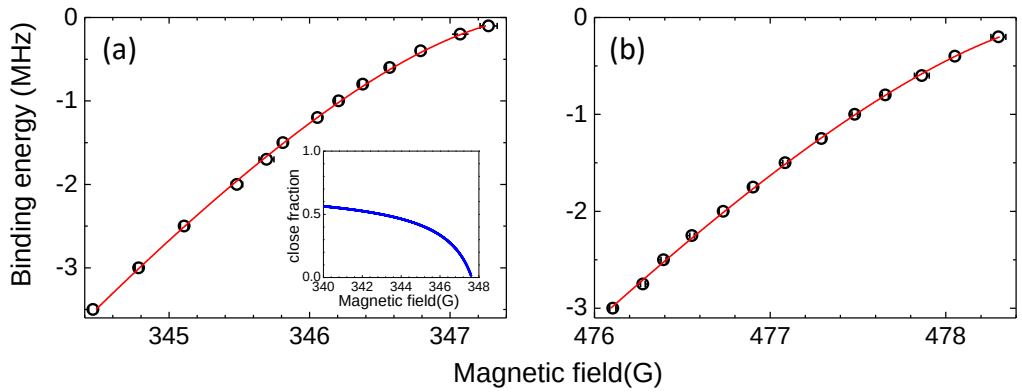

Figure 7.7: Summary of the binding energy measurements of two FRs. Open circles are experimental data. Error bars comes from fitting and magnetic field calibration. Solid lines are fitting results of the two-channel square well model. Inset of (a): calculated close channel fraction from fitted parameters.

With the fitted results, the widely used dimensionless parameter $s_{res} = \frac{a_{bg}}{\bar{a}}\frac{\delta\mu\Delta}{\bar{E}}$ for these two resonances are calculated to be 0.72 and 0.63. Which indicate that they are not wide resonance but with an intermediate coupling strength. It explains that the binding energies of these two FRs change quickly as the magnetic field is tuned away from the resonant position. We can also calculate the close channel fraction with $Z = \frac{\partial E_b}{\partial E_c} \approx \frac{1}{\delta\mu}\frac{\partial E_b}{\partial B}$ [15] and the results for the 347.8 G resonance are shown as the inset of Fig. 7.7(a).

In summary, the Feshbach molecules of NaRb are created by magneto-association. We also measure the binding energies of the 347.8 G and 478.8

G s-wave Feshbach resonances. By fitting with the two-channel square well model, the parameters of the two Feshbach resonances are revealed. The s_{res} are about 1 for both the resonances which indicate that they have intermediate coupling strength.

□ End of Chapter.

Chapter 8

Investigating few-body physics with Na and Rb mixtures

Few-body physics play an important role in quantum mechanics. In this chapter, I report the observation of atom-dimer and dimer-dimer recombination resonances in an ultracold Bose-Bose system of Na-Rb. During writing this thesis, the experiments have not been finished and theoretical analyzing is still going on. Therefore, I will only present some preliminary results here. You can find more details of this work in future publications of our group.

8.1 Three-body system

One milestone in few-body physics is the emergence of Efimov trimers. In 1970s, V. Efimov found that the properties of three quantum particles follow a universal behavior if the pairwise interaction are resonantly enhanced [50]. According to the predictions, there are an infinite number of three-body bound states. What is more astonishing is that the binding energies of these states obey a logarithmic periodic rule [51].

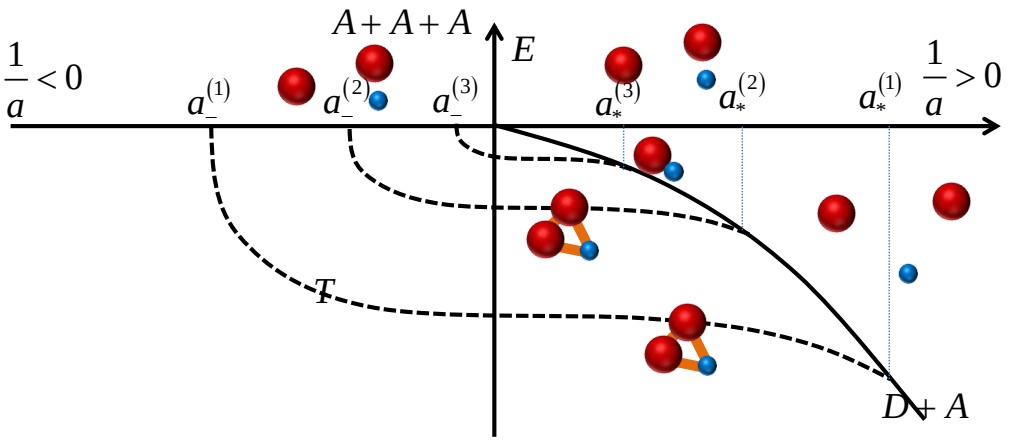

Figure 8.1: Efimov scenario. Above the scattering continuum E = 0, atomic mixture exit. And at positive scattering length side, there is a universal dimer state and the system is atom-dimer mixture. In the region $1/|a| \to 0$, both positive and negative scattering length side, a series of three-body bound states show up. Those trimer states attach the atomic threshold line at $a_-^{(n)}$ and the atom-dimer threshold line at $a_*^{(n)}$.

The Efimov scenario is schematically depicted in Fig. 8.1. Dimer states do not exit if $a < 0$. However, if a third particle is added into the system, a bound state can be formed. At $a < 0$ side, the trimer states intersect the scattering continuum at $a_-^{(n)}$. For $a > 0$, a dimer state exist and the trimer states smoothly merge the atom-dimer threshold at $a_*^{(n)}$. These interesting scattering lengths have a scaling law as

$$\frac{a_-^{(n+1)}}{a_-^{(n)}} = e^{\pi/s_0}, \frac{a_*^{(n+1)}}{a_*^{(n)}} = e^{\pi/s_0}. \tag{8.1}$$

The parameter s_0 depends on details of the system and equals 1.0062378 for a system of three identical bosons [4]. The Efimov trimers connect $a < 0$ side and $a > 0$ side. The intersections of these trimers and $a = \infty$ axis define

binding energies E_n, which also have a geometrical scaling law

$$\frac{E_{n+1}}{E_n} = e^{-2\pi/s_0} \tag{8.2}$$

^{4}He is the first promising candidate for studying the Efimov physics. Due to the fine-tuning of nature, two ^{4}He atoms have a scattering length about 170 a_0 while the the effective range of the van der Waals interaction is only about 9 a_0. Consequently, it is possible to observe the ground and first excited Efimov state. However, it is only recently the the excited Efimov state is observed experimentally [109], 20 years after the observation of the ground trimer state in 1994 [110].

Other candidates are the halo nuclei which consist of a compact core and two loosely bound neutrons. The existence of Efimov states have been analyzed in many isotopes [111]. Although no definitive signals of the Efimov states have been observed in the nuclear systems, the prospect of observing them drives experimental and theoretical researches [112].

Thanks to the successful cooling of netural atoms to nano-Kelvin regime and experimental proof of the tunability of scattering lengths with FRs, cold atoms become the most active area for studying the Efimov physics. In 2006, the first experimental observation of Efimov states was reported in Cs gas [18]. Since then, extensive studies are performed in other cold atom systems: homonuclear bosonic system such as ^{7}Li [113, 114, 115, 116], ^{39}K [117, 118], ^{85}Rb [119], Cs [120, 121], homonuclear ferminoic spin mixture [122, 123, 124, 125, 126, 127], heteronuclear mixtures [128, 129, 130, 131, 132, 133, 134] and atom-dimer mixture [129, 135]. All these works help to understand the Efimov physics within different experimental parameters.

Theoretical works help to examine and understand the experimental observations and give predictions about the few-body physics [4, 136, 137, 138].

8.1.1 Hyperspherical coordinate and hyperspherical potential

In order to understand the origins of Efimov trimers, it is helpful to use the hyperspherical coordinates [139]. In the center of mass frame, the wave function of three particle system can be described by 6 independent coordinates: five hyperangular variables denoted by Ω collectively and the hyperradius R which is the root-mean-square size of the three particles

$$R^2 = \frac{1}{3}\left(r_{12}^2 + r_{23}^2 + r_{31}^2\right) \tag{8.3}$$

where r_{ij} is separation of particle i and j.

With the adiabatic hyperspherical approximation that Ω can fast adjust their values for different R and the assumption that at low temperature the three-body interaction is close to the summation of three two-body interactions, the three-body problem can be solved for different R. Similarly with the Born-Oppenheimer(BO) potential, a set of R-dependent potential curves, the hyperspherical potentials, can be used to describe the three-body scattering [4].

For three identical bosons, if a is much larger than the characteristic size r_0 of the two-body interaction, the hyperspherical potential $V_n(R)$ can be calculated numerically [4]. The lowest several potentials are shown in Fig. 8.2. The lowest potentials at $a > 0$ and $a < 0$ are attractive and can support three-body bound states. The attractive hyperspherical potential for $a > 0$ approaches the "atom + dimer" curve which has a binding energy of $E_D = -\hbar^2/2\mu a^2$ at $R/a \to \infty$. All other hyperspherical potentials converge to the scattering continuum of free atoms.

However, these results only valid in the range $r_0 \ll R \ll a$. In the short

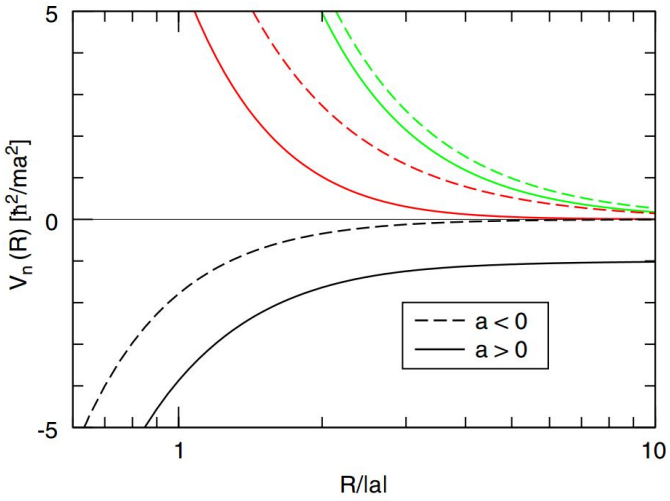

Figure 8.2: Hyperspherical potentials for the lowest three channels for three identical bosons. For both $a > 0$ and $a < 0$, there is only one attractive potential. All potentials except for the lowest potential of $a > 0$ goes to zero at the limit of $R/a \to \infty$, which corresponds to the scattering continuum of three free atoms. The attractive potential for $a > 0$ converges to the atom-dimer limit which has an energy of the dimer binding energy. This figure is taken from [4].

range $R \leq r_0$, the potential is gradually dominated by the van der Waals interaction $U_{vdW}(R) \approx U_{12,vdW}(R) + U_{23,vdW}(R) + U_{31,vdW}(R)$. Near $R \sim a$, the coupling between different channels can not be neglected. Consequently, there is a potential barrier in the lowest channel of $a < 0$ near $R \sim a$. For $a < 0$, in the range $r_0 \ll R \ll a$, there is an analytical formula for the hyperspherical potentials

$$U_v = \frac{s_v^2 - 1/4}{2\mu_{123}R^2} \tag{8.4}$$

where $\mu_{123} = \sqrt{\frac{m_1 m_2 m_3}{m_1+m_2 m_3}}$ is the three-body reduced mass, s_v are parameters depends on details of system. v denotes different channels and $v = 0$ corresponds to the lowest channel:

$$U_0 = -\frac{s_0^2 + 1/4}{2\mu_{123}R^2} \tag{8.5}$$

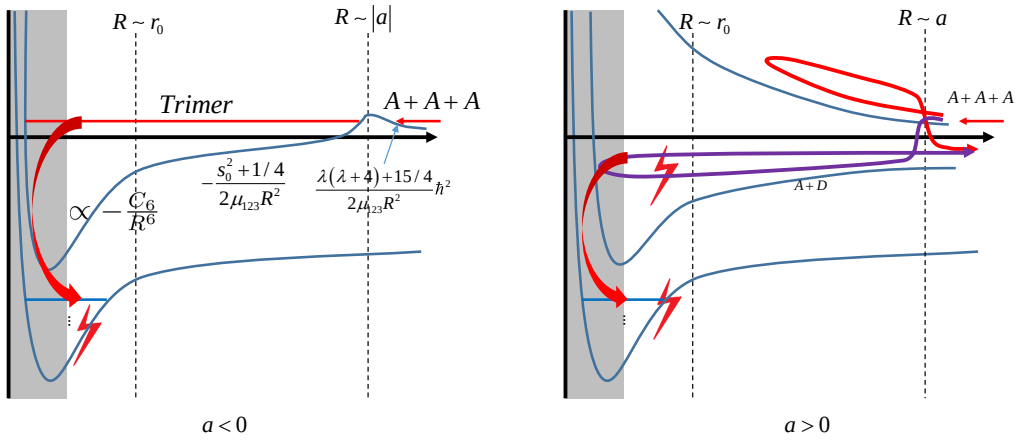

Figure 8.3: Schematic pictures for three-body recombination with the adiabatic hyperspherical potentials model. For $a < 0$, there is a potential barrier resulting from coupling of different hyperspherical potentials near $R \sim |a|$. The height of this barrier depends on a. For certain a, the scattering state is strongly coupled to a three-body bound state thanks to the shape resonance. Since the three-body bound state is coupled to deeply bounded molecular states, loss will be enhanced for this scattering length. For $a > 0$, there are two paths for three colliding atoms, which are denoted as red and purple arrows. These to paths can interfere at $R \sim a$. The destructively interference is responsible for the minima of three-body loss rate. For $a < 0$, the atoms can only recombine to deep dimers. However, for $a > 0$, the atoms can also recombine to the shallow dimer. This figure is a redrawn version and the original one can be find in [5].

This channel is attractive and has three-body bound states, which are the Efimov trimers.

8.1.2 Three-body recombination rate

These hyperspherical potentials dramatically change the scattering processes of three-body system. Beside the a^4 scaling law [86], there are fine structures for three-body loss rates when the three-body bound states are taken into account. The physics behind can be understood with Fig. 8.3. For $a < 0$ and $r_0 \ll R \ll |a|$, the $-1/R^2$ hyperspherical potential is attractive and

dominates the scattering processes. However, due the coupling between different hyperspherical potentials, there is a barrier near $R \sim |a|$. This barrier induces the shape resonance and the height of which depends on a. Thus, by tuning a to certain value, the scattering state is strongly coupled to weakly bounded three-body states, which then quickly decay due to large wave function overlaps with deeply bounded dimer states. The released binding energy makes all the three atoms run away from the trap. As a result, there is a series of loss resonances, the located of which are denoted as $a_-^{(n)}$. For $a > 0$, there are two paths for the scattering as indicated in Fig. 8.3. The destructively interference between these two paths mitigate three-body loss. The loss minima are located at $a_+^{(n)}$.

For $a < 0$, there is no shallow dimer and the three particles can only recombine into deeply bounded dimers. However, recombination into the shallow dimer also contribute to the loss reate [136]. Consequently, the rate constant for recombination α reads

$$\alpha = \frac{\hbar a^4}{m} \begin{cases} 67.12 e^{-2\eta_+} \left[\sin^2\left(s_0 \ln\left(a/a_+\right)\right) + \sinh^2\eta_+\right] \\ \qquad +16.84\left(1 - e^{-4\eta_+}\right), (a > 0) \\ \dfrac{4590 \sinh\left(2\eta_-\right)}{\sin^2\left[s_0 \ln\left(a/a_-\right)\right] + \sinh^2\eta_-}, (a < 0) \end{cases} \tag{8.6}$$

The $\eta_\pm$ describe decay probability to deeply bounded molecules, which generate the width of the Efimov resonances. In an "atom + dimer" system, by colliding with an atom, the weakly bounded dimer can decay to a deeply bounded dimers. The released binding energy is transferred to kinetic energies of recoiled atom and dimer. This dimer relaxation rate is [136]

$$\beta = \frac{20.3 \sinh\left(2\eta_+\right)}{\sin^2\left[s_0 \ln\left(a/a_*\right)\right] + \sinh^2\eta_+} \frac{\hbar a}{m} \tag{8.7}$$

Considering a heteronuclear system with one boson of mass m_1 and two identical bosons of mass m_2. If the interspecies s-wave scattering length $a \gg r_0$ and intraspecies s-wave scattering lengths are zero, the three-body recombination rate is [140]

$$\alpha = C(\delta) D \frac{\hbar a^4}{m_1} \begin{cases} \frac{\sin^2[s_0 \ln(a/a_*)] + \sinh^2\eta_+}{\sinh^2(\pi s_0 + \eta_+) + \cos^2[s_0 \ln(a/a_*)]} + \\ \frac{\coth(\pi s_0)\cosh\eta_+ \sinh\eta_+}{\sinh^2(\pi s_0 + \eta_+) + \cos^2[s_0 \ln(a/a_+)]}, & (a > 0) \\ \frac{1}{2} \frac{\coth(\pi s_0)\sinh(2\eta_-)}{\sin^2[s_0 \ln(a/a_-)] + \sinh^2\eta_-}, & (a < 0) \end{cases} \tag{8.8}$$

At zero temperature, the dimer relaxation rate is

$$\beta = 2\pi C_2(\delta) \frac{\delta(\delta+2)}{\delta+1} \frac{\sinh(2\eta_+)}{\sin^2[s_0 \ln(a/a_*)] + \sinh^2\eta_+} \frac{\hbar a}{m_1} \tag{8.9}$$

Here $D = 128\pi^2\left(4\pi - 3\sqrt{3}\right)$, $\delta = m_1/m_2$ is the mass ratio, and $C(\delta)$ is a constant depends on δ. The scaling factor $\exp(\pi/s_0)$ relates to a equation of s_0:

$$s_0 \cosh(\pi s_0/2) - \frac{2\sinh(\phi s_0)}{\sin(2\phi)} = 0 \tag{8.10}$$

with the parameter ϕ

$$\phi = \arcsin\left(\frac{1}{1+\delta}\right) \tag{8.11}$$

Theoretically, it is possible to observe many Efimov resonances near a Feshbach resonances. However, the finite stability of the magnetic field prevents tuning a to a very large value. Another theoretical restriction is that at the unitary limit, a is not a good characteristic length scale and the recombination rate depends the thermal de broglie wavelength instead of a. For a finite temperature T, the three-body recombination rate in a homonuclear

system saturates to [141, 142]

$$\alpha_{max} = \frac{36\sqrt{3}\pi^2\hbar^5}{(k_B T)^2 m^3}\left(1 - e^{-4\eta}\right) \tag{8.12}$$

Therefore, the temperature of system need to be prepared low enough for observing more Efimov resonances.

For identical bosons, the scaling factor $e^{\pi/s_0} = 22.7$. Which makes it is hard to observe the first excited Efimov resonance. (Only recently, the second Efimov resonance has been observed in Cs gas [121] by creating a sample with a temperature lower than 10 nK.) However, for heteronuclear system with large mass ratio, the scaling factor is much smaller which makes it is preferable to study the Efimov physics. For ^{6}Li-^{133}Cs, the scaling factor is about 5 and two excited Efimov resonances are observed [130, 133].

8.1.3 Van der Waals universality

The previous results are valid in condition that $a \gg r_0$ where the effect of finite r_0 is neglected. However this is not true for real system. Due to the complexity of short range details and differences between atomic species, it used to be believed that there was no universality for the three-body parameters(3BP). (There are different definitions of 3BP. In this thesis, 3BP is defined as the location of first Efimov resonance at $a < 0$ side: $a_-^{(1)}$.) However, people find that all the homonuclear 3BP happen to be about $-9.1 r_{vdW}$ except the ^{39}K experiments where $a_-^{(1)} = -23.3 r_{vdW}$ [143]. This disagreement between predictions and experimental results attract many studies and trigger the theory of van der Waals universality [144].

For the case of three identical bosons, this universality results from a potential barrier located at about $R \sim 2r_{vdW}$ [145, 146]. This barrier reflects

scattering wave function and helps to protect the three-body physics from the short range details of the interaction.

For the heteronuclear mixture of two identical bosons H, with a mass of m_H, and a third distinguishable atom L, with a mass of m_L, there are two situations depends on the mass ratio. If $m_H/m_L > 1$, it is easier to observe more Efimov resonances thanks to the smaller scaling factor e^{π/s_0}. In this "Efimov-favored" system, the universality can be understand with a Born-Oppenheimer approximation where the motion of light atom and heavy atoms can be separated. The corresponding potential for two heavy atoms reads

$$U_{BO}(r) = V_{HH}(r) + V_{BO}(r) \tag{8.13}$$

where $V_{HH}(r)$ is the bare two H atom interaction which is nothing but a van der Waals interaction $-1/r^6$. $V_{BO}(r)$ is interaction induced by atom L. For $r < a$, $V_{BO}(r) \propto -1/r^2$ [4]. In the range $r < r_{HL,vdW}$, $U_{BO}(r)$ is dominated by $V_{HH}(r)$ and the short range details are absorbed by a_{HH}. Consequently, the 3BP only depends on a_{HH}, r_{vdW} and m_H/m_L [147]. For a "Efimov-unfavored" system where the $m_H/m_L < 1$, there is also a universal repulsive barrier similar with identical the bosons case. [147]

8.2 Four-body system

After the prediction of the infinite three-body bound states, it is natural to ask whether there is similar universality for N-body system(N $\geq$ 4).

Although there is no Efimov effect for $N(N > 3)$ particles when the binding energy of $(N-1)$ body bound state is tuned to zero [148]. There are two kinds of other 4-body bound states as shown in Fig. 8.4. Near $a_*^{(n)}$, the atom-dimer scattering length a_{ad} diverges. Therefore the "atom-atom-

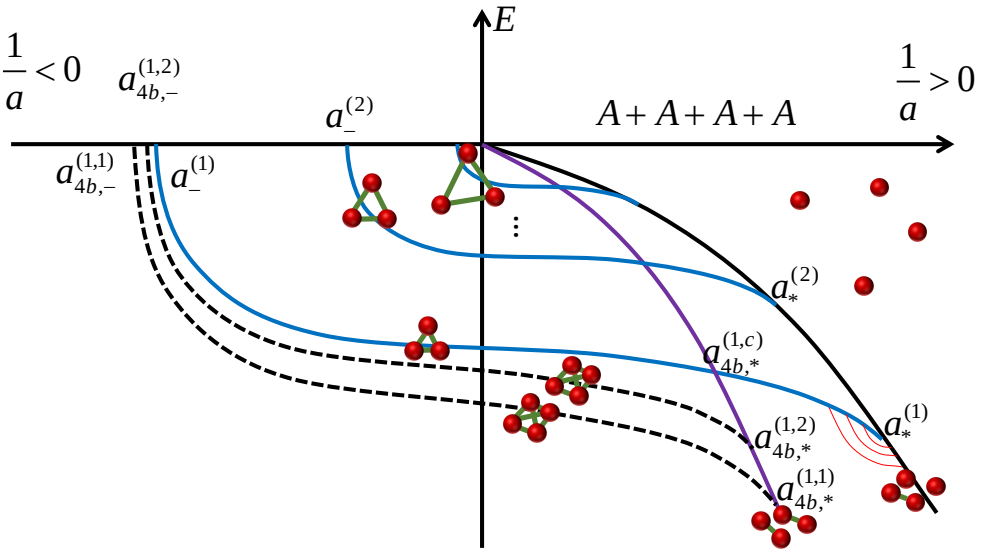

Figure 8.4: Schematic picture of the four-body physics of an identical boson system. For $a > 0$, there are two lines corresponding to the "dimer-atom-atom" curve (black solid line) and the "dimer-dimer" curve (purple solid line), respectively. For every trimer state (blue line), there are two tetramers (dashed lines). There are several intersectant scattering lengths: $a_{4b,*}^{(1,c)}$ for trimer state and the "dimer-dimer" curve; $a_*^{(1)}$ for trimer state and dimer state; $a_{4b,*}^{(1,1)}$ and $a_{4b,*}^{(1,2)}$ for tetramers and the "dimer-dimer" curve. Near $a_*^{(n)}$, scattering length between dimer and atom diverges and there are a series of bound states similar with unequal mass three-body scenario. For $a < 0$, the two tetramers connect with the free atom threshold at $a_{4b,-}^{(1,1)}$ and $a_{4b,-}^{(1,2)}$.

dimer" system is similar with an unequal mass three-body problem and there are an infinite bound states. People also predict that there are two universal tetramers associated with every Efimov trimer [149]. The ratios between several interesting scattering lengths are

$$a_{4b,-}^{(n,1)} = 0.43 a_-^{(n)}, a_{4b,-}^{(n,2)} = 0.90 a_-^{(n)} \tag{8.14}$$

for $a < 0$ [150] and

$$a_{4b,*}^{(n,1)} = 2.37 a_*^{(n)}, a_{4b,*}^{(n,2)} = 6.6 a_*^{(n)}, a_{4b,*}^{(n,c)} = 6.73 a_*^{(n)} \tag{8.15}$$

for $a > 0$ [151].

Similar with three-body scenario, collisional behaviors strongly depend on these four-body states. Experimental observations of four-body resonances are reported in homonuclear systems [18, 150, 113, 152].

Extending the four-body scenario to heteronulcear system, the picture is more complicated. Considering a mixture composed of bosons H and bosons L, there are two kinds of trimers, "HHL" and "HLL", and three kinds of tetramers, "HLLL", "HHLL", "HHHL". All these trimers and tetramers states depends on the mass ratio m_H/m_L. There are some theoretic work about this problem, but most of them focus on the "HHHL" tetramers in the limit of $m_L/m_H \ll 1$ [153, 154].

8.3 Experimental in Na-Rb system

The three-body physics have been well studied in heteronuclear mixture of ^{6}Li-Cs[130, 131, 132, 133], ^{7}Li-^{87}Rb [134], ^{41}K-^{87}Rb [128] and ^{40}K-^{87}Rb [129]. However, except for the experiments of ^{40}K-^{87}Rb, other experiments focus on the $a < 0$ region. And no experimental observations of heteronuclear four-body resonances are reported. Therefore we use our Na-Rb Bose-Bose system to study some three-body and four-body processes. The experimental details are presented in this part.

8.3.1 Theoretical predictions for Na-Rb mixture

Thanks to previous works, the locations of Efimov resonances are predictable. The useful parameters of Na-Rb system are summarized here.

The 3BP parameter depends on short range details of Na-Rb ($r_{vdW} = 57.8a_0$ [3]) and Rb-Rb ($r_{vdW} = 82.6a_0$ [39]) interactions. According to [147, 155], the first NaRbRb Efimov resonance locates at

$$a_- = -13170a_0 \tag{8.16}$$

The scaling factors of the two kinds of Efimov trimers are [4, 136]

$$\begin{cases} \text{NaNaRb} : s_0 = 0.1565, e^{\pi/s_0} = 5.2 \times 10^8 \\ \text{NaRbRb} : s_0 = 0.8703, e^{\pi/s_0} = 36.96 \end{cases} \tag{8.17}$$

For "NaNaRb", the scaling factor is so large that it is impossible to observe more than one of this kind of Efimov resonances. For the more preferable trimer "NaRbRb", K. Helfrich *el al.,* [140] give a prediction of about the ratios between a_-, a_* and a_+ as

$$\frac{a_-}{a_*} = 99.1, \frac{a_-}{a_+} = e^{\pi/2s_0} = 6.08, \frac{a_+}{a_*} = \frac{99.1}{6.08} = 16.3. \tag{8.18}$$

Thus the atom-dimer resonance should be observed at $a_*^{(1)=133a_0}$, the three-body recombination minimum should be deteceted at $a_+^{(1)} = 2166a_0$.

Since the mass ratio between Na and Rb is 3.8, much smaller than the critical value 13 for two "HHHL" tetramers [154], there should be only one "NaRbRbRb" tetramer. The "NaNaRbRb" tetramer has four resonant interacting pairs of "Na-Rb", while "NaRbRbRb" has only three pairs. Therefore, the "NaNaRbRb" is bounded deeper than "NaRbRbRb" and there should

be at least one "NaNaRbRb" tetramer.

8.3.2 Atom-dimer collisions

We firstly study the dimer relaxation rate which have a resonance at a_*, where the Efimov trimer state is degenerate with the "atom-dimer" threshold. We focus on the "Rb-dimer" mixture since this combination have a smaller scaling factor.

After magneto-association, we use a blast laser to remove the unassociated Na atoms. Firstly a 30 μs MW ARP is used to transfer Na atoms from $|F=1, m_F=1\rangle$ to $|F=2, m_F=2\rangle$ state. Then a laser pulse, which is resonant with the $|F=2, m_F=2\rangle \leftrightarrow |F'=3, m'_F=3\rangle$ transition, pushes the Na atoms out of the trap in 5 μs. Repeating this process for several times, all Na atoms can be removed in 150 μs. (In this experiment, the MW system has been upgraded and the MW Rabi frequency is about 45 kHz.)

In this "Rb-dimer" mixture, the evolution of the dimer and Rb numbers obey differential equations as

$$\begin{cases} \dfrac{d}{dt} n_m(\mathbf{r},t) = -\gamma n_m(\mathbf{r},t) - 2\beta_{mm} n_m^2(\mathbf{r},t) - \beta_{am} n_m(\mathbf{r},t)\, n_a(\mathbf{r},t) \\ \dfrac{d}{dt} n_a(\mathbf{r},t) = -\gamma n_a(\mathbf{r},t) - \beta_{am} n_m(\mathbf{r},t)\, n_a(\mathbf{r},t) \end{cases} \tag{8.19}$$

here $n_i(\mathbf{r},t), (i=a,m)$ are the density of Rb atoms and dimers, respectively. β_{am} and β_{mm} are two-body collision rate for "Rb + dimer" and "dimer + dimer". Here we assume that one dimer is lost for every "Rb-dimer" collision and two dimer are lost for every "dimer-dimer" collision.

If $n_a \gg n_m$, the β_{am} term dominates the dimer loss. Integrating the

equation, we get

$$\frac{d}{dt}N_m\left(t\right) = -\beta_{am}C_{am}N_a\left(t\right)N_m\left(t\right). \tag{8.20}$$

$C_{am} = \int n_a\left(\mathbf{r}\right)n_m\left(\mathbf{r}\right)d\mathbf{r}/\left(N_aN_m\right)$ is the density overlap. In the limit of $N_a \gg N_m$, by assuming that the system is always in a thermal equilibrium state and with a constant temperature T, $N_m\left(t\right)$ obey a exponential decay function

$$N_m\left(t\right) = N_0e^{-K_{am}t} \tag{8.21}$$

where $K_{am} = \beta_{am}C_{am}N_a$.

In our Rb-dimer mixture, we have about 6×10^4 Rb and 6×10^3 dimer. The temperatures are measured to be $0.254(6)\mu$K ($0.465(28)$ μK) for Rb(dimer). And the trap frequencies are $2\pi \times \{43.0(1.4), 155.3(3.4), 155.3(3.4)\}$Hz for Rb and $2\pi \times \{44.7(1.5), 161.53.5, 161.5(3.5)\}$Hz for dimer. The calculated differential gravity sag δ_g is 4.87μm. The inhomogeneity of magnetic field is measured to be smaller than 0.5 G/cm at 347 G magnetic field, which has a neglectable effect for the atom-dimer density overlap. The size of Rb(dimer) sample in vertical direction is $7.1(2)\mu$m ($9.3(3)\mu$m), which are comparable with δ_g. Therefore, δ_g has to be taken into account when calculating C_{am}.

By tuning the magnetic field near the resonant magnetic field, we get the atom-dimer collision rates as Fig. 8.8 (b). In the spectrum a resonant peak is observed. Fitting the Rb-dimer data with E.q. 8.9 and $s_0 = 0.8703$, we get $C_2 = 1.13(3)$, $\eta_+ = 0.320(12)$ and $a_* = 184(3)a_0$. Compared with the prediction of $a_* = 133a_0$, the fitted value is about 40% larger. And the theoretical prediction of C_2 is 2.254 [140]. These discrepancies have also been observed in [129] and may due to the finite temperature effect. Another possible reason is that an assumption of $a_{\mathrm{NaNa}} = 0$ and $a_{\mathrm{NaRb}} \to \infty$ is used

in [140], which is invalid for our system. And the fitting function E.q. 8.21 is oversimplified for our experiments since the Rb-dimer mixture is not in a thermal equilibrium state by an estimation with E.q. 5.5.

8.3.3 Dimer-dimer collisions

We then study the dimer-dimer collisions. The pure Feshbach molecules sample is created by magneto-association and a magnetic gradient pulse as discussed in previous chapters. Then we ramp the magnetic field to various values in 3 ms. The number of dimers is recorded for different holding time.

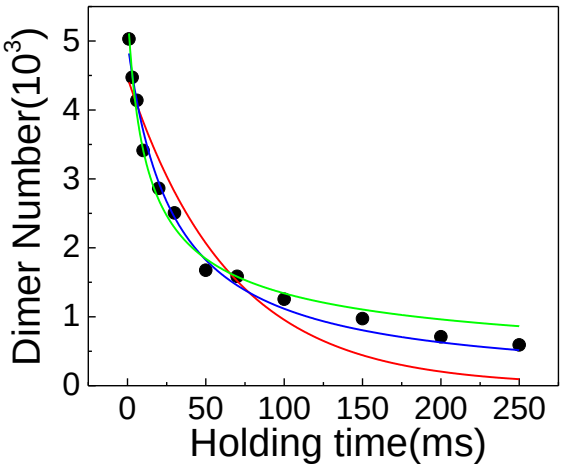

Figure 8.5: Typical loss curve of dimers. The dimer sample is prepared at $a = 900a_0$ and with a temperature about 0.327 μK. The red, blue and green solid lines are fitting results of pure one-, two- and three-body loss functions.

For a pure dimer system, the density $n(\mathbf{r}, t)$ obeys a differential equation

$$\frac{d}{dt}n(\mathbf{r}, t) = -\gamma n(\mathbf{r}, t) - n_\beta \beta n^2(\mathbf{r}, t) - n_\alpha \alpha n^3(\mathbf{r}, t) \tag{8.22}$$

where γ, β, α are event rates for the one-, two- and three-body loss processes and $n_{\beta,\alpha}$ are corresponding lost particle number in every collision event. Although some publications claim that n_α depends on experimental details and

can be larger than 3 [117, 156, 157] due to the avalanche mechanism, there is still debating on the validation of this model [158]. Therefore, we assume $n_\beta = 2$ and $n_\alpha = 3$ in this thesis. Other higher-body processes are neglected here. With a further approximation that the system is in a thermal equilibrium state and with a constant temperature T, the density is

$$n(\mathbf{r}, t) = N\bar{\omega}^3 \left(\frac{m}{2\pi k_B T}\right)^{3/2} \exp\left[-\frac{m\left(\omega_x^2 x^2 + \omega_y^2 y^2 + \omega_z^2\right)}{2k_B T}\right] \tag{8.23}$$

$\bar{\omega} = (\omega_x \omega_y \omega_z)^{1/3}$ is the average trap frequency. Integrating the sample we can get an equation of number $N(t)$ as

$$\frac{d}{dt}N(t) = -\gamma N(t) - K_2 N^2(t) - K_3 N^3(t) \tag{8.24}$$

where

$$K_2 = \left(\frac{m\bar{\omega}^2}{4\pi k_B T}\right)^{3/2} \beta n_\beta, K_3 = 3^{-3/2}\left(\frac{m\bar{\omega}^2}{2\pi k_B T}\right)^3 \alpha n_\alpha \tag{8.25}$$

This differential equation can be solved for different experimental parameters:

two-body loss: $K_2 N^2 \gg \gamma N, K_3 N^3$

$$N(t) = \frac{N_0}{1 + N_0 K_2 (t - t_0)} \tag{8.26}$$

three-body loss: $K_3 N^3 \gg \gamma N, K_2 N^2$

$$N(t) = \frac{N_0}{\sqrt{1 + K_3 N_0^2 (t - t_0)}} \tag{8.27}$$

one- and two-body loss: $\gamma N, K_2 N^2 \gg K_3 N^3$

$$N(t) = \frac{\gamma N_0}{(\gamma + K_2 N_0)\exp\left[\gamma (t - t_0)\right] - K_2 N_0} \tag{8.28}$$

one- and three-body loss: $\gamma N, K_3 N^3 \gg K_2 N^2$

$$N(t) = \sqrt{\frac{\gamma N_0^2}{(\gamma + K_3 N_0^2)\exp\left[2\gamma\left(t - t_0\right)\right] - K_3 N_0^2}} \tag{8.29}$$

For our experiment, the temperature of dimer is $\sim 0.327\mu$K, which is smaller than the dimer binding energies of all the measurements up to $2000a_0$ where the binding energy is about 1.2 μK. Therefore, the dimers only have a small possibility to be dissociated by dimer collisions with initial kinetic energy.

The two-body loss may result from three process: (1):"NaRb + NaRb $\rightarrow$ NaRbRb + Na", two dimers form a NaRbRb trimer which will be enhanced when NaRbRb trimer is degenerate with the "dimer + dimer" scattering continuum. (2):"NaRb + NaRb $\rightarrow$ NaNaRb + Rb", similar with (1) but associated with the NaNaRb trimer; and (3): "NaRb + NaRb $\rightarrow$ NaRb$'$ + NaRb$''$", collision with another dimer makes a dimer decay to deeply bounded molecular states and the released binding energy is taken away as kinetic energy, which is similar with the dimer relaxation. This process will be enhanced when the NaNaRbRb tetramer is degenerate with the "dimer+dimer" combination.

The possible three-body loss mechanism is similar with the situation of three atoms near a Feshbach resonance. Here two dimers can form a four-body state NaNaRbRb and the binding energy is transferred to kinetic energies and all the three dimers leave the trap. A three-body loss resonance should also be observed near critical scattering length where NaNaRbRb is degenerate with the "dimer+dimer" combination.

A typical loss curve is shown in Fig. 8.5. Fitted results of the one-, two- and three-body loss functions are shown with solid curves. It is clear that the one-body loss function (red curve) can not capture the loss feature. And the

fitting results of the two- and three-body loss functions work much better. However, it is hard to tell apart which one is correct. Actually, there is no obvious difference between the calculated χ^2 for these two fittings over all the measured a. Using "one- and two-body" loss function (E.q. 8.28) or "one- and three-body" loss fucntion (E.q. 8.29), we get unphysical results of γ. The results by fitting with "two- and three-body" loss function are not on a solid ground since the fitted results have large uncertainty. Therefore, it is the two-body and three-body loss functions are used to fit the data.

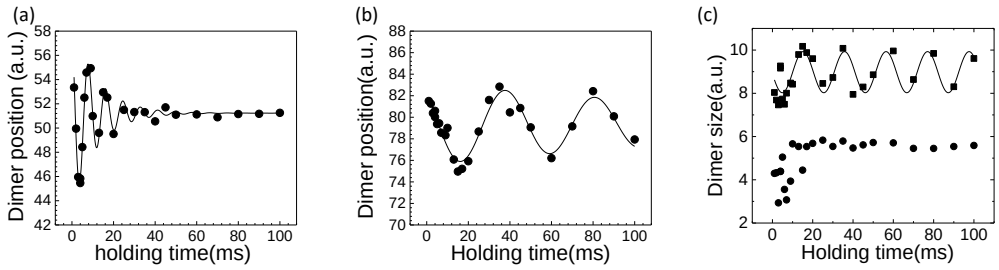

Figure 8.6: Dimer trap frequency measurement. (Measured with Rb signals.) After pure dimer sample is prepared, the dimer position is recorded for different holding times. The results are shown in (a) and (b) for z-(tightly confined) and x-(loosely confined) direction. (c) is the measured size of dimer sample for z-(dots) and x-(squares) directions. The solid lines are fittings of a damped/undamped sine curve.

In order to calculate the collision rate, number, temperature and trap frequencies have to be measured accurately. However, we observe oscillations of dimers' position and size, as shown in Fig. 8.6. Fitting with a damped sine curve, the damping time constant is about 12.0(1.7) ms for the dipole oscillations in z-direction. However, due to the unobvious damping behavior of the dipole oscialltion in x direction, the fitted result has a large uncertainty as 185(102)ms. Therefore, it is treated as an undamped oscillation in following calculations. With these data, we can get two trap frequencies as $\omega_z = 2\pi\times$ 120.2(5.1) Hz and $\omega_x = 2\pi\times$ 23.3(0.4) Hz. For the

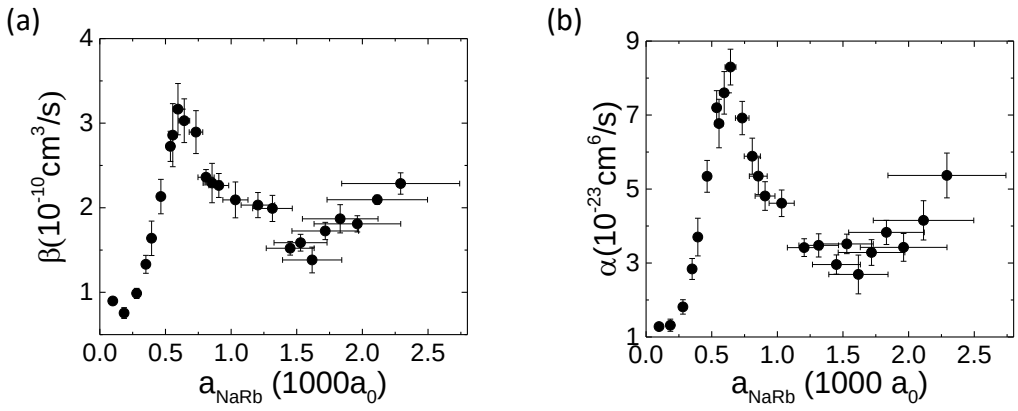

Figure 8.7: Collision rates for dimer system. (a) and (b) are fitted results of two-body and three-body loss functions respectively. Scattering lengths are calculated by considering two s-wave resonances [6] with formula $a(B) = a_{bg}\prod_{i=1,2}[1-\Delta_i/(B-B_{res,i})]$. Error bars of collision rates result from fitting process while error bars of scattering length comes from magnetic field calibrations, magnetic field stability of 10 mG and uncertainties of parameters of the two FRs.

measured size of the dimer sample, the oscillation in x-direction is quickly damped while it is not in z-direction. Fitted with an undamped sine function for the data of z-direction reveals a frequency of $\omega_3 = 2\pi\times$ 48.5(0.9) Hz. ω_x is about a half of ω_3 because ω_3 corresponds to the breathing mode while ω_x corresponds to the dipole mode of an excitation of a thermal cloud. By summarizing signals from Na and Rb, we get the trap freuqencies as $2\pi \times \{23.1(0.6), 121.1(5.6), 121.1(5.6)\}$ Hz. (Due to the cylindrical symmetry of the trap, we assign the trap frequency of y-direction is the same as that of the z-direction.) The temperature is measured to be $0.327(66)\mu$K with time of flight method after 100 ms holding time, when the oscillations in z-direction have damped out. In this measurement, the binding energy releasing during dissociation has been taken into consideration by let dimer fly before dissociation [159].

By tuning the magnetic field from 335.6 G to 347.48 G, we can measure

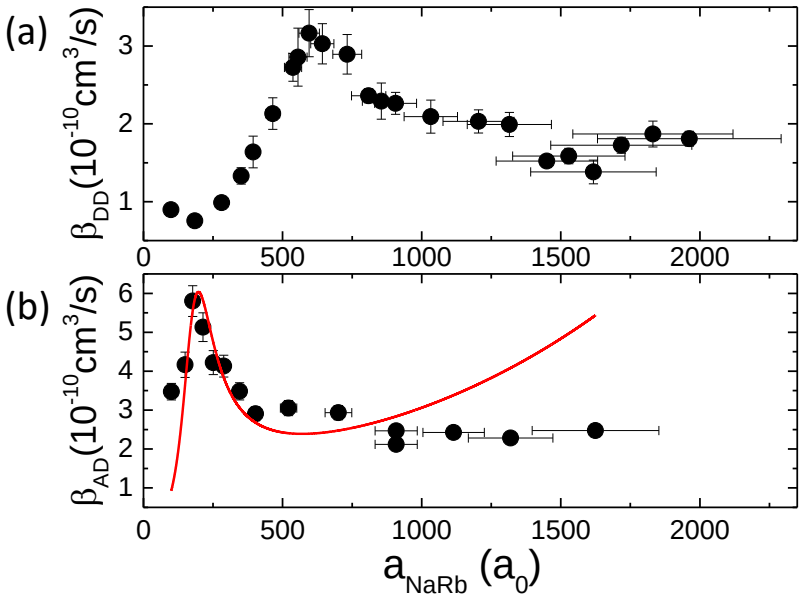

Figure 8.8: Collision rates for dimer-dimer(a) and Rb-dimer(b) system. The error bars of β comes from number, temperature and trap frequencies measurements while that of a comes from magnetic field calibration, stability of 10 mG and uncertainty of parameters of the two FRs. The solid curves in (b) is fitting result of E.q. 8.9.

the collisional rates for $100a_0 \leq a \leq 2000a_0$. (The upper limit is determined by $1/k$, where $k = \sqrt{2\mu k_B T}/\hbar$ is the thermal wave number and μ is the reduced mass of two dimers.) The overall behavior is shown in Fig. 8.7. Using the measured temperature, we can calculate the unitary limit of the two-body collision rate as $8\pi \langle v \rangle / k^2 = 3.8 \times 10^{-9} cm^{-3}/s$ and of the three-body collision rate as $\alpha_{max} = \frac{36\sqrt{3}\pi^2\hbar^5}{m^3(k_B T)^2} = 6.46 \times 10^{-23} cm^{-6}/s$. Which means that the fittings with the three-body loss function are non physical. Therefore, it is the two-body collisions which cause the loss of dimers.

There is a resonant peak located at $\sim 600a_0$ and a dip near $1500a_0$. (Fitting the specturm with a phenomenological function of "linear + Gaussian", we have the resonant peak at 658 a_0.) For a magnetic field further close to resonant magnetic field, the collision rate increases. The resonant peak

may come from the enhancement of "NaRb + NaRb → NaRb'+NaRb" " or "NaRb + NaRb → NaRbRb + Na" ("NaRb + NaRb → NaNaRb + Rb") as mentioned before. Here NaRb' and NaRb" are molecules with different internal degree of freedom. However, we cannot detect free atomic signals during the holding times. If a is close to the cross point of the trimer state and the "dimer + dimer" state, the energy difference between the "trimer+atom" and the "dimer+dimer" should be too small to let the generated free atoms run away from the trap. Therefore, it is believed that this loss resonance results from tetramer NaNaRbRb.

Comparing the measured "atom+dimer" and "dimer+dimer" collision rates, as shown in Fig. 8.8, the resonant peak of β_{AD} is right at a minimum of β_{DD}. (It is an one-point minimum right now. We will take more data later.) A similar result has been observed and explained in the homonuclear situation [160, 151]. At the a_*, the dimer-dimer scattering length approaches zero and there is a dimer-dimer recombination minimum. (In the experiments of [160], only the recombination minimum is observed.)

According to numerical calculations by Prof. Doerte Blume (WSU), the ratio of $a_\#/a_*$ is about 2.5. ($a_\#$ is defined for the intersectant point of the NaNaRbRb tetramer and the NaRbRb trimer.) (In the calculation a zero-range approximation is used, the two-body potentials are the attractive Gaussian potentials, and a repulsive three-body potential is used to stabilize the system. For more details, please read the upcoming publications.) However, the experimental result is 3.6. More experimental and theoretical works are needed to understand these observations.

□ End of Chapter.

Chapter 9

Outlook

The NaRb FMs have been successfully transferred to the rovibrational ground state with STIRAP [49]. Different hyperfine states of NaRb molecules, including the absolute ground state with $M_F = m_I^{Na} + m_I^{Rb} = 3$, can be reached by changing the polarizations and frequencies of the STIRAP lasers. The one way STIRAP efficiency is about 80%. An electric field as high as 1.5 kV/cm is created which can induce a dipole moment larger than 1 Debye. However the measured two-body loss rate coefficient of the ground state NaRb molecules is as high as $2.5(9) \times 10^{-10}$ cm$^3\cdot$ s^{-1}, which limits the lifetime of the NaRb molecules to be about 200 ms. Works are underway to study the mechanisms of such large loss rates. Possible reasons are photo-association effect of the ODT laser, collisions with molecules in excited states due to the imperfect STIRAP process, and sticky collisions caused by formation of four-body complex. In order to increase the lifetime of NaRb molecules, we can load them into the optical lattice. Another method is using a DC electric field to shielding the collisions when the molecules are populated into the rotation state of $J'' = 1$. The principle of this shielding mechanism was explained in [161, 162]. The basic idea is as follows. Thanks to the coupling

between different rotation levels, the adiabatic potential of the incident channel which are composed of two $J'' = 1$ molecules has a repulsive barrier at certain DC field. So the two molecules cannot approach one another as close as before. Consequently, this shielding reduces the possibility of the inelastic collisions as well as chemical reactions.

The significance of formation of ultracold ground state dipolar molecules are well reviewed in many articles [163, 24]. With the integrated dipole-dipole interactions, there are many novel quantum effects like super-solid phases [164, 165, 24], dipolar crysalline phases [166]. The possible applications of ultracold dipolar moelcules are not limited to the realization of models with more complex Hamiltonians but also a new platform for quantum computation [167, 168].

Both Na and Rb are suitable for study physics of spinor gases. We have observed the heteronuclear coherent spin dynamics [66]. And it also be proved that a vector light shift can be used to control the heteronuclear collision process. The double spinor gases are a possible realization of bosonic Kondo model by replacing the two orbits with two different kinds of atoms. Another possible application is generating entanglement between distinguishable atoms.

There are plenty of other experiments when the interspecies interactions are tuned to be resonant. If the number ratio of these two kinds of atoms are large, we can study the impurity problem in a boson-boson system [169, 170, 171]. On the other hand, the few-body experiments can be pushed further with colder atom-dimer and dimer-dimer mixtures.

□ End of Chapter.

Appendix A

Na and Rb laser

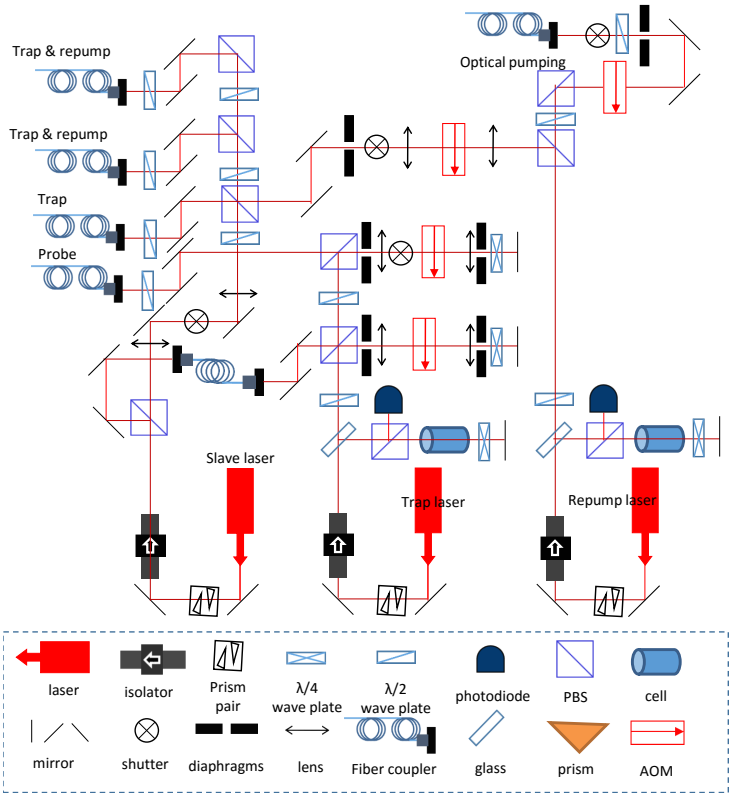

Figure A.1: Optical layout of Rb lasers.

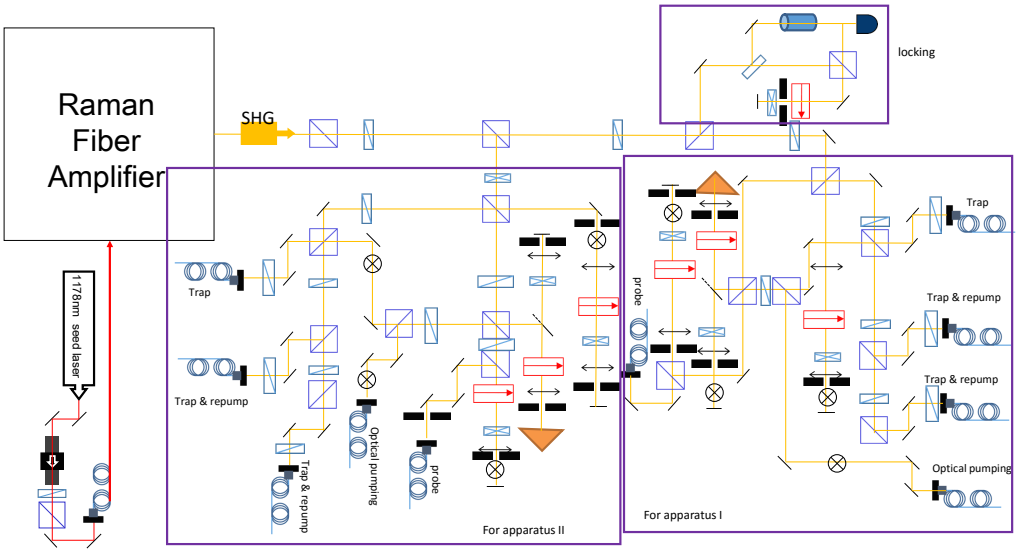

Figure A.2: Optical layout of Na lasers.

□ End of Chapter.

Appendix B

Numerical simulation of the coupled GP equations

In this part, I will describe how we numerically simulate the density distribution of the dBECs.

Let us firstly recall the coupled GP equations:

$$\begin{cases} \left[-\dfrac{\hbar^2}{2m_1}+V_{ext,1}+g_{11}|\phi_1|^2+g_{12}|\phi_2|^2\right]\phi_1 = \mu_1\phi_1 \\ \left[-\dfrac{\hbar^2}{2m_2}+V_{ext,2}+g_{12}|\phi_1|^2+g_{22}|\phi_2|^2\right]\phi_2 = \mu_2\phi_2 \end{cases} \tag{B.1}$$

Where the gravity acceleration, atom mass, reduced mass, atom numbers, chemical potentials, intra-(inter-) species s-wave scattering lengths, intra(inter-) species interaction strengths and the external potentials are m_i, $m_{ij} = \frac{m_i m_j}{m_i+m_j}$, N_i, μ_i, a_{ij}, $g_{ij} = \frac{2\pi\hbar^2 a_{ij}}{m_{ij}}$, $V_{ext,i} = m_i\left(\omega_{x,i}^2x^2+\omega_{y,i}^2y^2+\omega_{z,i}^2z^2\right)/2 + m_igz\,(i=1,2)$, respectively. The wave functions ϕ_1, ϕ_2 are normalized by $N_i = \int d\mathbf{r}n_i = \int d\mathbf{r}|\phi_i|^2, (i=1,2)$

In order to obtain the ground state of the dBECs, one need minimize the

total energy of this system

$$E = \int d\mathbf{r} \left(\frac{\hbar^2}{2m_1} |\nabla \phi_1|^2 + V_{ext,1}(\mathbf{r}) |\phi_1|^2 + \frac{\hbar^2}{2m_2} |\nabla \phi_2|^2 + V_{ext,2}(\mathbf{r}) |\phi_2|^2 + \frac{1}{2} g_{11} |\phi_1|^4 + \frac{1}{2} g_{22} |\phi_2|^4 + g_{12} |\phi_1|^2 |\phi_2|^2 \right) \tag{B.2}$$

Typically it is difficult to get an analytical solution. However one can use numerical methods to get the ground state density distribution. One widely used method is the steepest-descent approach, which is applicable to find a minimum of a function with several variables [172]. The essence of this method is "continuously projecting onto the minimum of the functional an initial trial state by propagating it in imaginary time" [173]. As the imaginary time goes to infinity, the trial function will converge to the exact solution. The time evolution reads

$$\frac{\partial}{\partial t} \phi(\mathbf{r}, t) = -\frac{\overline{\delta} E}{\overline{\delta} \phi^*(\mathbf{r}, t)} \tag{B.3}$$

where $\overline{\delta}$ indicate the constrained functional derivative that preseves the normalization. It means that at each step defined by δt, the wavefunction moves a little along the gradient $-\overline{\delta} E / \overline{\delta} \phi^*(\mathbf{r}, t)$. The functional derivative could be obtained by

$$\frac{\delta E}{\delta \phi^*(\mathbf{r}, t)} = H \phi(\mathbf{r}, t) \tag{B.4}$$

where the Hamiltonian relies on the wave functions of previous step. The end results corresponding to $\partial \phi(\mathbf{r}, t) / \partial t = 0$. In practice, we choose small time step Δt and use

$$\phi(\mathbf{r}, t + \Delta t) = \frac{\phi(\mathbf{r}, t) - \Delta t H \phi(\mathbf{r}, t)}{|\phi(\mathbf{r}, t) - \Delta t H \phi(\mathbf{r}, t)|} \sqrt{N} \tag{B.5}$$

as the iterating equation until the converge condition is fulfilled. The mentioned equation above can be directly used to obtain the ground state of single species BEC. And it is easy to be generalized to dBECs

$$\begin{cases} \phi_1(\mathbf{r}, t+\Delta t) = & \dfrac{\phi_1(\mathbf{r},t) - \Delta t H_1 \phi_1(\mathbf{r},t)}{|\phi_1(\mathbf{r},t) - \Delta t H_1 \phi_1(\mathbf{r},t)|}\sqrt{N_1} \\ \phi_2(\mathbf{r}, t+\Delta t) = & \dfrac{\phi_2(\mathbf{r},t) - \Delta t H_2 \phi_2(\mathbf{r},t)}{|\phi_2(\mathbf{r},t) - \Delta t H_2 \phi_2(\mathbf{r},t)|}\sqrt{N_2} \end{cases} \tag{B.6}$$

where the Hamiltonians are

$$\begin{cases} H_1(\mathbf{r}) = & -\dfrac{\hbar^2}{2m_1}\nabla^2 + V_{ext,1}(\mathbf{r}) + g_{11}|\phi_1(\mathbf{r})|^2 + g_{12}|\phi_2(\mathbf{r})|^2 \\ H_2(\mathbf{r}) = & -\dfrac{\hbar^2}{2m_2}\nabla^2 + V_{ext,2}(\mathbf{r}) + g_{12}|\phi_1(\mathbf{r})|^2 + g_{22}|\phi_2(\mathbf{r})|^2 \end{cases} \tag{B.7}$$

In order to avoid dealing with small numbers, it is useful to transform the equations to some dimensionless ones with the following rules

$$\begin{cases} t \to \dfrac{t}{\omega_m}, \omega_m = min\{\omega_{x,1}, \omega_{y,1}, \omega_{z,1}, \omega_{x,2}, \omega_{y,2}, \omega_{z,2}\} \\ x \to x a_0, a_0 = \sqrt{\hbar/m_1\omega_m} \\ \phi_i \to \phi_i / a_0^{3/2} \\ \Omega \to \Omega\omega_m \\ E(\cdot) \to \hbar\omega_m E(\cdot) \\ g \to g a_0 \omega_m^2 \end{cases} \tag{B.8}$$

This transformation can be directly used to the equal mass dBECs. But for the unequal mass case, there is a factor shows up when doing the transfor-

Table B.1: Splitting methods

name	formula	error
Lie	$e^{iH_K\Delta t}e^{iH_I\Delta t}$	$i\Delta t^2\frac{[H_K,H_I]}{2}+O\left(\Delta t^3\right)$
Strang	$e^{iH_K\Delta t/2}e^{iH_I\Delta t}e^{iH_K\Delta t/2}$	$i\Delta t^3\left(\frac{[H_I,[H_I,H_K]]}{12}-\frac{[H_K,[H_K,H_I]]}{24}\right)+O\left(\Delta t^4\right)$
SWSS	$\frac{\left(e^{iH_K\Delta t}e^{iH_I\Delta t}+e^{iH_I\Delta t}e^{iH_K\Delta t}\right)}{2}$	$O\left(\Delta t^3\right)$

mation:

$$\begin{cases} H_1 = -\frac{1}{2}\hbar\omega_m\left(\frac{\partial^2}{\partial x^2}+\frac{\partial^2}{\partial y^2}+\frac{\partial^2}{\partial z^2}\right)+\frac{1}{2}\hbar\omega_m\left(\gamma_{x,1}^2x^2+\gamma_{y,1}^2y^2+\gamma_{z,1}^2z^2\right) \\ \quad +\hbar\omega_m\beta_{11}|\phi_1|^2+\hbar\omega_m\beta_{12}|\phi_2|^2 \\ H_2 = -\frac{1}{2}\hbar\omega_m\left(\frac{m_1}{m_2}\right)\left(\frac{\partial^2}{\partial x^2}+\frac{\partial^2}{\partial y^2}+\frac{\partial^2}{\partial z^2}\right)+\frac{1}{2}\hbar\omega_m\left(\frac{m_2}{m_1}\right)\left(\gamma_{x,2}^2x^2\right. \\ \quad \left.+\gamma_{y,2}^2y^2+\gamma_{z,2}^2z^2+\hbar\omega_m\beta_{12}|\phi_1|^2+\hbar\omega_m\beta_{22}|\phi_2|^2\right. \end{cases} \tag{B.9}$$

where $\gamma_{i,j}=\omega_{i,j}/\omega_m,(i=x,y,z;j=1,2)$ and $\beta_{11}=\frac{4\pi a_{11}}{a_0}$,$\beta_{22}=\frac{4\pi a_{22}m_1}{a_0m_2}$,$\beta_{12}=\frac{2\pi a_{12}(m_1+m_2)}{a_0m_2}$. We need note that in this calculation, a coordinate move transformation about $z_1\to z_a+g/\omega_{z,1}^2$ and $z_2\to z_2+g/\omega_{z,2}$ are performed for these two atoms and the energy zero points also chaneged about $\frac{m_1}{2}\frac{g^2}{\omega_{z,1}^2}$ and $\frac{m_2}{2}\frac{g^2}{\omega_{z,2}^2}$. The mentioned equations above can be used to solve static problems such as simulating the ground state of dBECs. However, in order to solve the dynamic ones, a time splitting is necessary.

For a dimensionless time dependent GP equation

$$i\frac{\partial}{\partial t}\phi=\left(-\frac{1}{2}\nabla^2+V+\beta\left|\phi\right|\right)\phi \tag{B.10}$$

the kinetic part $H_K=-\frac{1}{2}\nabla^2$ is diagonalized in the momentum space while the remaining part $H_I=V+\beta\left|\phi\right|$ is diagonalized in the real space. Therefore one can split the total Hamiltonian into H_K and H_I and then solve this

equation in the two spaces separately. Although

$$e^{i(H_K+H_I)\Delta t} \neq e^{iH_I\Delta t}e^{iH_K\Delta t}. \tag{B.11}$$

there are kinds of splitting methods summarized in Table. B.1. Taking the Strang splitting as an example: with certain t and wave function $\phi(t)$, we can get $\phi(t+\Delta t)$ with following steps:

$$\begin{aligned}
\phi_1 &= e^{iH_I(t)\Delta t/2}\phi(t) \\
\phi_2 &= \mathcal{F}[\phi_1] \\
\phi_3 &= e^{iH_K(t)\Delta t}\phi_2 \\
\phi_4 &= \mathcal{F}^{-1}[\phi_3] \\
\phi_5 &= e^{iH_I(t)\Delta t/2}\phi_4 \\
\phi(t+\Delta t) &= \phi_5/|\phi_5|
\end{aligned} \tag{B.12}$$

Here $\mathcal{F}$ and $\mathcal{F}^{-1}$ are the Fourier and inverse Fourier transformation, respectively.

In principle, this method can be used to simulate the time of flight by expressing

$$V(t) = \begin{cases} V_0, & (t \leq 0) \\ V_g, & (t > 0) \end{cases} \tag{B.13}$$

where $V_0 = V_{ext}(x,y,z) + V_g$ is the trap potential including the gravity potential V_g. However, since the atomic cloud expands fast, a large volume needs to be meshed which costs too much computation resources. Therefore, I only simulate the ground state density distribution in this thesis.

After calculating the density distributions of the dBECs with home written codes, I find that there is an open source Matlab package for solving static and dynamic GP equations [174, 175]. It is more powerful and flexible

to solve different kinds of problems.

□ End of Chapter.

Appendix C

Coils construction

There are many coils used in our apparatus. Details of simulation of the magnetic fields and the construction of coils will be introduced in this part.

C.1 Magnetic Field Simulation

Usually, the coils are combinations of two basic configurations: a single turn coil and a finite length straight wire. It is useful to calculate magnetic fields generated by this two configurations (Fig. C.1) [176]

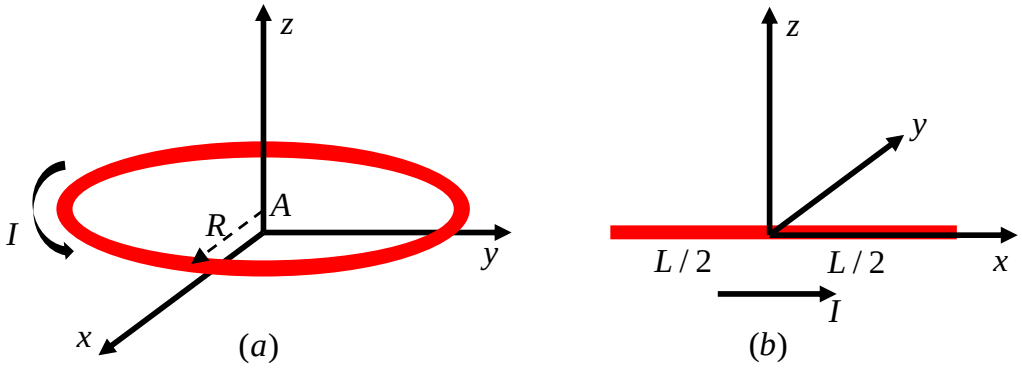

Figure C.1: Configurations of a single turn coil(a) and a finite length straight wire(b). The current is I.

Single turn coil: A single coil with radius of R is placed in the plane of $z = A$ and centered at $(x, y, z) = (0, 0, A)$ The fields are

$$\begin{cases} B_z = \dfrac{\mu_0 I}{2\pi} \dfrac{1}{\left[(R+\rho)^2 + (z-A)^2\right]^{1/2}} \left[\mathcal{K}\left(k^2\right) + \dfrac{R^2 - \rho^2 - (z-A)^2}{(R-\rho)^2 + (z-A)^2} \mathcal{E}\left(k^2\right)\right] \\ B_x = \dfrac{y}{\rho} \times \dfrac{\mu_0 I}{2\pi\rho} \dfrac{z-A}{\left[(R+\rho)^2 + (z-A)^2\right]^{1/2}} \left[-\mathcal{K}\left(k^2\right) + \dfrac{R^2 + \rho^2 + (z-A)^2}{(R-\rho)^2 + (z-A)^2} \mathcal{E}\left(k^2\right)\right] \\ B_y = \dfrac{x}{\rho} \times \dfrac{\mu_0 I}{2\pi\rho} \dfrac{z-A}{\left[(R+\rho)^2 + (z-A)^2\right]^{1/2}} \left[-\mathcal{K}\left(k^2\right) + \dfrac{R^2 + \rho^2 + (z-A)^2}{(R-\rho)^2 + (z-A)^2} \mathcal{E}\left(k^2\right)\right] \end{cases} \tag{C.1}$$

where $\mathcal{K}$ and $\mathcal{E}$ are the first and second kinds of complete elliptic integrals. $k^2 = 4R\rho/\left[(R+\rho)^2 + (z-A)^2\right]$ and $\rho = \sqrt{x^2 + y^2}$. μ_0 is vacuum permeability.

Finite length straight wire: A straight wire with length L is placed in at x-axis. The center is $x = 0$ and current is I:

$$\begin{cases} B_x = 0 \\ B_y = \dfrac{z}{\sqrt{y^2+z^2}} \dfrac{\mu_0 I}{4\pi\sqrt{y^2+z^2}} \left[\dfrac{L/2 - x}{\sqrt{(L/2-x)^2 + y^2 + z^2}} - \dfrac{-L/2 - x}{\sqrt{(-L/2-x)^2 + y^2 + z^2}}\right] \\ B_z = \dfrac{y}{\sqrt{y^2+z^2}} \dfrac{\mu_0 I}{4\pi\sqrt{y^2+z^2}} \left[\dfrac{L/2 - x}{\sqrt{(L/2-x)^2 + y^2 + z^2}} - \dfrac{-L/2 - x}{\sqrt{(-L/2-x)^2 + y^2 + z^2}}\right] \end{cases} \tag{C.2}$$

These six equations can be used to simulate the magnetic fields of kinds of coils when combined with spatial translation transformation and rotation transformation. Then it is easy to optimize the coils' configurations for different purposes, such as a homogenous magnetic field.

C.2 Coils Winding

There are two kinds of winding method: standard winding and back-winding. It is easy to wind a standard pattern, but one end is at the inner side of the coil while the other end is at the outer side. This winding makes the coil one

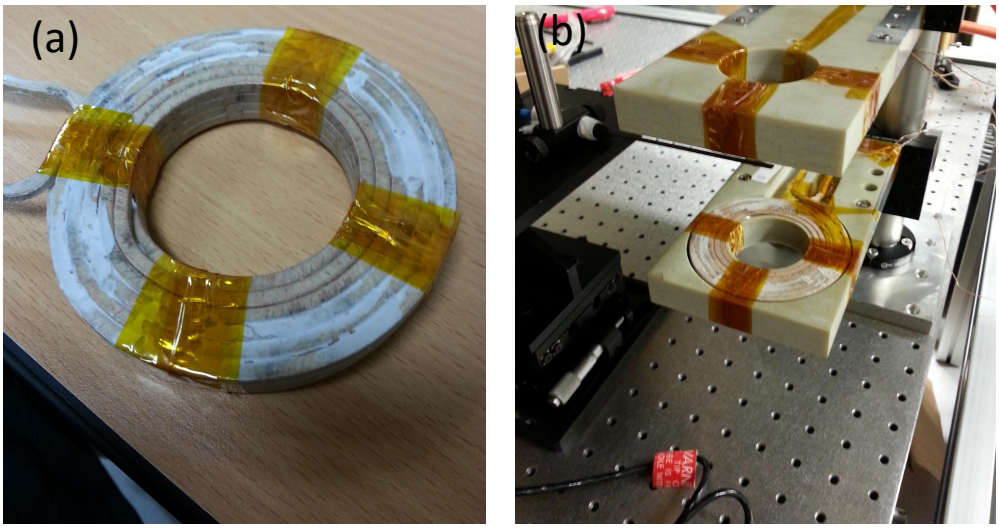

Figure C.2: One winded QT coil(a) and the testing of the QT coil pair by measuring the magnetic field with a Gauss meter (b).

layer thicker than the ideal one. What is more, the magnetic fields generated by these two ends can not cancel each other and consequently which will affect the homogeneity of the magnetic field. The back-winding is not a straight-forward method but it has the advantage that both ends project radially form the coil and the thickness exactly equals the ideal one. By binding the two ends together, the inhomogeneity caused by the non-ideal winding can be minimized.

We design some molds for these coil inspired by [177]. We wind the coils with a lathe. The molds are mounted in the headstock spindle, copper tube is fixed on the carriage via a Teflon cube. This Teflon cube helps to avoid copper tube twisting during winding process and protects the isolation layer. Firstly we fix the headstock position and manually wind the first layer of the coil. Then we fix the corresponding end on the mold and rotate the headstock spindle to wind other layers. The expoxy (NM25 500, Cotronics) is applied during the winding. Since the cure time is about 4 hours, we have to finish the winding in less than 2 hours. It is important to apply some lubricating

grease on the surface of the molds before the winding in order to remove the them after the epoxy cures. One winded coil is shown in Fig. C.2.

□ End of Chapter. bibliography

Bibliography

[1] Johannes Deiglmayr, Mireille Aymar, Roland Wester, Matthias Weidemller, and Olivier Dulieu. Calculations of static dipole polarizabilities of alkali dimers: Prospects for alignment of ultracold molecules. *The Journal of Chemical Physics*, 129(6), 2008.

[2] M. Aymar and O. Dulieu. Calculation of accurate permanent dipole moments of the lowest $^{1,3}\Sigma^+$ states of heteronuclear alkali dimers using extended basis sets. *The Journal of Chemical Physics*, 122(20), 2005.

[3] Fudong Wang, Dezhi Xiong, Xiaoke Li, Dajun Wang, and Eberhard Tiemann. Observation of Feshbach resonances between ultracold Na and Rb atoms. *Phys. Rev. A*, 87:050702, May 2013.

[4] Eric Braaten and H.-W. Hammer. Universality in few-body systems with large scattering length. *Physics Reports*, 428(5—6):259 – 390, 2006.

[5] Brett D. Esry and Chris H. Greene. Quantum physics: A menage a trois laid bare. *Nature*, 440(7082):289–290, March 2006.

[6] Fudong Wang, Xiaodong He, Xiaoke Li, Bing Zhu, Jun Chen, and Dajun Wang. Formation of ultracold NaRb Feshbach molecules. *New Journal of Physics*, 17(3):035003, 2015.

[7] S. N. Bose. Planck's Law and Light Quantum Hypothesis. *Zeitschrift für Physics*, 26:1–4, 1924.

[8] A. Einstein. Quantum theory of the monoatomic ideal gas. *Sitzungsberichte*, V:161–167, 1924.

[9] M. H. Anderson, J. R. Ensher, M. R. Matthews, C. E. Wieman, and E. A. Cornell. Observation of Bose-Einstein Condensation in a Dilute Atomic Vapor. *Science*, 269(5221):198–201, 1995.

[10] K. B. Davis, M. O. Mewes, M. R. Andrews, N. J. van Druten, D. S. Durfee, D. M. Kurn, and W. Ketterle. Bose-Einstein Condensation in a Gas of Sodium Atoms. *Phys. Rev. Lett.*, 75:3969–3973, Nov 1995.

[11] C. C. Bradley, C. A. Sackett, J. J. Tollett, and R. G. Hulet. Evidence of Bose-Einstein Condensation in an Atomic Gas with Attractive Interactions. *Phys. Rev. Lett.*, 75:1687–1690, Aug 1995.

[12] B. DeMarco and D. S. Jin. Onset of Fermi Degeneracy in a Trapped Atomic Gas. *Science*, 285(5434):1703–1706, 1999.

[13] Alexander L. Fetter. Rotating trapped Bose-Einstein condensates. *Rev. Mod. Phys.*, 81:647–691, May 2009.

[14] S. Inouye, M. R. Andrews, J. Stenger, H.-J. Miesner, D. M. Stamper-Kurn, and W. Ketterle. Observation of Feshbach resonances in a Bose-Einstein condensate. *Nature*, 392(6672):151–154, March 1998.

[15] Cheng Chin, Rudolf Grimm, Paul Julienne, and Eite Tiesinga. Feshbach resonances in ultracold gases. *Rev. Mod. Phys.*, 82:1225–1286, Apr 2010.

[16] Markus Greiner, Olaf Mandel, Tilman Esslinger, Theodor W. Hansch, and Immanuel Bloch. Quantum phase transition from a superfluid to a Mott insulator in a gas of ultracold atoms. *Nature*, 415(6867):39–44, January 2002.

[17] Immanuel Bloch, Jean Dalibard, and Wilhelm Zwerger. Many-body physics with ultracold gases. *Rev. Mod. Phys.*, 80:885–964, Jul 2008.

[18] T. Kraemer, M. Mark, P. Waldburger, J. G. Danzl, C. Chin, B. Engeser, A. D. Lange, K. Pilch, A. Jaakkola, H.-C. Ngerl, and R. Grimm. Evidence for Efimov quantum states in an ultracold gas of caesium atoms. *Nature*, 440(7082):315–318, March 2006.

[19] K.-K. Ni, S. Ospelkaus, M. H. G. de Miranda, A. Pe'er, B. Neyenhuis, J. J. Zirbel, S. Kotochigova, P. S. Julienne, D. S. Jin, and J. Ye. A High Phase-Space-Density Gas of Polar Molecules. *Science*, 322(5899):231–235, 2008.

[20] Dan M. Stamper-Kurn and Masahito Ueda. Spinor Bose gases: Symmetries, magnetism, and quantum dynamics. *Rev. Mod. Phys.*, 85:1191–1244, Jul 2013.

[21] C. A. Regal, M. Greiner, and D. S. Jin. Observation of Resonance Condensation of Fermionic Atom Pairs. *Phys. Rev. Lett.*, 92:040403, Jan 2004.

[22] M. W. Zwierlein, C. A. Stan, C. H. Schunck, S. M. F. Raupach, A. J. Kerman, and W. Ketterle. Condensation of Pairs of Fermionic Atoms near a Feshbach Resonance. *Phys. Rev. Lett.*, 92:120403, Mar 2004.

[23] M.A. Baranov. Theoretical progress in many-body physics with ultracold dipolar gases. *Physics Reports*, 464(3):71 – 111, 2008.

[24] M. A. Baranov, M. Dalmonte, G. Pupillo, and P. Zoller. Condensed Matter Theory of Dipolar Quantum Gases. *Chemical Reviews*, 112(9):5012–5061, 2012. PMID: 22877362.

[25] J L Bohn, M Cavagnero, and C Ticknor. Quasi-universal dipolar scattering in cold and ultracold gases. *New Journal of Physics*, 11(5):055039, 2009.

[26] K. Aikawa, S. Baier, A. Frisch, M. Mark, C. Ravensbergen, and F. Ferlaino. Observation of Fermi surface deformation in a dipolar quantum gas. *Science*, 345(6203):1484–1487, 2014.

[27] B. Capogrosso-Sansone, C. Trefzger, M. Lewenstein, P. Zoller, and G. Pupillo. Quantum Phases of Cold Polar Molecules in 2D Optical Lattices. *Phys. Rev. Lett.*, 104:125301, Mar 2010.

[28] Goulven Qumner and Paul S. Julienne. Ultracold Molecules under Control! *Chemical Reviews*, 112(9):4949–5011, 2012. PMID: 22921011.

[29] Piotr S. Żuchowski and Jeremy M. Hutson. Reactions of ultracold alkali-metal dimers. *Phys. Rev. A*, 81:060703, Jun 2010.

[30] Tetsu Takekoshi, Lukas Reichsöllner, Andreas Schindewolf, Jeremy M. Hutson, C. Ruth Le Sueur, Olivier Dulieu, Francesca Ferlaino, Rudolf Grimm, and Hanns-Christoph Nägerl. Ultracold Dense Samples of Dipolar RbCs Molecules in the Rovibrational and Hyperfine Ground State. *Phys. Rev. Lett.*, 113:205301, Nov 2014.

[31] Peter K. Molony, Philip D. Gregory, Zhonghua Ji, Bo Lu, Michael P. Köppinger, C. Ruth Le Sueur, Caroline L. Blackley, Jeremy M. Hutson, and Simon L. Cornish. Creation of Ultracold $^{87}Rb^{133}Cs$ Molecules in

the Rovibrational Ground State. *Phys. Rev. Lett.*, 113:255301, Dec 2014.

[32] Jee Woo Park, Sebastian A. Will, and Martin W. Zwierlein. Ultracold Dipolar Gas of Fermionic $^{23}Na^{40}K$ Molecules in Their Absolute Ground State. *Phys. Rev. Lett.*, 114:205302, May 2015.

[33] Matthew T. Hummon, Mark Yeo, Benjamin K. Stuhl, Alejandra L. Collopy, Yong Xia, and Jun Ye. 2D Magneto-Optical Trapping of Diatomic Molecules. *Phys. Rev. Lett.*, 110:143001, Apr 2013.

[34] J. F. Barry, D. J. McCarron, E. B. Norrgard, M. H. Steinecker, and D. DeMille. Magneto-optical trapping of a diatomic molecule. *Nature*, 512(7514):286–289, August 2014.

[35] E. B. Norrgard, D. J. McCarron, M. H. Steinecker, M. R. Tarbutt, and D. DeMille. Submillikelvin Dipolar Molecules in a Radio-Frequency Magneto-Optical Trap. *Phys. Rev. Lett.*, 116:063004, Feb 2016.

[36] Johann G. Danzl, Elmar Haller, Mattias Gustavsson, Manfred J. Mark, Russell Hart, Nadia Bouloufa, Olivier Dulieu, Helmut Ritsch, and Hanns-Christoph Nägerl. Quantum Gas of Deeply Bound Ground State Molecules. *Science*, 321(5892):1062–1066, 2008.

[37] F. Lang, K. Winkler, C. Strauss, R. Grimm, and J. Hecker Denschlag. Ultracold Triplet Molecules in the Rovibrational Ground State. *Phys. Rev. Lett.*, 101:133005, Sep 2008.

[38] S. Knoop, T. Schuster, R. Scelle, A. Trautmann, J. Appmeier, M. K. Oberthaler, E. Tiesinga, and E. Tiemann. Feshbach spectroscopy and analysis of the interaction potentials of ultracold sodium. *Phys. Rev. A*, 83:042704, Apr 2011.

[39] A. Marte, T. Volz, J. Schuster, S. Dürr, G. Rempe, E. G. M. van Kempen, and B. J. Verhaar. Feshbach Resonances in Rubidium 87: Precision Measurement and Analysis. *Phys. Rev. Lett.*, 89:283202, Dec 2002.

[40] A. Pashov, O. Docenko, M. Tamanis, R. Ferber, H. Knöckel, and E. Tiemann. Potentials for modeling cold collisions between Na (3S) and Rb (5S) atoms. *Phys. Rev. A*, 72:062505, Dec 2005.

[41] Thorsten Köhler, Krzysztof Góral, and Paul S. Julienne. Production of cold molecules via magnetically tunable Feshbach resonances. *Rev. Mod. Phys.*, 78:1311–1361, Dec 2006.

[42] K. Bergmann, H. Theuer, and B. W. Shore. Coherent population transfer among quantum states of atoms and molecules. *Rev. Mod. Phys.*, 70:1003–1025, Jul 1998.

[43] K. Winkler, F. Lang, G. Thalhammer, P. v. d. Straten, R. Grimm, and J. Hecker Denschlag. Coherent Optical Transfer of Feshbach Molecules to a Lower Vibrational State. *Phys. Rev. Lett.*, 98:043201, Jan 2007.

[44] Shunji Kasahara, Tsuyoshi Ebi, Mari Tanimura, Heiji Ikoma, Kensuke Matsubara, Masaaki Baba, and Hajime Kat. High-resolution laser spectroscopy of the X $^1\Sigma^+$ and $(1)^3\Sigma^+$ states of $^{23}Na^{85}Rb$ molecule. *The Journal of Chemical Physics*, 105(4):1341–1347, 1996.

[45] W.C Stwalley. Efficient conversion of ultracold Feshbach-resonance-related polar molecules into ultracold ground state ($X^1\Sigma^+$ v = 0, J = 0) molecules. *The European Physical Journal D-Atomic, Molecular, Optical and Plasma Physics*, 31(2):221–225, 2004.

[46] O. Docenko, M. Tamanis, R. Ferber, E. A. Pazyuk, A. Zaitsevskii, A. V. Stolyarov, A. Pashov, H. Knöckel, and E. Tiemann. Deperturbation treatment of the $A\,^1\Sigma^{+\smile}b\,^3\Pi$ complex of NaRb and prospects for ultracold molecule formation in $X\,^1\Sigma^+(v = 0; J = 0)$. *Phys. Rev. A*, 75:042503, Apr 2007.

[47] S. Ospelkaus, K.-K. Ni, G. Quéméner, B. Neyenhuis, D. Wang, M. H. G. de Miranda, J. L. Bohn, J. Ye, and D. S. Jin. Controlling the Hyperfine State of Rovibronic Ground-State Polar Molecules. *Phys. Rev. Lett.*, 104:030402, Jan 2010.

[48] N. V. Vitanov and S. Stenholm. Adiabatic population transfer via multiple intermediate states. *Phys. Rev. A*, 60:3820–3832, Nov 1999.

[49] Mingyang Guo, Bing Zhu, Bo Lu, Xin Ye, Fudong Wang, Romain Vexiau, Nadia Bouloufa-Maafa, Goulven Quéméner, Olivier Dulieu, and Dajun Wang. Creation of an Ultracold Gas of Ground-State Dipolar ^{23}Na^{87}Rb Molecules. *Phys. Rev. Lett.*, 116:205303, May 2016.

[50] V. N. Efimov. WEAKLY-BOUND STATES OF 3 RESONANTLY-INTERACTING PARTICLES. *Sov. J. Nucl. Phys.*, 12:589, 1971.

[51] V. Efimov. Energy levels arising form the resonant two-body forces in a three-body system. *Phys. Lett.*, B33:563–564, 1970.

[52] Dezhi Xiong, Fudong Wang, Xiaoke Li, Ting-Fai Lam, and Dajun Wang. Production of a rubidium Bose-Einstein condensate in a hybrid trap with light induced atom desorption. *arXiv:1303.0333*, 2013.

[53] Fudong Wang, Xiaoke Li, Dezhi Xiong, and Dajun Wang. A double species 23 Na and 87 Rb Bose—Einstein condensate with tunable mis-

cibility via an interspecies Feshbach resonance. *Journal of Physics B: Atomic, Molecular and Optical Physics*, 49(1):015302, 2016.

[54] J.T.M. Walraven. *Quantum Gases-Collisions and Statistics*. University of Vienna, 2013.

[55] Roger G. Newton. *Scattering Theory of Waves and Particles*. Springer Berlin Heidelberg, 1982.

[56] C. J. Pethick and H. Smith. *Bose—Einstein Condensation in Dilute Gases*. Cambridge University Press, second edition, 2008. Cambridge Books Online.

[57] P. A. Ruprecht, Mark Edwards, K. Burnett, and Charles W. Clark. Probing the linear and nonlinear excitations of Bose-condensed neutral atoms in a trap. *Phys. Rev. A*, 54:4178–4187, Nov 1996.

[58] Xiaoke Li. *Coherent Heteronuclear Spin Dynamics in an Ultracold Spinor Mixture*. PhD thesis, Chinese University of Hong Kong, 2015.

[59] Jun Chen. Optical dipole traps for optimized preparation of ultracold atomic mixtures. Master's thesis, Chinese University of Hong Kong, 2014.

[60] B. P. Anderson and M. A. Kasevich. Loading a vapor-cell magneto-optic trap using light-induced atom desorption. *Phys. Rev. A*, 63:023404, Jan 2001.

[61] Emmanuel Mimoun, Luigi De Sarlo, David Jacob, Jean Dalibard, and Fabrice Gerbier. Fast production of ultracold sodium gases using light-induced desorption and optical trapping. *Phys. Rev. A*, 81:023631, Feb 2010.

[62] A. S. Arnold, J. S. Wilson, and M. G. Boshier. A simple extended-cavity diode laser. *Review of Scientific Instruments*, 69(3):1236–1239, 1998.

[63] S.N. Atutov, V. Biancalana, A. Burchianti, R. Calabrese, S. Gozzini, V. Guidi, P. Lenisa, C. Marinelli, E. Mariotti, L. Moi, K. Nasyrov, and S. Pod'yachev. Sodium MOT collection efficiency as a function of the trapping and repumping laser frequencies and intensities. *The European Physical Journal D - Atomic, Molecular, Optical and Plasma Physics*, 13(1):71–82, 2001.

[64] John Weiner, Vanderlei S. Bagnato, Sergio Zilio, and Paul S. Julienne. Experiments and theory in cold and ultracold collisions. *Rev. Mod. Phys.*, 71:1–85, Jan 1999.

[65] Rudolf Grimm, Matthias Weidemller, and Yurii B. Ovchinnikov. Optical Dipole Traps for Neutral Atoms. In Benjamin Bederson and Herbert Walther, editors, *Advances In Atomic, Molecular, and Optical Physics*, volume 42 of *Advances In Atomic, Molecular, and Optical Physics*, pages 95 – 170. Academic Press, 2000.

[66] Xiaoke Li, Bing Zhu, Xiaodong He, Fudong Wang, Mingyang Guo, Zhi-Fang Xu, Shizhong Zhang, and Dajun Wang. Coherent Heteronuclear Spin Dynamics in an Ultracold Spinor Mixture. *Phys. Rev. Lett.*, 114:255301, Jun 2015.

[67] Y.-J. Lin, A. R. Perry, R. L. Compton, I. B. Spielman, and J. V. Porto. Rapid production of ^{87}Rb Bose-Einstein condensates in a combined magnetic and optical potential. *Phys. Rev. A*, 79:063631, Jun 2009.

[68] M. S. Safronova, Bindiya Arora, and Charles W. Clark. Frequency-dependent polarizabilities of alkali-metal atoms from ultraviolet through infrared spectral regions. *Phys. Rev. A*, 73:022505, Feb 2006.

[69] M. E. Gehm, K. M. O'Hara, T. A. Savard, and J. E. Thomas. Dynamics of noise-induced heating in atom traps. *Phys. Rev. A*, 58:3914–3921, Nov 1998.

[70] D.E. Miller. *Studying Coherence in Ultra-Cold Atomic Gases*. PhD thesis, Massachusetts Institute of Technology, 2007.

[71] W. Ketterle, D. S. Durfee, and D. M. Stamper-kurn. Making, probing and understanding Bose-Einstein condensates. In *Proceedings of the International School of Physics "Enrico Fermi", Course CXL, Edited by M. Inguscio, S. Stringari and C.E. Wieman*, page 67. IOS Press, Amsterdam, 1999.

[72] G. Reinaudi, T. Lahaye, Z. Wang, and D. Guéry-Odelin. Strong saturation absorption imaging of dense clouds of ultracold atoms. *Opt. Lett.*, 32(21):3143–3145, Nov 2007.

[73] D.J. McCarron. *A Quantum Degenerate Mixture of ^{87}Rb and ^{133}Cs*. PhD thesis, Durham University, 2011.

[74] Wolfgang Petrich, Michael H. Anderson, Jason R. Ensher, and Eric A. Cornell. Stable, Tightly Confining Magnetic Trap for Evaporative Cooling of Neutral Atoms. *Phys. Rev. Lett.*, 74:3352–3355, Apr 1995.

[75] David E. Pritchard. Cooling Neutral Atoms in a Magnetic Trap for Precision Spectroscopy. *Phys. Rev. Lett.*, 51:1336–1339, Oct 1983.

[76] Tilman Esslinger, Immanuel Bloch, and Theodor W. Hänsch. Bose-Einstein condensation in a quadrupole-Ioffe-configuration trap. *Phys. Rev. A*, 58:R2664–R2667, Oct 1998.

[77] K. M. O'Hara, M. E. Gehm, S. R. Granade, and J. E. Thomas. Scaling laws for evaporative cooling in time-dependent optical traps. *Phys. Rev. A*, 64:051403, Oct 2001.

[78] A. Mosk, S. Kraft, M. Mudrich, K. Singer, W. Wohlleben, R. Grimm, and M. Weidemüller. Mixture of ultracold lithium and cesium atoms in an optical dipole trap. *Applied Physics B*, 73(8):791–799, 2014.

[79] Huang Wu and Christopher J Foot. Direct simulation of evaporative cooling. *Journal of Physics B: Atomic, Molecular and Optical Physics*, 29(8):L321, 1996.

[80] S. E. Pollack, D. Dries, M. Junker, Y. P. Chen, T. A. Corcovilos, and R. G. Hulet. Extreme Tunability of Interactions in a ^{7}Li Bose-Einstein Condensate. *Phys. Rev. Lett.*, 102:090402, Mar 2009.

[81] Cindy A. Regal, Christopher Ticknor, John L. Bohn, and Deborah S. Jin. Creation of ultracold molecules from a Fermi gas of atoms. *Nature*, 424(6944):47–50, July 2003.

[82] G. Zürn, T. Lompe, A. N. Wenz, S. Jochim, P. S. Julienne, and J. M. Hutson. Precise Characterization of ^{6}Li Feshbach Resonances Using Trap-Sideband-Resolved RF Spectroscopy of Weakly Bound Molecules. *Phys. Rev. Lett.*, 110:135301, Mar 2013.

[83] T. Mukaiyama, J. R. Abo-Shaeer, K. Xu, J. K. Chin, and W. Ketterle. Dissociation and Decay of Ultracold Sodium Molecules. *Phys. Rev. Lett.*, 92:180402, May 2004.

[84] Stephan Dürr, Thomas Volz, and Gerhard Rempe. Dissociation of ultracold molecules with Feshbach resonances. *Phys. Rev. A*, 70:031601, Sep 2004.

[85] S. B. Papp and C. E. Wieman. Observation of Heteronuclear Feshbach Molecules from a ^{85}Rb$^{\smile}$^{87}Rb Gas. *Phys. Rev. Lett.*, 97:180404, Oct 2006.

[86] P. O. Fedichev, M. W. Reynolds, and G. V. Shlyapnikov. Three-Body Recombination of Ultracold Atoms to a Weakly Bound s Level. *Phys. Rev. Lett.*, 77:2921–2924, Sep 1996.

[87] In preparation.

[88] C. Marzok, B. Deh, C. Zimmermann, Ph. W. Courteille, E. Tiemann, Y. V. Vanne, and A. Saenz. Feshbach resonances in an ultracold ^{7}Li and ^{87}Rb mixture. *Phys. Rev. A*, 79:012717, Jan 2009.

[89] T. Schuster, R. Scelle, A. Trautmann, S. Knoop, M. K. Oberthaler, M. M. Haverhals, M. R. Goosen, S. J. J. M. F. Kokkelmans, and E. Tiemann. Feshbach spectroscopy and scattering properties of ultracold Li + Na mixtures. *Phys. Rev. A*, 85:042721, Apr 2012.

[90] M. Repp, R. Pires, J. Ulmanis, R. Heck, E. D. Kuhnle, M. Weidemüller, and E. Tiemann. Observation of interspecies ^{6}Li-^{133}Cs Feshbach resonances. *Phys. Rev. A*, 87:010701, Jan 2013.

[91] P. Ao and S. T. Chui. Binary Bose-Einstein condensate mixtures in weakly and strongly segregated phases. *Phys. Rev. A*, 58:4836–4840, Dec 1998.

[92] C. K. Law, H. Pu, N. P. Bigelow, and J. H. Eberly. "Stability Signature" in Two-Species Dilute Bose-Einstein Condensates. *Phys. Rev. Lett.*, 79:3105–3108, Oct 1997.

[93] D. M. Harber, H. J. Lewandowski, J. M. McGuirk, and E. A. Cornell. Effect of cold collisions on spin coherence and resonance shifts in a magnetically trapped ultracold gas. *Phys. Rev. A*, 66:053616, Nov 2002.

[94] M. Egorov, B. Opanchuk, P. Drummond, B. V. Hall, P. Hannaford, and A. I. Sidorov. Measurement of s-wave scattering lengths in a two-component Bose-Einstein condensate. *Phys. Rev. A*, 87:053614, May 2013.

[95] Krzysztof Jachymski and Paul S. Julienne. Analytical model of overlapping Feshbach resonances. *Phys. Rev. A*, 88:052701, Nov 2013.

[96] A. D. Lange, K. Pilch, A. Prantner, F. Ferlaino, B. Engeser, H.-C. Nägerl, R. Grimm, and C. Chin. Determination of atomic scattering lengths from measurements of molecular binding energies near Feshbach resonances. *Phys. Rev. A*, 79:013622, Jan 2009.

[97] L. Wacker, N. B. Jørgensen, D. Birkmose, R. Horchani, W. Ertmer, C. Klempt, N. Winter, J. Sherson, and J. J. Arlt. Tunable dual-species Bose-Einstein condensates of ^{39}K and ^{87}Rb. *Phys. Rev. A*, 92:053602, Nov 2015.

[98] Shai Ronen, John L. Bohn, Laura Elisa Halmo, and Mark Edwards. Dynamical pattern formation during growth of a dual-species Bose-Einstein condensate. *Phys. Rev. A*, 78:053613, Nov 2008.

[99] G. Thalhammer, G. Barontini, L. De Sarlo, J. Catani, F. Minardi, and M. Inguscio. Double Species Bose-Einstein Condensate with Tunable Interspecies Interactions. *Phys. Rev. Lett.*, 100:210402, May 2008.

[100] Paul S. Julienne, Eite Tiesinga, and Thorsten Khler. Making cold molecules by time-dependent feshbach resonances. *Journal of Modern Optics*, 51(12):1787–1806, 2004.

[101] E. Hodby, S. T. Thompson, C. A. Regal, M. Greiner, A. C. Wilson, D. S. Jin, E. A. Cornell, and C. E. Wieman. Production Efficiency of Ultracold Feshbach Molecules in Bosonic and Fermionic Systems. *Phys. Rev. Lett.*, 94:120402, Mar 2005.

[102] Tyler D. Cumby, Ruth A. Shewmon, Ming-Guang Hu, John D. Perreault, and Deborah S. Jin. Feshbach-molecule formation in a Bose-Fermi mixture. *Phys. Rev. A*, 87:012703, Jan 2013.

[103] Cheng-Hsun Wu, Jee Woo Park, Peyman Ahmadi, Sebastian Will, and Martin W. Zwierlein. Ultracold Fermionic Feshbach Molecules of $^{23}Na^{40}K$. *Phys. Rev. Lett.*, 109:085301, Aug 2012.

[104] Tetsu Takekoshi, Markus Debatin, Raffael Rameshan, Francesca Ferlaino, Rudolf Grimm, Hanns-Christoph Nägerl, C. Ruth Le Sueur, Jeremy M. Hutson, Paul S. Julienne, Svetlana Kotochigova, and Eberhard Tiemann. Towards the production of ultracold ground-state RbCs molecules: Feshbach resonances, weakly bound states, and the coupled-channel model. *Phys. Rev. A*, 85:032506, Mar 2012.

[105] Michael P. Köppinger, Daniel J. McCarron, Daniel L. Jenkin, Peter K. Molony, Hung-Wen Cho, Simon L. Cornish, C. Ruth Le Sueur, Caroline L. Blackley, and Jeremy M. Hutson. Production of optically

trapped ^{87}RbCs Feshbach molecules. *Phys. Rev. A*, 89:033604, Mar 2014.

[106] Cheng Chin and Paul S. Julienne. Radio-frequency transitions on weakly bound ultracold molecules. *Phys. Rev. A*, 71:012713, Jan 2005.

[107] C. Klempt, T. Henninger, O. Topic, M. Scherer, L. Kattner, E. Tiemann, W. Ertmer, and J. J. Arlt. Radio-frequency association of heteronuclear Feshbach molecules. *Phys. Rev. A*, 78:061602, Dec 2008.

[108] C. Weber, G. Barontini, J. Catani, G. Thalhammer, M. Inguscio, and F. Minardi. Association of ultracold double-species bosonic molecules. *Phys. Rev. A*, 78:061601, Dec 2008.

[109] Maksim Kunitski, Stefan Zeller, Jörg Voigtsberger, Anton Kalinin, Lothar Ph. H. Schmidt, Markus Schöffler, Achim Czasch, Wieland Schöllkopf, Robert E. Grisenti, Till Jahnke, Dörte Blume, and Reinhard Dörner. Observation of the Efimov state of the helium trimer. *Science*, 348(6234):551–555, 2015.

[110] Wieland Schllkopf and J. Peter Toennies. Nondestructive Mass Selection of Small van der Waals Clusters. *Science*, 266(5189):1345–1348, November 1994.

[111] Hans-Werner Hammer, Andreas Nogga, and Achim Schwenk. *Colloquium* : Three-body forces: From cold atoms to nuclei. *Rev. Mod. Phys.*, 85:197–217, Jan 2013.

[112] G. Hagen, P. Hagen, H.-W. Hammer, and L. Platter. Efimov Physics Around the Neutron-Rich ^{60}Ca Isotope. *Phys. Rev. Lett.*, 111:132501, Sep 2013.

[113] Scott E. Pollack, Daniel Dries, and Randall G. Hulet. Universality in Three- and Four-Body Bound States of Ultracold Atoms. *Science*, 326(5960):1683–1685, 2009.

[114] P. Dyke, S. E. Pollack, and R. G. Hulet. Finite-range corrections near a Feshbach resonance and their role in the Efimov effect. *Phys. Rev. A*, 88:023625, Aug 2013.

[115] Noam Gross, Zav Shotan, Servaas Kokkelmans, and Lev Khaykovich. Observation of Universality in Ultracold ^{7}Li Three-Body Recombination. *Phys. Rev. Lett.*, 103:163202, Oct 2009.

[116] Noam Gross, Zav Shotan, Servaas Kokkelmans, and Lev Khaykovich. Nuclear-Spin-Independent Short-Range Three-Body Physics in Ultracold Atoms. *Phys. Rev. Lett.*, 105:103203, Sep 2010.

[117] M. Zaccanti, B. Deissler, C. D'Errico, M. Fattori, M. Jona-Lasinio, S. Muller, G. Roati, M. Inguscio, and G. Modugno. Observation of an Efimov spectrum in an atomic system. *Nat Phys*, 5(8):586–591, August 2009.

[118] Sanjukta Roy, Manuele Landini, Andreas Trenkwalder, Giulia Semeghini, Giacomo Spagnolli, Andrea Simoni, Marco Fattori, Massimo Inguscio, and Giovanni Modugno. Test of the Universality of the Three-Body Efimov Parameter at Narrow Feshbach Resonances. *Phys. Rev. Lett.*, 111:053202, Aug 2013.

[119] R. J. Wild, P. Makotyn, J. M. Pino, E. A. Cornell, and D. S. Jin. Measurements of Tan's Contact in an Atomic Bose-Einstein Condensate. *Phys. Rev. Lett.*, 108:145305, Apr 2012.

[120] M. Berninger, A. Zenesini, B. Huang, W. Harm, H.-C. Nägerl, F. Ferlaino, R. Grimm, P. S. Julienne, and J. M. Hutson. Universality of the Three-Body Parameter for Efimov States in Ultracold Cesium. *Phys. Rev. Lett.*, 107:120401, Sep 2011.

[121] Bo Huang, Leonid A. Sidorenkov, Rudolf Grimm, and Jeremy M. Hutson. Observation of the Second Triatomic Resonance in Efimov's Scenario. *Phys. Rev. Lett.*, 112:190401, May 2014.

[122] Thomas Lompe, Timo B. Ottenstein, Friedhelm Serwane, Andre N. Wenz, Gerhard Zürn, and Selim Jochim. Radio-Frequency Association of Efimov Trimers. *Science*, 330(6006):940–944, 2010.

[123] Bo Huang, Kenneth M. O'Hara, Rudolf Grimm, Jeremy M. Hutson, and Dmitry S. Petrov. Three-body parameter for Efimov states in ^{6}Li. *Phys. Rev. A*, 90:043636, Oct 2014.

[124] Shuta Nakajima, Munekazu Horikoshi, Takashi Mukaiyama, Pascal Naidon, and Masahito Ueda. Nonuniversal Efimov Atom-Dimer Resonances in a Three-Component Mixture of ^{6}Li. *Phys. Rev. Lett.*, 105:023201, Jul 2010.

[125] Shuta Nakajima, Munekazu Horikoshi, Takashi Mukaiyama, Pascal Naidon, and Masahito Ueda. Measurement of an Efimov Trimer Binding Energy in a Three-Component Mixture of ^{6}Li. *Phys. Rev. Lett.*, 106:143201, Apr 2011.

[126] J. H. Huckans, J. R. Williams, E. L. Hazlett, R. W. Stites, and K. M. O'Hara. Three-Body Recombination in a Three-State Fermi Gas with Widely Tunable Interactions. *Phys. Rev. Lett.*, 102:165302, Apr 2009.

[127] J. R. Williams, E. L. Hazlett, J. H. Huckans, R. W. Stites, Y. Zhang, and K. M. O'Hara. Evidence for an Excited-State Efimov Trimer in a Three-Component Fermi Gas. *Phys. Rev. Lett.*, 103:130404, Sep 2009.

[128] G. Barontini, C. Weber, F. Rabatti, J. Catani, G. Thalhammer, M. Inguscio, and F. Minardi. Observation of Heteronuclear Atomic Efimov Resonances. *Phys. Rev. Lett.*, 103:043201, Jul 2009.

[129] Ruth S. Bloom, Ming-Guang Hu, Tyler D. Cumby, and Deborah S. Jin. Tests of Universal Three-Body Physics in an Ultracold Bose-Fermi Mixture. *Phys. Rev. Lett.*, 111:105301, Sep 2013.

[130] Shih-Kuang Tung, Karina Jiménez-García, Jacob Johansen, Colin V. Parker, and Cheng Chin. Geometric Scaling of Efimov States in a ^{6}Li-^{133}Cs Mixture. *Phys. Rev. Lett.*, 113:240402, Dec 2014.

[131] R. Pires, J. Ulmanis, S. Häfner, M. Repp, A. Arias, E. D. Kuhnle, and M. Weidemüller. Observation of Efimov Resonances in a Mixture with Extreme Mass Imbalance. *Phys. Rev. Lett.*, 112:250404, Jun 2014.

[132] J Ulmanis, S Hfner, R Pires, E D Kuhnle, M Weidemller, and E Tiemann. Universality of weakly bound dimers and Efimov trimers close to Li-Cs Feshbach resonances. *New Journal of Physics*, 17(5):055009, 2015.

[133] J. Ulmanis, S. Häfner, R. Pires, F. Werner, D. S. Petrov, E. D. Kuhnle, and M. Weidemüller. Universal three-body recombination and Efimov resonances in an ultracold Li-Cs mixture. *Phys. Rev. A*, 93:022707, Feb 2016.

[134] R. A. W. Maier, M. Eisele, E. Tiemann, and C. Zimmermann. Efimov Resonance and Three-Body Parameter in a Lithium-Rubidium Mixture. *Phys. Rev. Lett.*, 115:043201, Jul 2015.

[135] S. Knoop, F. Ferlaino, M. Mark, M. Berninger, H. Schobel, H.-C. Nagerl, and R. Grimm. Observation of an Efimov-like trimer resonance in ultracold atom-dimer scattering. *Nat Phys*, 5(3):227–230, March 2009.

[136] Eric Braaten and H.-W. Hammer. Efimov physics in cold atoms. *Annals of Physics*, 322(1):120 – 163, 2007. January Special Issue 2007.

[137] Hans-Werner Hammer and Lucas Platter. Efimov States in Nuclear and Particle Physics. *Annual Review of Nuclear and Particle Science*, 60(1):207–236, 2010.

[138] Yujun Wang, Jose P. D'Incao, and Brett D. Esry. Chapter 1 - Ultracold Few-Body Systems. In Paul R. Berman Ennio Arimondo and Chun C. Lin, editors, *Advances in Atomic, Molecular, and Optical Physics*, volume 62 of *Advances In Atomic, Molecular, and Optical Physics*, pages 1 – 115. Academic Press, 2013.

[139] E. Nielsen, D.V. Fedorov, A.S. Jensen, and E. Garrido. The three-body problem with short-range interactions. *Physics Reports*, 347(5):373 – 459, 2001.

[140] K. Helfrich, H.-W. Hammer, and D. S. Petrov. Three-body problem in heteronuclear mixtures with resonant interspecies interaction. *Phys. Rev. A*, 81:042715, Apr 2010.

[141] J. P. D'Incao, H. Suno, and B. D. Esry. Limits on Universality in Ultracold Three-Boson Recombination. *Phys. Rev. Lett.*, 93:123201, Sep 2004.

[142] B. S. Rem, A. T. Grier, I. Ferrier-Barbut, U. Eismann, T. Langen, N. Navon, L. Khaykovich, F. Werner, D. S. Petrov, F. Chevy, and C. Salomon. Lifetime of the Bose Gas with Resonant Interactions. *Phys. Rev. Lett.*, 110:163202, Apr 2013.

[143] Chin C. Universal scaling of Efimov resonance position in cold atom systems. *arXiv:1111.1484*, 2011.

[144] Yujun Wang and Paul S. Julienne. Universal van der Waals physics for three cold atoms near Feshbach resonances. *Nat Phys*, 10(10):768–773, October 2014.

[145] Jia Wang, J. P. D'Incao, B. D. Esry, and Chris H. Greene. Origin of the Three-Body Parameter Universality in Efimov Physics. *Phys. Rev. Lett.*, 108:263001, Jun 2012.

[146] Pascal Naidon, Shimpei Endo, and Masahito Ueda. Microscopic Origin and Universality Classes of the Efimov Three-Body Parameter. *Phys. Rev. Lett.*, 112:105301, Mar 2014.

[147] Yujun Wang, Jia Wang, J. P. D'Incao, and Chris H. Greene. Universal Three-Body Parameter in Heteronuclear Atomic Systems. *Phys. Rev. Lett.*, 109:243201, Dec 2012.

[148] R. D. Amado and F. C. Greenwood. There Is No Efimov Effect for Four or More Particles. *Phys. Rev. D*, 7:2517–2519, Apr 1973.

[149] H. W. Hammer and L. Platter. Universal properties of the four-body system with large scattering length. *The European Physical Journal A*, 32(1):113–120, 2007.

[150] J. von Stecher, J. P. D'Incao, and Chris H. Greene. Signatures of universal four-body phenomena and their relation to the Efimov effect. *Nat Phys*, 5(6):417–421, June 2009.

[151] J. P. D'Incao, J. von Stecher, and Chris H. Greene. Universal Four-Boson States in Ultracold Molecular Gases: Resonant Effects in Dimer-Dimer Collisions. *Phys. Rev. Lett.*, 103:033004, Jul 2009.

[152] F. Ferlaino, S. Knoop, M. Berninger, W. Harm, J. P. D'Incao, H.-C. Nägerl, and R. Grimm. Evidence for Universal Four-Body States Tied to an Efimov Trimer. *Phys. Rev. Lett.*, 102:140401, Apr 2009.

[153] Yujun Wang, W. Blake Laing, Javier von Stecher, and B. D. Esry. Efimov Physics in Heteronuclear Four-Body Systems. *Phys. Rev. Lett.*, 108:073201, Feb 2012.

[154] D. Blume and Yangqian Yan. Generalized Efimov Scenario for Heavy-Light Mixtures. *Phys. Rev. Lett.*, 113:213201, Nov 2014.

[155] Private communication with C.H. Greene.

[156] Olga Machtey, David A. Kessler, and Lev Khaykovich. Universal Dimer in a Collisionally Opaque Medium: Experimental Observables and Efimov Resonances. *Phys. Rev. Lett.*, 108:130403, Mar 2012.

[157] J. Schuster, A. Marte, S. Amtage, B. Sang, G. Rempe, and H. C. W. Beijerinck. Avalanches in a Bose-Einstein Condensate. *Phys. Rev. Lett.*, 87:170404, Oct 2001.

[158] Ming-Guang Hu, Ruth S. Bloom, Deborah S. Jin, and Jonathan M. Goldwin. Avalanche-mechanism loss at an atom-molecule Efimov resonance. *Phys. Rev. A*, 90:013619, Jul 2014.

[159] N. Syassen, T. Volz, S. Teichmann, S. Dürr, and G. Rempe. Collisional decay of ^{87}Rb Feshbach molecules at 1005.8 G. *Phys. Rev. A*, 74:062706, Dec 2006.

[160] F. Ferlaino, S. Knoop, M. Mark, M. Berninger, H. Schöbel, H.-C. Nägerl, and R. Grimm. Collisions between Tunable Halo Dimers: Exploring an Elementary Four-Body Process with Identical Bosons. *Phys. Rev. Lett.*, 101:023201, Jul 2008.

[161] Alexander V. Avdeenkov, Masatoshi Kajita, and John L. Bohn. Suppression of inelastic collisions of polar $^1\Sigma$ state molecules in an electrostatic field. *Phys. Rev. A*, 73:022707, Feb 2006.

[162] Gaoren Wang and Goulven Quéméner. Tuning ultracold collisions of excited rotational dipolar molecules. *New Journal of Physics*, 17(3):035015, 2015.

[163] Lincoln D Carr, David DeMille, Roman V Krems, and Jun Ye. Cold and ultracold molecules: science, technology and applications. *New Journal of Physics*, 11(5):055049, 2009.

[164] G. G. Batrouni and R. T. Scalettar. Phase Separation in Supersolids. *Phys. Rev. Lett.*, 84:1599–1602, Feb 2000.

[165] L. Pollet, J. D. Picon, H. P. Büchler, and M. Troyer. Supersolid Phase with Cold Polar Molecules on a Triangular Lattice. *Phys. Rev. Lett.*, 104:125302, Mar 2010.

[166] G. Pupillo, A. Griessner, A. Micheli, M. Ortner, D.-W. Wang, and P. Zoller. Cold Atoms and Molecules in Self-Assembled Dipolar Lattices. *Phys. Rev. Lett.*, 100:050402, Feb 2008.

[167] D. DeMille. Quantum Computation with Trapped Polar Molecules. *Phys. Rev. Lett.*, 88:067901, Jan 2002.

[168] Chaohong Lee and Elena A. Ostrovskaya. Quantum computation with diatomic bits in optical lattices. *Phys. Rev. A*, 72:062321, Dec 2005.

[169] F. M. Cucchietti and E. Timmermans. Strong-Coupling Polarons in Dilute Gas Bose-Einstein Condensates. *Phys. Rev. Lett.*, 96:210401, Jun 2006.

[170] Ryan M. Kalas and D. Blume. Interaction-induced localization of an impurity in a trapped Bose-Einstein condensate. *Phys. Rev. A*, 73:043608, Apr 2006.

[171] D H Santamore and Eddy Timmermans. Multi-impurity polarons in a dilute Bose—Einstein condensate. *New Journal of Physics*, 13(10):103029, 2011.

[172] Xavier Antoine, Weizhu Bao, and Christophe Besse. Computational methods for the dynamics of the nonlinear Schrdinger/Gross—Pitaevskii equations. *Computer Physics Communications*, 184(12):2621 – 2633, 2013.

[173] F. Dalfovo and S. Stringari. Bosons in anisotropic traps: Ground state and vortices. *Phys. Rev. A*, 53:2477–2485, Apr 1996.

[174] Xavier Antoine and Romain Duboscq. GPELab, a Matlab toolbox to solve Gross—Pitaevskii equations I: Computation of stationary solutions. *Computer Physics Communications*, 185(11):2969 – 2991, 2014.

[175] Xavier Antoine and Romain Duboscq. GPELab, a Matlab toolbox to solve Gross—Pitaevskii equations II: Dynamics and stochastic simulations. *Computer Physics Communications*, 193:95 – 117, 2015.

[176] T. Bergeman, Gidon Erez, and Harold J. Metcalf. Magnetostatic trapping fields for neutral atoms. *Phys. Rev. A*, 35:1535–1546, Feb 1987.

[177] P. Tierney. *Magnetic Trapping of an Ultracold ^{87}Rb-^{133}Cs Atomic Mixture*. PhD thesis, Durham University, 2009.